Simulation von Siliziumdetektoren und Studie des Higgs Zerfalls $H \to ZZ^* \to 4\,\mu$ für CMS (LHC)

Simulation of silicon sensors and study of the Higgs decay $H \to ZZ^* \to 4\,\mu$ for CMS (LHC)

Zur Erlangung des akademischen Grades eines
DOKTORS DER NATURWISSENSCHAFTEN
von der Fakultät für Physik der
Universität Karlsruhe(TH)

genehmigte

DISSERTATION

von

Dipl. Phys. Valeria Bartsch
aus Dortmund

Tag der mündlichen Prüfung: 19.12.2003

Referent: Prof. Dr. W. de Boer, Institut für Experimentelle Kernphysik

Korreferent: Prof. Dr. G. Quast, Institut für Experimentelle Kernphysik

Deutsche Zusammenfassung

In dieser Arbeit werden vorbereitende Studien für den CMS Detektor vorgestellt. Es handelt sich dabei zum einen um eine Studie zur Berücksichtigung des Lorentzwinkels in den Siliziumsensoren des Vertexdetektors, zum anderen um die Studie des Higgszerfallskanals $\mathrm{H} \rightarrow \mathrm{ZZ}^* \rightarrow 4\,\mu$. Zunächst wird der CMS Detektor vorgestellt.

CMS Detektor:
Der CMS Detektor (Compact Muon Solenoid) ist ein Vielzweckdetektor am Proton-Proton Speicherring LHC (Large Hadron Collider), der voraussichtlich im Jahr 2007 in Betrieb genommen wird. Am LHC werden Protonen bei einer Schwerpunktsenergie von 14 TeV [LHCb] kollidieren. Die Luminosität des Beschleunigers wird dabei so hoch sein, daß es mehrere Kollisionen pro Kreuzung der Protonenpakete gibt. Bei der Phase mit der niedrigen Luminosität von $2 \cdot 10^{33}\,\mathrm{cm}^{-2} \cdot s^{-1}$ gibt es etwa 3.41 Proton-Proton Kollisionen pro Kreuzung der Protonenpakete, bei der Phase mit der hohen Luminosität von $10^{34}\ \mathrm{cm}^{-2} \cdot s^{-1}$ sind es etwa 17.8. Die meisten dieser Kollisionen haben nur einen kleinen Impulsübertrag zwischen den wechselwirkenden Protonen. Für die Erzeugung schwerer Elementarteilchen, wie zum Beispiel des Higgs Bosons, benötigt man einen hohen Impulsübertrag. So unterscheiden sich die Eigenschaften der Endzustände, das heißt die Eigenschaften der stabilen Teilchen am Ende der Zerfallskette, voneinander. Daher kann man geeignete Trigger nutzen, um nur die physikalisch interessanten Ereignisse zu speichern.

Der CMS Detektor ist etwa 21 m lang und hat einen Durchmesser von etwa 15 m. Er besteht aus vielen Untersystemen wie in Abbildung 1 gezeigt [TRA98, ADD00, ECA97, HCA97, MUO97, TRI00, HLT03]. Ein wichtiger und der namensgebende Teil des CMS Detektors ist der supraleitende Magnet, der ein konstantes Magnetfeld von 4 T erzeugt. Das Spurrekonstruktionssystem als

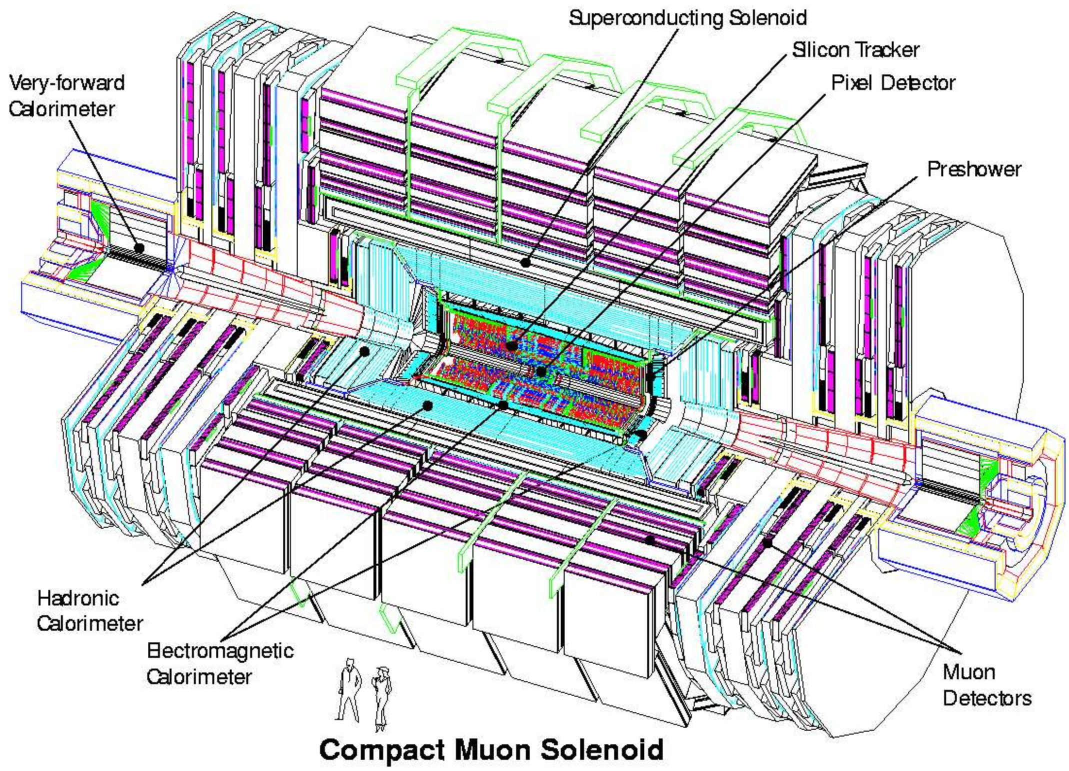

Abbildung 1: *Übersicht über den CMS Detektor [TRA98]*

auch die Kalorimeter befinden sich im Innern des Solenoidmagneten. Das innere Spurrekonstruktionssystem kann in die Siliziumpixeldetektoren und Siliziumstreifendetektoren aufgeteilt werden. Durch die Krümmung der Teilchenspuren im Magnetfeld und die hohe Segmentierung der Vertexdetektoren liefern die beiden Siliziumdetektoren eine sehr genaue Impuls- und Ortsauflösung und leisten daher einen wichtigen Beitrag zu der Myonrekonstruktion. Außerhalb des Magneten befindet sich das Myonsystem des CMS Detektors, hier werden die Myonen identifiziert und rekonstruiert.

Berücksichtigung des Lorentzwinkels bei der Spurfindung:

Der Lorentzversatz, das heißt die Ablenkung der Ladungsträger im Magnetfeld, verändert die Fitposition im Detektor signifikant und geht daher als Korrekturfaktor bei der Spurrekonstruktion ein. Bei den Siliziumstreifendetektoren des CMS Detektors beträgt der Lorentzversatz voraussichtlich 30 bis 80 μm. Die Auflösung der Detektoren sollte allerdings bei etwa 15μm liegen. In einem Magnetfeld wirkt auf die Ladungsträger sowohl eine elektrische Kraft, durch das Anlegen einer Spannung während des Betriebs, als auch die Lorentzkraft, die proportional zu

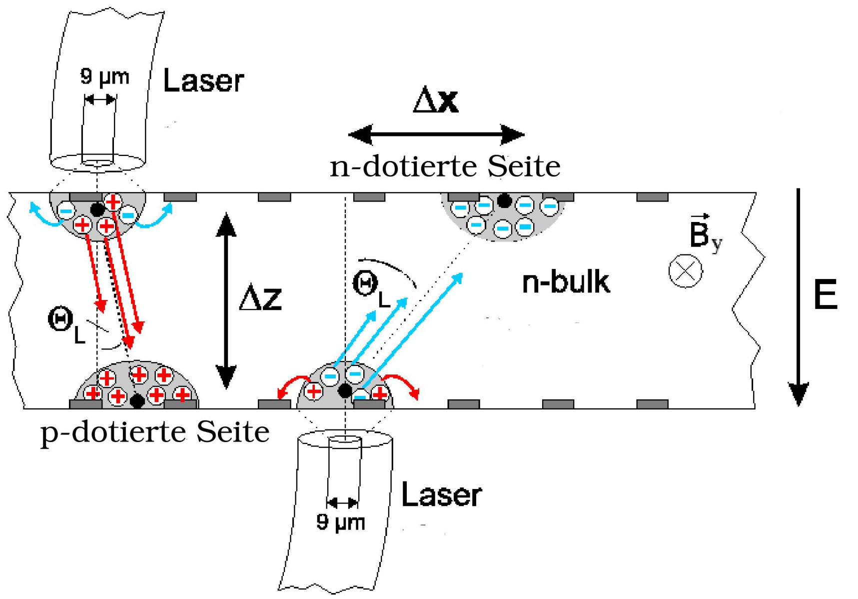

Abbildung 2: *Die Abbildung zeigt das Prinzip des Karlsruher Meßaufbaus zur Bestimmung des Lorentzwinkels für die positiven und negativen Ladungsträger (Löcher und Elektronen) [dB+01]. Der Aufbau ist mit zwei Laserfasern ausgestattet. Die roten Laser haben eine Eindringtiefe von wenigen µm, so daß man mit einem Laserpuls auf der n-dotierten Seite oder der p-dotierten Seite die Drift der Ladungsträger messen kann.*

dem angelegten Magnetfeld ist (vergleiche Abbildung 2). Aus diesen Kräften läßt sich der Lorentzwinkel berechnen. Der Lorentzwinkel Θ_L ist abhängig von der Mobilität der Ladungsträger $\mu(E)$, dem Hallstreuungsfaktor r_{H} und dem Magnetfeld B.

$$\tan(\Theta_L) = r_{\mathrm{H}} \mu B \tag{1}$$

Die Mobilität der Ladungsträger wird wiederum beeinflußt vom elektrischen Feld in einem Siliziumdetektor und wird daher durch die Strahlungsschäden, die während der Betriebszeit der Detektoren auftreten, beeinflußt. Da sich durch Strahlenschädigung die Depletionsspannung verändert, verändert sich auch das elektrische Feld und muß bei der Berechnung des Lorentzwinkels berücksichtigt werden. Bei den Siliziumpixeldetektoren wird darüber hinaus noch die Größe der depletierten Zone beachtet. Neben der Depletionsspannung kann sich während des Betriebes auch die Mobilität der Ladungsträger bei vernachlässigbarem elektrischen Feld ändern. Berücksichtigt man all diese Abhängigkeiten, kann man eine Korrektur auf die Verschiebung der Ladungsträger ermitteln. Diese Lorentzverschiebung ist sowohl mit in Karlsruhe aufgenommenen Daten als auch mit Literaturdaten [Ale00] verglichen worden. Wie in Abbildung 3 gezeigt wird, stimmt die Simulation mit den Daten sehr gut überein. Der Algorithmus zur Berechnung des Lorentzwinkels ist in die CMS Rekonstruktionssoftware implementiert worden.

Das Higgs Teilchen:

Im zweiten Teil der Arbeit ist der Higgszerfallskanals $\mathrm{H} \rightarrow \mathrm{ZZ}^* \rightarrow 4\,\mu$ untersucht worden. Zunächst wird die theoretische Motivation für das Higgsboson dargestellt. Das Standardmodell der Teilchenphysik beschreibt - bis auf die Gravitation - alle fundamentalen Kräfte. Allerdings ist es nicht möglich in dieser Theorie Massenterme einzuführen, da die Massenterme nicht invariant unter lokalen Eichtransformationen sind. Dieses Problem kann durch die spontanen Symmetriebrechung gelöst werden. Man erhält allerdings ein weiteres Teilchen, das sogenannte Higgs Teilchen. Die Masse des Higgs Teilchens ist ein freier Parameter der Theorie. Durch Messungen an den LEP (Large Electron Positron Collider) Experimenten konnte die untere Grenze der Higgs Masse auf etwa 114 GeV bestimmt werden, die obere Grenze folgt aus elektroschwachen Präzisionsmessungen und liegt bei etwa 219 GeV. Erweiterungen des Standardmodells wie das Minimal Supersymmetrische Modell grenzen die Higgs Masse stärker ein. Das leichteste Higgs Boson des Minimal Supersymmetrischen Modells, das dem Standardmodell Higgs Boson am ähnlichsten ist, sollte eine Masse kleiner als 125 GeV haben. Daher ist in dieser Arbeit ein Massenbereich von 115 GeV bis 140 GeV untersucht worden. Bei dem Zerfallskanal $\mathrm{H} \rightarrow \mathrm{ZZ}^* \rightarrow 4\,\mu$ ist der Zerfall des Higgsbosons in zwei Z-Bosonen dabei stark unterdrückt, da eines der beiden Z-Bosonen außerhalb der Massenschale erzeugt wird. Abhängig von der Higgsmasse werden bei der Strahlungskorrektur erster Ordnung Wirkungsquerschnitte von etwa 43 fb bis 33 fb vorhergesagt [Spi95, H^+92, C^+95a, Kun84, MP91, DW89, Spi98]. Das entspricht im ersten Jahr des LHC Betriebs 4 bis 30 detektierbaren Ereignissen abhängig von der Higgsmasse. Dadurch daß nur leptonische Ereignisse, in diesem Fall myonische Ereignisse, verwendet werden, ist das Signal sehr klar und es gibt nur wenige Untergrundkanäle, die dem Signal ähnliche Eigenschaften aufweisen. Die wichtigsten Untergründe für diesen Kanal sind der $\mathrm{t\bar{t}} \rightarrow 4\mu$, $\mathrm{Zb\bar{b}} \rightarrow 4\mu$ und der $\mathrm{ZZ}^* \rightarrow 4\mu$ Untergrund. Diese Untergründe enthalten sowohl vier Myonen im Endzustand als auch schwere Eichbosonen, so daß sie Ähnlichkeit mit den

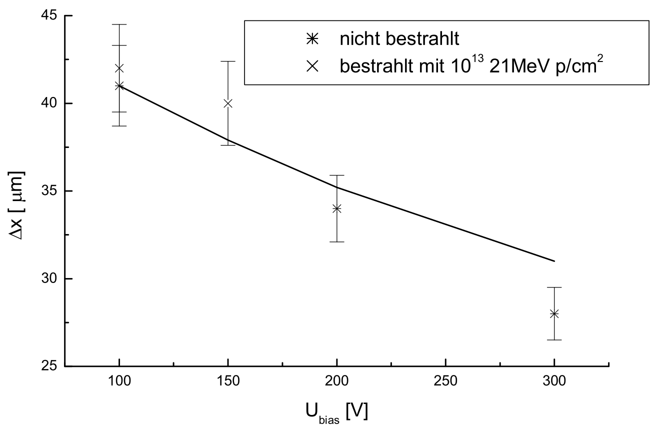

(a)

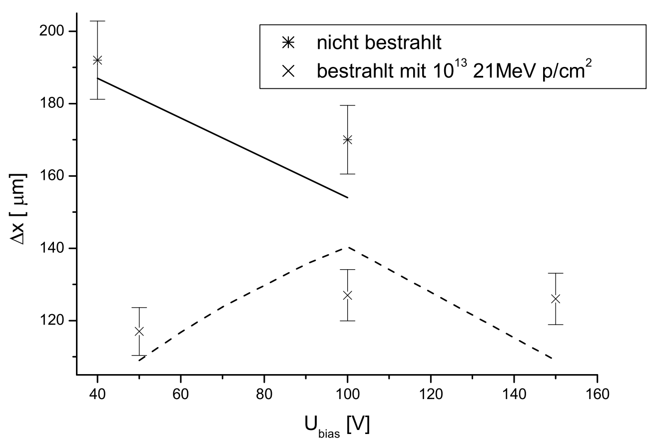

(b)

Abbildung 3: *Die Lorentzverschiebung* Δx *für Löcher (obere Abbildung) und Elektronen (untere Abbildung). Die Ladungsträger sind an der Oberfläche eines* $300\,\mu m$ *dicken Sensors erzeugt worden. Die Balken repräsentieren systematische Fehler. Die Daten sind bei einer Temperatur von* $260\,K$ *(für die Löcher) und* $280\,K$ *(für die Elektronen) aufgenommen worden. Die Linien entsprechen der Simulation des Lorentzwinkels.*

Signalereignissen haben. Nach einer weichen Vorselektion des Untergrundes werden etwa 4000 Untergrundereignisse im ersten Jahr von LHC erwartet. Der Wirkungsquerschnitt des Untergrundes nach der Vorselektion ist damit um etwa einen Faktor 100 größer als der des Signals. Neben den Untergrundprozessen mit vier Myonen im Endzustand sind weitere Untergrundprozesse untersucht worden. Ereignisse mit Myonen aus verschiedenen Kollisionen, das heißt zwei oder drei Myonen aus einer Kollision und ein oder zwei Myonen aus einer anderen, haben sehr große Wirkungsquerschnitte. Im Vergleich zum Signal ist der Abstand der Vertices der verschiedenen Kollisionen dieses Untergrundes hoch. Daher kann man diesen Untergrund mit Hilfe eines Selektionsschnitts auf den Abstand der Vertices sehr gut unterdrücken.

Myonenrekonstruktion:

Im Idealfall werden die Myonen mit einem effizienten Rekonstruktionsalgorithmus auf den getriggerten Daten rekonstruiert. Im Moment ist der Rekonstruktionsalgorithmus, der für den Trigger verwendet wird, allerdings besser als alle anderen Algorithmen und wird daher für diese Arbeit verwendet. Die Rekonstruktionseffizienz, die als Verhältnis der generierten vier Myonereignisse gegenüber den rekonstruierten vier Myonereignissen definiert ist, liegt zwischen etwa 48% bis 77%. Die Auflösung wird im Wesentlichen durch das Myon mit dem kleinsten p_T bestimmt und ist daher für die Untergrundprozesse, die Myonen aus b Quarks enthalten, und für die kleinen Higgsmasse gering. Die Auflösung des transversalen Impulses p_T ist 2 - 4 % über das ganze simulierte p_T Spektrum. Dies entspricht der im Technischen Design Reports des Trackers [TRA98] spezifierten Auflösung.

Selektionsschnitte:

Als Selektionsschnitte zur Abtrennung von Signal- und Untergrundereignissen sind kinematische Variablen, wie die sortierten transversalen Impulse und invarianten Massen für die Z-Bosonen und das Higgsboson, als auch das Isolationskriterium herangezogen worden. Die invariante Masse zweier Myonen mit unterschiedlichen Ladungen ergibt im Fall von Signalereignissen die Z-Boson Masse. Die Zuordnung, die eine invariante Masse nahe der realen Z-Boson Masse besitzt, ist ein Z-Boson Kandidat. Die andere Kombination ist ein Kandidat für das virtuelle Z-Boson. Die Verteilungen für die Signalereignisse und die Untergrundereignisse unterscheiden sich stark, so daß man einen großen Unterdrückungsfaktor erhält. Sortiert man die transversalen Impulse der Myonen pro Ereignis, so fällt auf, daß die Verteilungen der Myonen mit den niedrigsten transversalen Impulsen deutliche Unterschiede zwischen dem Signal und dem Untergrund aufweisen. Dies liegt daran, daß die Myonen der Untergrundereignisse mit niedrigem p_T meist auf der Hadronisation der b-Quarks stammen. Ein weiterer Selektionsschnitt, der auf die Myonen aus den b-Quarks wirkt, die in dem $\mathrm{t\bar{t}} \rightarrow W^+bW^-\bar{b}$ und $\mathrm{Zb\bar{b}}$ Untergrundprozessen enthalten sind, ist das Isolationskriterium. Ein Myon gilt als isoliert, solange in einem Kegel um die Myonspur herum der deponierte transversale Impuls, beziehungsweise die transversale Energie, geringer als ein bestimmter Grenzwert ist. Optimiert man die Kegelgröße und den Grenzwert, kann man mit diesem Kriterium einen großen Teil des $\mathrm{t\bar{t}}$ und $\mathrm{Zb\bar{b}}$ Untergrundes unterdrücken. Das Resultat der gesamten Schnitte ist sowohl für die Phase mit geringer Luminosität als auch für Phase mit hoher Luminosität in Abbildung 4 dargestellt.

Beobachtbarkeit des Signals:

Es handelt sich also bei diesem Zerfallskanal um einen Kanal mit geringer Statistik. Bisher wird bei CMS zur Abschätzung der Signifikanz ein Ereigniszählschätzer verwendet. Man zählt die Anzahl der Signalereignisse in einem bestimmten Higgsmassenbereich N_s und die Zahl der Untergrundereignisse N_b. Das Verhältnis $S_{c1} = N_s/\sqrt{N_b}$ bildet die Abschätzung für die Signifikanz. Diese Abschätzung basiert auf Gaußscher Statistik, die jedoch für die erwartete kleine Anzahl von Ereignissen ungenau ist. Für kleine Ereigniszahlen erwartet man Poissonstatistik, die mit Hilfe der Maximum Likelihood Methode in Wahrscheinlichkeit umgewandelt werden kann. Das Verhältnis der Hypothese, daß sowohl Signal als auch Untergrund auftreten, und der Hypothese, daß nur Untergrund vorhanden ist, wird mit Q bezeichnet. $S_{l2} = \sqrt{2\ln Q}$ ist die Abschätzung für die Signifikanz der Likelihood-Methode. Hierbei wird die gesamte Statistik der Monte-Carlo-Ereignisse, die durch Gewichtungsfaktoren auf die zu erwartenden Ereignisse gewichtet worden sind, verwendet (vergleiche Bild 5).

Mit Hilfe der oben eingeführten Formeln für die Abschätzung der Signifikanzen erhält man die in Tabelle 1 angegebenen Signifikanzen für die Phasen mit niedriger und hoher Luminosität. Man sieht, daß S_{c1} die Signifikanz stark überschätzt. Mit der Signifikanz S_{l2} ist in der Phase mit niedriger Luminosität nach einem Jahr keine Higgsentdeckung möglich, das heißt man muß mehrere

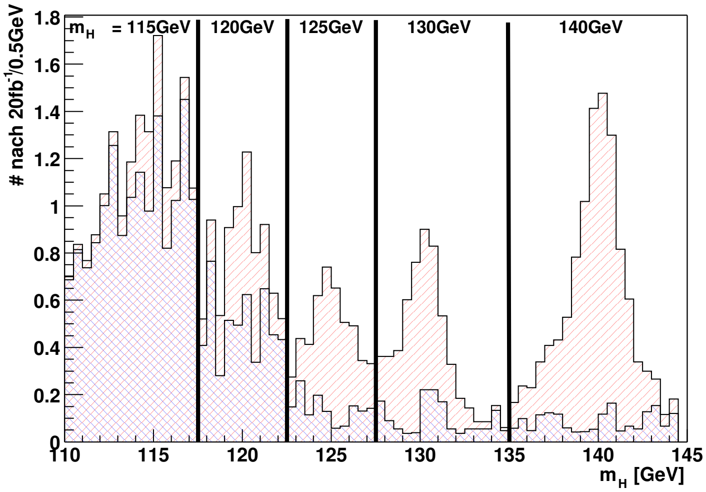

(a)

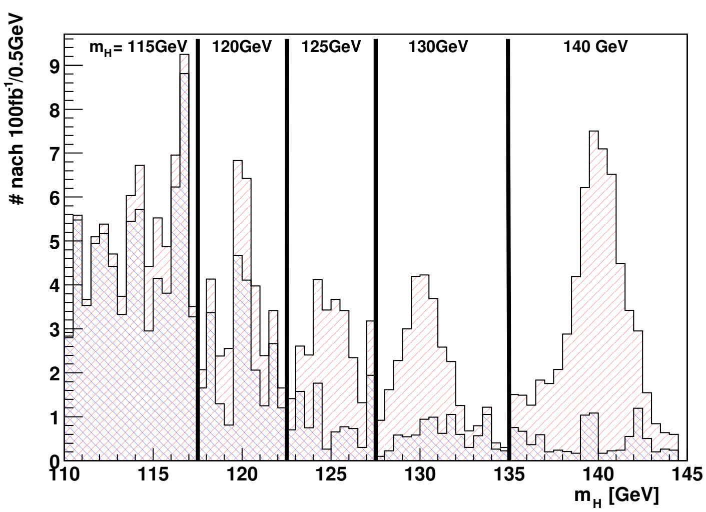

(b)

Abbildung 4: *Signal- und Untergrundverteilungen für einige Higgsmassen. Die obere Abbildung zeigt die Verteilung für ein Jahr niedriger Luminosität, die untere für ein Jahr hoher Luminosität. Für jede Masse wurden optimierte Selektionsschnitte verwendet. Die Signalereignisse sind in rot (hell schattiert) dargestellt, die Untergrundereignisse in blau (dunkel schattiert).*

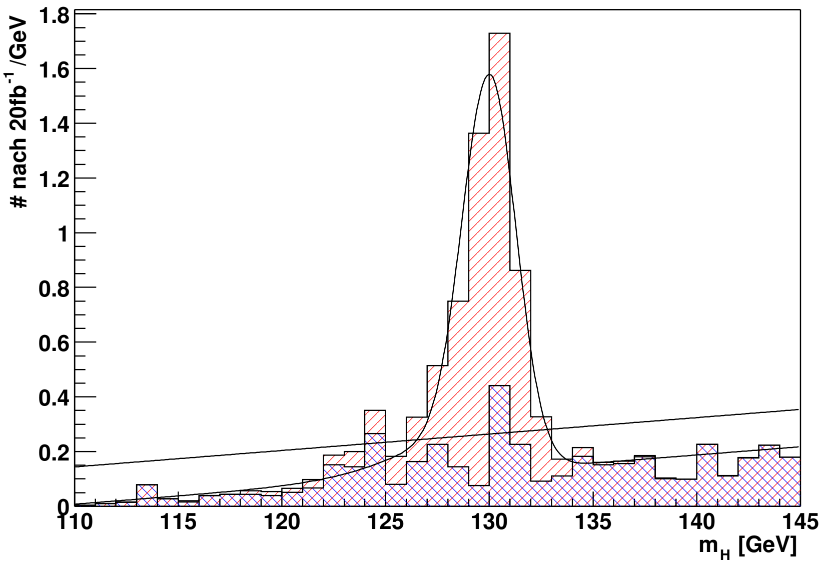

Abbildung 5: *Histogramm, daß die rekonstruierte invariante Masse der vier Myonen für eine integrierte Luminosität von $20\,fb^{-1}$ darstellt. Das Histogramm ist die gewichtete Summe der Signalereignisse aus dem Higgszerfallskanal $H \rightarrow 4\mu$ und der Untergrundereignisse der wichtigsten Untergründe. Die gerade Linie ist ein Ausgleichsgerade für die Hypothese, dass nur Untergrund vorhanden ist, die Kurve erhält man unter der Annahme, dass sowohl Signal als auch Untergrund beiträgt.*

Higgszerfallskanäle kombinieren.

Im Vergleich zu einer ältere Studie [Dro97] sind die erhaltenen Signifikanzen trotz der realistischeren Simulation größer. Die ältere Studie beruht im Gegensatz zu dieser Arbeit auf schneller Detektorsimulation und den damals gültigen Wirkungsquerschnitten. Es sind kinematische Selektionsschnitte zur Auswahl der Ereignisse, also Selektionsschnitte auf die transversalen Impulse sowie die invarianten Z-Boson Massen und ein Kriterium zur Klassifizierung und Unterdrückung von b-Quarks verwendet worden. Unglücklicherweise kann man die ältere Analyse nur mit Hilfe von Ereigniszählmethoden auswerten. Mit dem Schätzer für die Signifikanz $S_{c12} = 2 * (\sqrt{N_s + N_b} - \sqrt{N_b})$ [BK00], der am vertrauenswürdigsten von den Ereigniszählmethoden ist, erhält man für die ältere Studie eine Signifikanz von 2.5 für eine Higgsmasse von 130 GeV nach $20\,\mathrm{fb}^{-1}$ gegenüber 3.2 mit dieser Studie. Die wesentliche Neuerung dieser Studie ist die Optimierung des

Tabelle 1: *Likelihood Signifikanz* $S_{l2} = \sqrt{2lnQ}$ *für einige Higgsmassen, zum Vergleich die Ereigniszählsignifikanz* $S_{c1} = \frac{N_s}{\sqrt{N_b}}$. *Die integrierte Luminosität für die Phase mit niedriger Luminosität ist* $20\,fb^{-1}$, *das entspricht der Datennahme des ersten Betriebsjahres, für die Phase mit hoher Luminosität* $100\,fb^{-1}$, *das entspricht einem Jahr bei hoher Luminosität.*

Higgsmasse	140 GeV	130 GeV	125 GeV	120 GeV	115 GeV
Phase mit niedriger Luminosität					
S_{l2}	4.2	3.2	2.3	1.1	0.5
S_{c1}	7.6	5.7	3.6	1.2	0.5
Phase mit hoher Luminosität					
S_{l2}	9.3	6.7	5.5	2.6	0.6
S_{c1}	17.2	11.2	8.3	3.0	0.7

Isolationskriteriums, das den Untergrund stark unterdrückt. Das Isolationskriterium konnte in der früheren Studie nicht eingeführt werden, da diese auf einer einfacheren Detektorsimulation beruht.

Contents

Chapter 1

Introduction

The future proton-proton collider LHC (Large Hadron Collider) at CERN (European Laboratory for Particle Physics) will have a high centre-of-mass energy of 14 TeV and a luminosity of $2 \cdot 10^{33}\, cm^{-2} \cdot s^{-1}$ in the beginning increased to $10^{34}\, cm^{-2} \cdot s^{-1}$ after the first three years, implying a significant discovery potential for new particles. One of the four detectors at the LHC will be the multipurpose detector CMS (Compact Muon Soleonid).

One of the most exciting topic in particle physics is Higgs physics. The Standard Model of elementary particle physics has been highly successful in explaining all experimental data. However, the way particles acquire mass has not yet been understood. In the Standard Model the Higgs mechanism is an elegant method to generate the masses of vector bosons and fermions, connected to the prediction of the existence of a new particle, the Higgs boson. The Standard Model Higgs boson is expected to be in the mass range of about 115 GeV which is the experimental limit of LEP to several hundred GeV [1]. This mass region will be explored by the LHC. The discovery channel $\mathrm{H} \rightarrow \mathrm{ZZ}^* \rightarrow 4\,\mu$ at CMS is studied in this thesis. For Higgs masses below about 180 GeV, which is equivalent to twice the Z mass, the decay into a Z boson pair is suppressed. So it is very challenging to study this mass region and try to extract the Higgs parameters.

The CMS detector, currently under construction, exploits a silicon detector for tracking in a magnetic field. In the magnetic field the charge carriers are

[1] In this thesis $\hbar$=c=1 is used.

deflected by the Lorentz angle, this influences the tracking performance. In this thesis the effect of the magnetic field on the charge carriers has been studied, taking into account the change of operation parameters due to radiation damage. An algorithm calculating the Lorentz angle in the silicon sensors has been developed and implemented in the full reconstruction software of CMS.

This thesis is divided into two parts: the development and implementation of the Lorentz algorithm (Chapters 3 and 4) and the study of the Higgs decay channel $\mathrm{H} \rightarrow \mathrm{ZZ}^* \rightarrow 4\,\mu$ (Chapters 5 to 7). Chapter 2 gives some general information on the design of the CMS detector.

Chapter 3 describes the principle of silicon sensors, their characteristics and mechanisms of radiation damage. In Chapter 4 the Lorentz algorithm for silicon sensors is described including radiation damage. The algorithm has been adapted for the CMS silicon sensors and an implementation of the algorithm in the CMS software is presented.

The aim of the study of the Higgs decay channel $\mathrm{H} \rightarrow \mathrm{ZZ}^* \rightarrow 4\,\mu$ is to compare the outcome of the more realistic simulation with older studies [Dro97]. In Chapter 5 the theory of the Higgs particle is introduced. Chapter 6 describes the simulation and reconstruction of the signal and backgrounds. In order to simulate the events the full simulation and reconstruction software is locally installed. The muon reconstruction algorithms are evaluated and compared with each other. In Chapter 7 the study on the Higgs decay $\mathrm{H} \rightarrow \mathrm{ZZ}^* \rightarrow 4\,\mu$ using full simulation and reconstruction software is described. The event selection is based on cuts, performed from both the low luminosity phase and the high luminosity phase. The discovery potentials in these scenarios are summarised. Furthermore backgrounds arising from multiple collisions are studied.

Chapter 2

CMS Experiment

2.1 Large Hadron Collider

The LHC storage ring will be located in the former LEP (Large Electron Positron Collider) tunnel at CERN with a circumference of 27 km. At four collision points the experiments ALICE, ATLAS, CMS and LHCb will be located (Fig. 2.1). CMS and ATLAS are multipurpose detectors with similar physics goals, while ALICE is a heavy ion experiment and LHCb will concentrate on b-physics. At the proton-proton collider LHC the protons are accelerated to 7 TeV each resulting in a centre of mass energy of 14 TeV. The collision rate is 40 MHz. Two separate beam channels, with fields equal in strength, but opposite in directions, are required. Superconducting magnets containing the two channels and their corresponding sets of coils inserted in a structure with a single cryostat are foreseen. The magnets are cooled with superfluid helium at a temperature of 1.9 K to allow a magnetic field of 8.4 T. More details of the LHC design can be found in [LHCb].

Fig. 2.2 shows the cross sections and the event rates in proton-proton and proton-antiproton collisions as a function of the center of mass energy. Depending on the Higgs mass the total cross section is about a factor 10^{12} larger than the Higgs cross section. The high $t\bar{t}$ production rate compared to the Higgs production rate is a challenge for the Higgs searches, because this process is a background for the Higgs.

It is planned to have two phases with different luminosities. The first phase with lower luminosity is planned in order to get to know the detector properties and

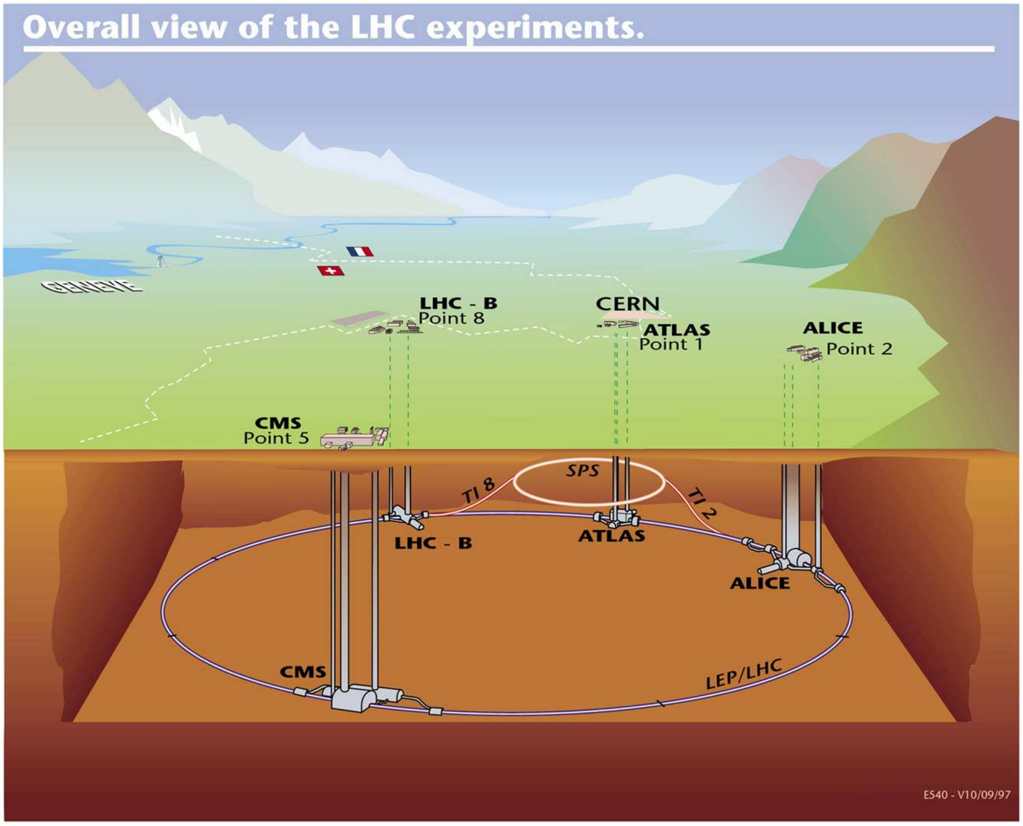

Figure 2.1: *Overview over the LHC accelerator complex*

concentrate on b-physics. In the phase with higher luminosity more precise measurements, for example of the Higgs production cross section can be done. Overall the high luminosity balances the decrease of the DeBroglie wavelength which is proportional to $1/E$. Therefore the cross section decreases to proportional $1/E^2$. For the physics simulation the following scenario is studied: In the first phase, lasting three years, LHC will run at a low luminosity of $2 \cdot 10^{33}\,\mathrm{cm}^{-2} \cdot s^{-1}$, in the second phase LHC will run at a high luminosity of $10^{34}\,\mathrm{cm}^{-2} \cdot s^{-1}$ [TRI00]. This corresponds to an accumulation of an integrated luminosity of $20\,\mathrm{fb}^{-1}$ ($100\,\mathrm{fb}^{-1}$) per year. The high luminosity causes the existence of soft interactions:

- Every incoming beam particle may leave behind a beam remnant, which does not take part in the initial-state radiation or hard scattering process.
- At the LHC several interactions happen in one bunch crossing. In addition the composite nature of the two protons implies the additional possibility that several parton pairs undergo separate hard or semi-hard scatterings,

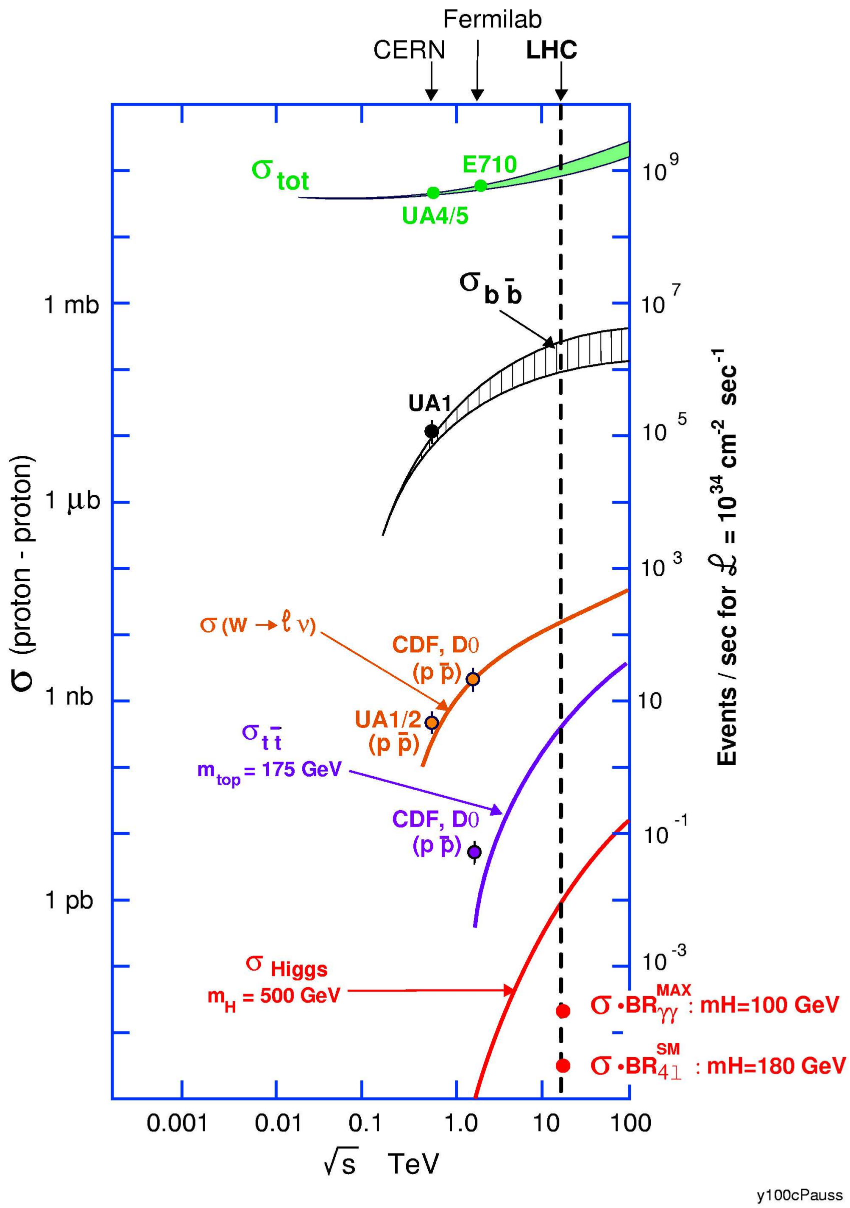

Figure 2.2: *Cross sections for hard scattering versus the center of mass energy $\sqrt{s}$. The cross section values at $\sqrt{s} = 14$ TeV are: $\sigma_{tot} = 99.4\,mb$, $\sigma_b = 0.633\,mb$, $\sigma_t = 0.888\,nb$, $\sigma_W = 187\,nb$, $\sigma_Z = 55.5\,nb$, $\sigma_H\ (m_H = 150\,GeV) = 23.8\,pb$. All except the first of these are calculated using the latest MRST parton distribution function. [lhca]*

called multiple interactions. This may give a non-negligible contribution to the underlying event structure, and thus to the total multiplicity.

- Finally, in high-luminosity colliders, it is possible to pile up events, which arise because of the detector readout time that is slower than the time between the bunch crossings.

The treatment of the multiple interactions and the pileup in the CMS software are discussed in Section 6.2.

In the hard-scattering interactions of quarks and gluons at a hadron collider, the effective centre-of-mass energy of the interaction is, unlike e^+e^- colliders, smaller than the centre-of-mass energy of the machine, because the interacting particles, quarks and gluons, carry only fractions of the proton momentum. The momentum distributions of quarks and gluons inside the proton are called parton distribution functions.

2.2 CMS Detector

The CMS detector is described in this section. For the Higgs studies especially the muon chambers and the tracker have been used and so these subsystems are described in more detail.

The CMS detector is a typical colliding beam experiment. It has almost 4π coverage with cylindrical barrels closed by planar endcaps. The total length of the detector is approximately 21 m, the diameter approximately 15 m. It consists of many different subdetectors, which interplay to make the reconstruction and identification of physical objects possible. An overview of the CMS detector is depicted in Fig. 2.3. The information given in this section relies on the Technical Design Report of CMS and its subsystems [TRA98, ADD00, ECA97, HCA97, MUO97, TRI00, HLT03].

Coordinate system:
In collider experiments a cylindrical coordinate system is used. The axis parallel to the beam direction is called z-axis. In the transverse plane the geometry of the detector is described by the parameters (r,ϕ), where ϕ is the angle in the xy-plane with respect to the z-axis. In the longitudinal plane the z-coordinate

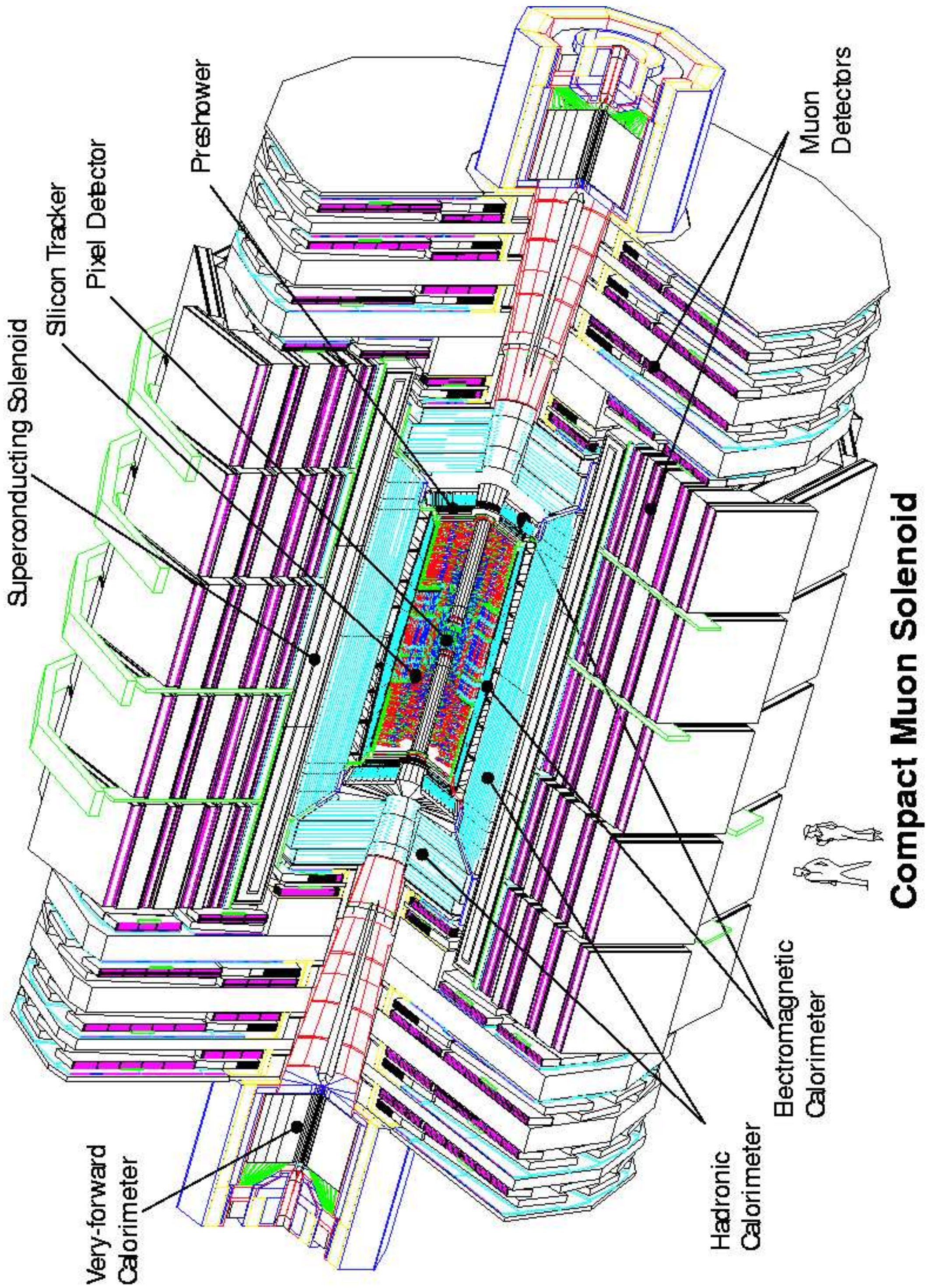

Figure 2.3: *Overview over the CMS detector [TRA98]*

along the beam axis and the angle θ are used to specify the detector coordinates. Often instead of θ the pseudorapidity η is used:

$$\eta = -\ln[\tan(\frac{\theta}{2})]. \tag{2.1}$$

For example an angle θ of 9.4° corresponds to $\eta = 2.4$.

Overview over the subsystems:

One of the most important part of the CMS detector is the superconducting solenoid providing a 4 T magnetic field parallel to the beam direction. The magnetic field causes a bending of the tracks of charged particles in the (r, ϕ)-plane. The inner tracking system and the calorimeters are inside the magnetic field. The muon chambers are situated outside the coil. There the magnetic flux of the solenoid is returned by a set of iron yokes interspersed with muon chambers. So the muon system is exposed to a lower magnetic field.

The inner tracking system consists of the silicon pixel detector and the silicon strip detector. It is used to identify bottom quarks, so called b-tagging and to reconstruct tracks and momenta. Calorimetry is performed in the electromagnetic and the hadronic calorimeter. The electromagnetic calorimeter measures the energies and positions of photons and electrons, whereas the hadronic calorimeter detects energy deposits of hadrons. The muon system identifies and measures the charge and momentum of the muons. Examples can be seen in Fig. 2.4.

In this thesis the Higgs decay channel H$\rightarrow$ 4μ has been chosen, so muon reconstruction is very important for this thesis. Muons from this decay pass the silicon tracker leaving a bent track due to the magnetic field. It passes the calorimeters and traverses through the muon system. Here the bending direction changes because the muon is exposed to a reverse magnetic field created by the return yokes forming the muon system. The muon system provides the identification of the particle as muon and together with the tracker it delivers information about the track and the momentum.

The subsystems are now discussed in more detail from the interaction point to the outermost layer of the CMS detector. Special emphasis is put on the r-dependence of the occupancy of the subdetectors which is proportional to the

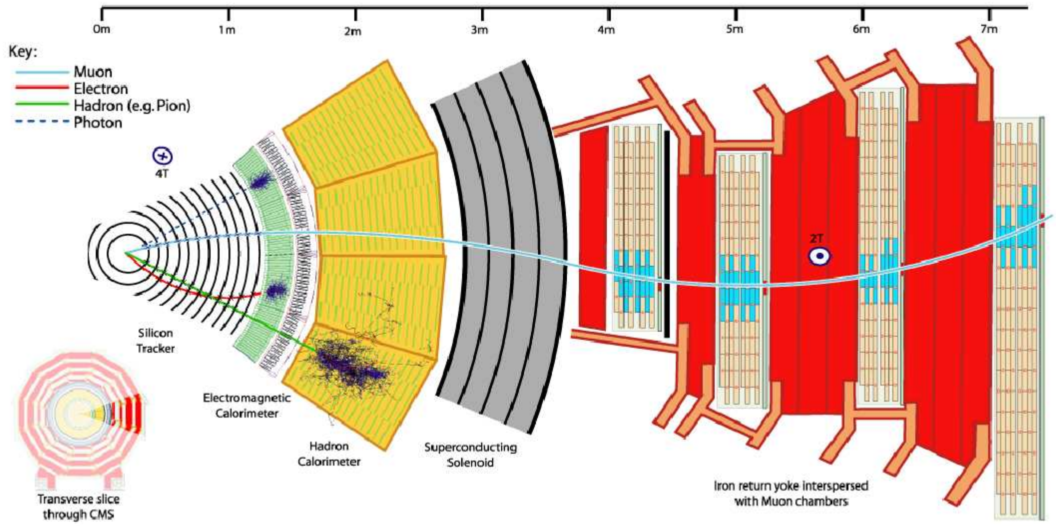

Figure 2.4: *Examples of particle tracks in a segment of the CMS detector, the blue curve represents the track of a muon , [DET02]*

number of tracks per defined area.

Tracking system:

The innermost detector is the silicon pixel detector. It consists of three modules which are placed at radii of 4.3 cm, 7.3 cm and 11 cm. The pixel size amounts to $150 \cdot 150\,\mu\mathrm{m}^2$. To enhance spatial resolution an analog signal read-out allows to profit from charge interpolation, where effects of charge sharing among pixels are present. Therefore in spite of using a pixel dimension of $150\,\mu$m an intrinsic hit resolution of about $15\,\mu$m can be obtained. Besides capacitive coupling charge sharing between pixels is mainly due to the Lorentz drift. Hence, the detectors are deliberately not tilted in the barrel layers but are tilted in the end disks. The momentum resolution is $\frac{\Delta p_T}{p_T} \approx (0.15 - 0.6)$ (p_T in GeV) depending on the η range. The whole pixel system consists out of about 1400 detector modules. The pixel detector has a geometrical acceptance of $|\eta| < 2.4$.

The silicon pixel detector is surrounded by the silicon strip sensor as sketched in Fig. 2.5. Every sensor delivers only two dimensional data instead of three

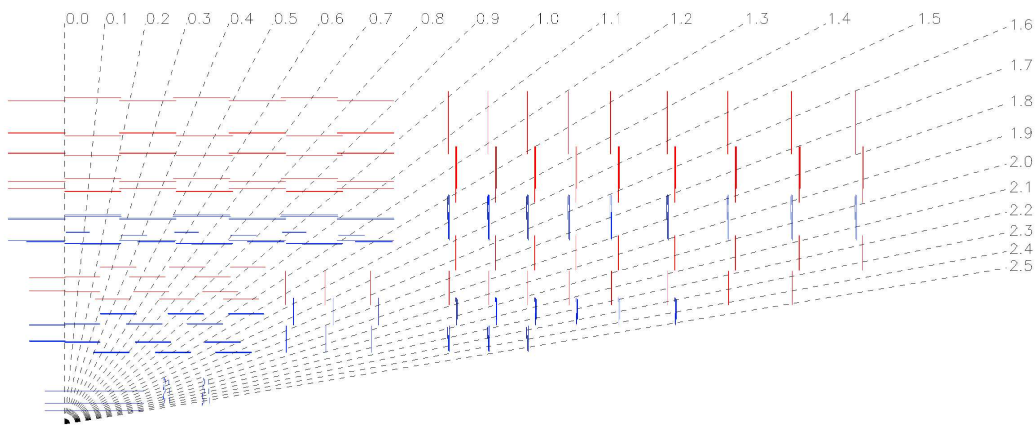

Figure 2.5: *r-z view of a half of the silicon tracker. The dotted lines are η planes. The inner barrel has four layers, the outer barrel has six layers. The inner end cap is made of three small disks on each side of the inner barrel. The outer end-cap is made of nine big disks on both sides of the tracker.*

dimensional data as the pixel detector does. This may give rise to so-called ghosthits if the occupancy of tracks in the sensor is high. A simplified example is given in Fig. 2.6. If only one charged particle passes the detector one three dimensional hit can be constructed. In contrast, two charged particles passing the detector leave an ambiguity, because four possible three dimensional hits can be constructed from the hits left in the two layers of the silicon strip detectors. In contrast to this simplified example, there are 10 layers with a small stereo angle between the layers at the CMS strip detector. The small stereo angle lowers the probability of ambiguities. Since the strip detector is located far enough from the vertex the occupancy is low enough to work with strip sensors.

The strip detectors have two different thicknesses of $320\,\mu$m in the inner layers and $500\,\mu$m in the outer layers, their strip pitches vary between 80 to $158\,\mu$m for the $320\,\mu$m thick sensors and 122 to $205\,\mu$m for the $500\,\mu$m thick sensors. The occupancy of the sensors decreases with r-dependence. In total, the silicon detector of CMS consists of about 24328 sensors and $206\,\mathrm{m}^2$ of silicon. Its outer radius extends up to 110 cm. The length of the tracker is approximately 540 cm. The inner barrel has four layers, the outer barrel has six layers in the barrel region. The inner endcap consists of three disks, the outer of nine disks.

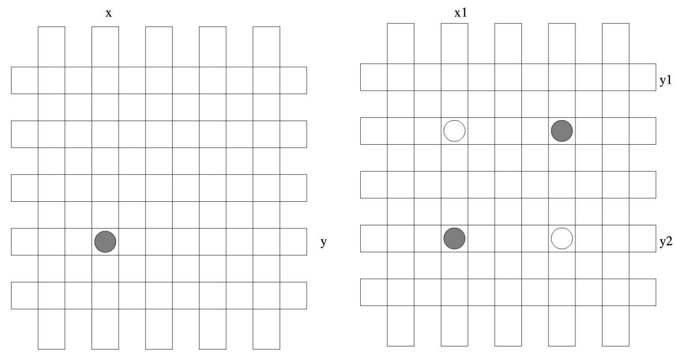

Figure 2.6: *Ambiguity in the assignment of the signal to the tracks: left hand side: clear assignment of the track to one hit, right hand side: possible assignments of the track to two hits, dark circles represent the real passage of particles, light circles show the second possibility to interpret the strip detector information.*

Calorimeters:

CMS has two calorimeters: the electromagnetic calorimeter and the hadronic calorimeter. The primary function of the electromagnetic calorimeter is to measure energies and locations of electrons and photons precisely. It should also allow a distinction between the electromagnetic showers created by leptons, electrons, photons and hadrons. The electromagnetic calorimeter consists of lead-tungsten ($PbWO_4$) crystals. $PbWO_4$ has been chosen due to its short radiation length of 0.9 cm and its short light decay time of some ns. Its fine granularity provides good spatial information. The geometrical coverage of the electromagnetic calorimeter extends up to $|\eta| = 3$ as depicted in Fig. 2.7.

A hadronic calorimeter is installed to absorb and measure the energies of hadrons. The barrel hadronic calorimeter and the endcap hadronic calorimeter are sampling calorimeters and consist of layers of copper absorber plates interleaved with plastic scintillator packages separated by air gap containers. In the very forward region $3 < |\eta| < 5$ the readout of the calorimeter is complemented by a radiation hard quartz-fibre component. This calorimeter is built to increase the coverage for the measurement of missing energy and to tag very forward jets.

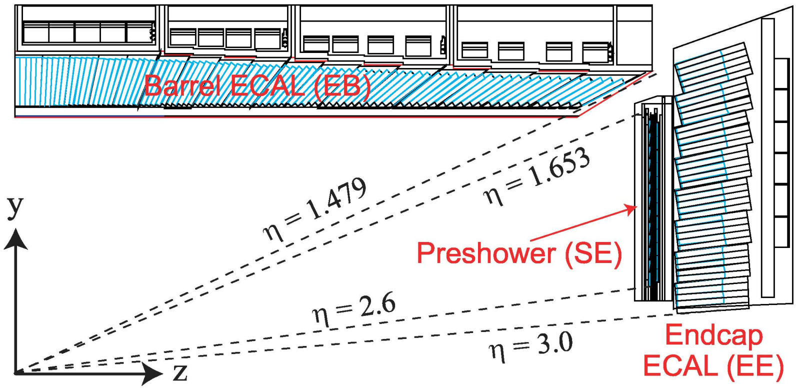

Figure 2.7: *Transverse section of ECAL*

Muon system:

The muon system identifies muons and measures their momentum and charge. The most stringent requirements on the performance of the muon system comes from the $\mathrm{H} \rightarrow \mathrm{ZZ}^* \rightarrow 4\,\mu$ decay channel. The muon system is the outermost subdetector, almost all particles other than muons are absorbed in the inner detector and the calorimeters. The energy loss of muons in the inner detector and calorimeters is approximately 3.5 GeV. The muon system consists of four barrel layers alternating with the iron wheels, and of three endcap layers as depicted in Fig. 2.8. In the iron return yokes multiple scattering occurs thus limiting the resolution of the muon system. The spatial resolution is approximately 100 μm, the standalone p_T resolution amounts $\frac{\Delta p_T}{p_T} \approx 10\%$ up to 100 GeV. Combined with the high resolution tracker information the p_t resolution is about 1 %. Detailed information is found at Sect. 6.3.

The muon system uses three different technologies to detect and measure muons: drift tubes with bunch crossing identification capability to reconstruct muon tracks in the barrel region, cathode strip chambers reconstructing tracks in the endcap region and resistive plate chambers to detect muons for trigger purposes in both barrel and endcap. The resistive plate chambers cover an η region from 0 to 2.1.

Trigger and Data Acquisition:

The Trigger and Data Acquisition system of an experiment at a hadron collider plays an essential role because the collision and the overall data rates are much

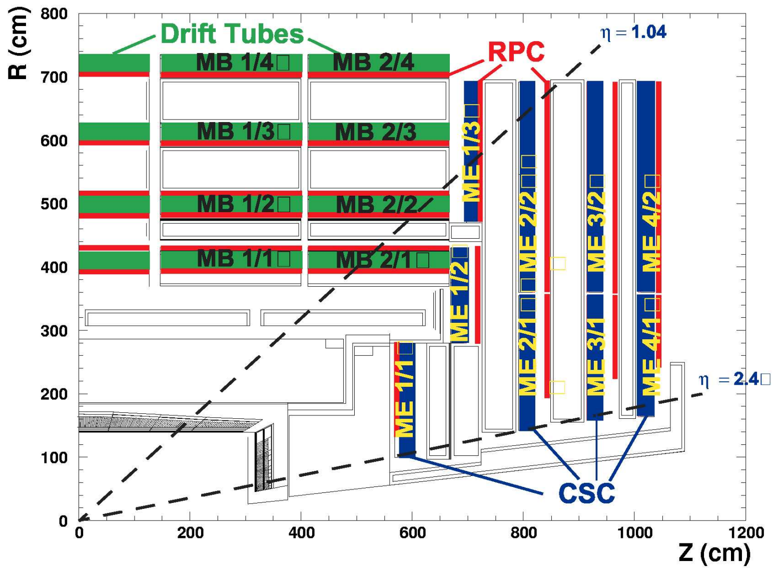

Figure 2.8: *Cross-sectional view of one quarter of CMS showing the drift tubes (DT), cathode strip chambers (CSC) and resistive plate chambers (RPC) muon systems*

higher than the rate at which interesting physics reactions, like Higgs decays, appear. The cross sections of interesting physics processes are orders of magnitude lower than the total cross section depending on the physics one is interested in. The Trigger should select the interesting physics reactions. Technically the archival storage capability is at the moment of order 100 Hz and 1000 MB/s, whereas at the design luminosity of $10^{34}\,\mathrm{cm}^{-2}\mathrm{s}^{-1}$ each bunch crossing every 25 ns results in approximately 1 MB of data. So this data has to be suppressed by a factor of 10^5. As shown in Fig. 2.9 the selection process needs to be splitted into two steps: the Level-1 Trigger and the High-Level Triggers. The Level-1 Trigger is a pure hardware trigger reducing the data by a factor of 1000 to less than 100 kHz and 75 GB/s. The time available for actually processing the data is no more than about 1 μs. Therefore the Level-1 Trigger can only process data from a subset of the CMS subdetectors - these are the calorimeters and muon chambers - with coarse granularity. The High-Level Trigger reduces the amount of data to the final output rate. It's processing time amounts about 1 s. The High-Level Trigger can be divided into a Level-2 and Level-3 Trigger, which are both software triggers. The Level-2 Trigger exploits the full calorimeter and muon chamber information. In some cases one has a Level-2.5 Trigger which includes

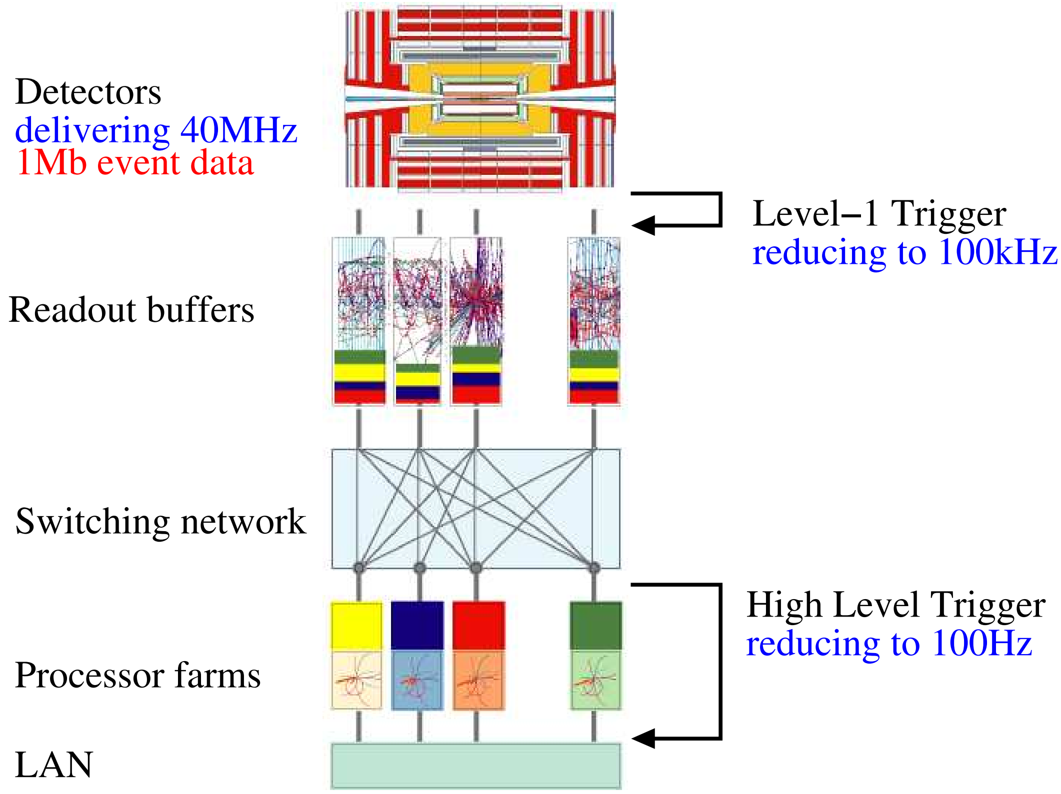

Figure 2.9: *Multilevel trigger system: The raw data of the detector need to pass the Level-1 Trigger. They are processed in the readout buffers. The High Level Trigger reduces the data to 100 Hz. Then the data are saved in the local area network (LAN).*

the pixel information. Finally the Level-3 Trigger does a full event reconstruction. An example for High-Level Trigger decisions is described in Section 6.3 for the case of muon reconstruction.

Chapter 3

Silicon Sensors

3.1 Introduction

This chapter describes the principle of silicon sensors and their main characteristics. Special emphasize is put on radiation damage, because a detailed description is needed to understand the change of behaviour of the CMS silicon sensors during operation and therefore to evaluate which aspects of radiation damage are needed for the Lorentz angle calculation.

3.2 Energy Loss in Material

A particle crossing the silicon detector interacts with the electrons and the nucleus of the silicon atoms. While direct collisions with the nuclei change the characteristics of the detector permanently, so-called radiation damage (see Sect. 3.6), the interactions with the electrons are reversible. Along its path a traversing charged particle looses part of its energy in the material described by the Bethe-Bloch-Formula [Leo94]:

$$-\frac{dE}{dx} = 4\pi\frac{N_a e^4}{m_e c^2}Z^2\frac{1}{\beta^2}[\ln\frac{2m_e c^2\beta^2\gamma^2}{I} - \beta^2] \tag{3.1}$$

The energy loss dE/dx depends on the atomic number of the medium Z. Therefore material with a high atomic number causes a strong energy loss. This is for example required for calorimeters. The constants of the equation are the charge Z of the traversing particle, the mass of the electron ($m_e = 9.11 \cdot 10^{-31}$ kg) and the Avogadro number ($N_a = 6.022 \cdot 10^{23}$). $\beta = v/c$ is the velocity of the traversing particle and γ is equal to $\frac{1}{\sqrt{1-\beta^2}}$. The average ionisation potential I for pure silicon amounts to about 173 eV.

Fig. 3.1 depicts the energy loss as a function of kinetic energy. The energy loss for particles with low momentum is proportional to $1/v^2$. The minima of the heavy particles' energy loss curves can be found at an energy which corresponds to approximately three times the rest mass. For higher momenta the energy loss for dense material increases only slightly and obtains a saturation value which lies slightly above the minimum. Therefore high energetic particles are called MIPs (Minimal Ionizing Particles). For a 300 μm thick silicon detector the most probable energy loss is 84 keV, the average value is 117 keV. An average of 3.6 eV is necessary to create an electron-hole pair in silicon, so that on average 23.000 electron-holes pairs are created by a MIP.

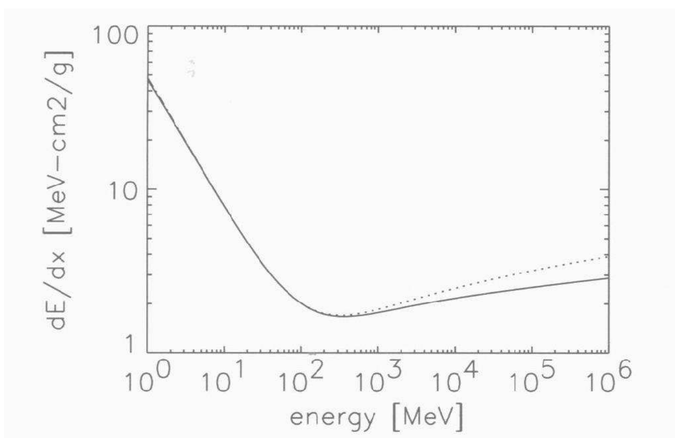

Figure 3.1: *Energy loss due to ionisation as a function of kinetic energy of a charged pion with (solid line) and without (dashed line) density- and shell-corrections. [Lut99]*

3.3 pn-junction

Silicon sensors consist of pn-diodes, which are operated with reverse bias. To extract the signal, the electron hole pairs created by the traversing particle need to be transformed into a current. Since silicon atoms have four valence electrons which are bound in the lattice structure there is no electron or hole left to conduct a current. This can be changed by adding small fractions of specific impurities.

This procedure called doping, distinguishes p- and n-doping:

- p-doping: The replacement of a silicon atom by an acceptor, an atom with only three valence electrons, is called p-doping. Thus one electron is missing in the covalent bonds and a hole is created. This change of the lattice structure is accompanied by the creation of localised energy levels in the band gap. For p-doping the energy level is found just above the valence band.

- n-doping: A silicon atom can also be replaced by a donator, an atom with five valence electrons. The occurrence of an additional electron is called n-doping. The donor energy level is found just below the conduction band.

P-doping and n-doping create holes and electrons which are not bound to a specific atom but are free for conduction. In a diode both p-doping and n-doping are used, creating at their interface a pn-junction. Here, holes and electrons diffuse and neutralise each other, forming a space-charge region, the so-called depletion zone (as sketched in Fig. 3.2).

Since ionised atoms stay at their lattice position, the diffusion leaves positive charge in the previously neutral n-doped region and negative charge in the p-doped region. Hence a potential is built up, which counteracts the diffusion of movable charge carriers. The diffusion ends when the potential is equal to the energy band bending between the p-doped and n-doped region. The diffusion voltage U_{bi} (shown in Fig. 3.2) amounts to about a few hundred mV [Sze85].

To extract a signal, the depletion zone w has to be enlarged with the help of an external voltage U_{bias}, which is has the same polarity as the diffusion voltage U_{bi}. This is called reserve biasing. With the help of the Poisson equation one can derive the width of the depletion zone w for an abrupt p^+n-junction, that is a pn-junction with an abrupt transition between very high acceptor concentration N_A and a low donator concentration N_D. From the neutrality condition for the entire diode follows that the depletion zone extends much further in the lower doped zone, so that only the parameters of the n-region are necessary to determine the depletion zone w for an asymmetric p^+n-junction:

$$w = \sqrt{\frac{2\epsilon_{Si}\epsilon_0}{q_0|N_{eff}|}(U_{bias} + U_{bi})}. \tag{3.2}$$

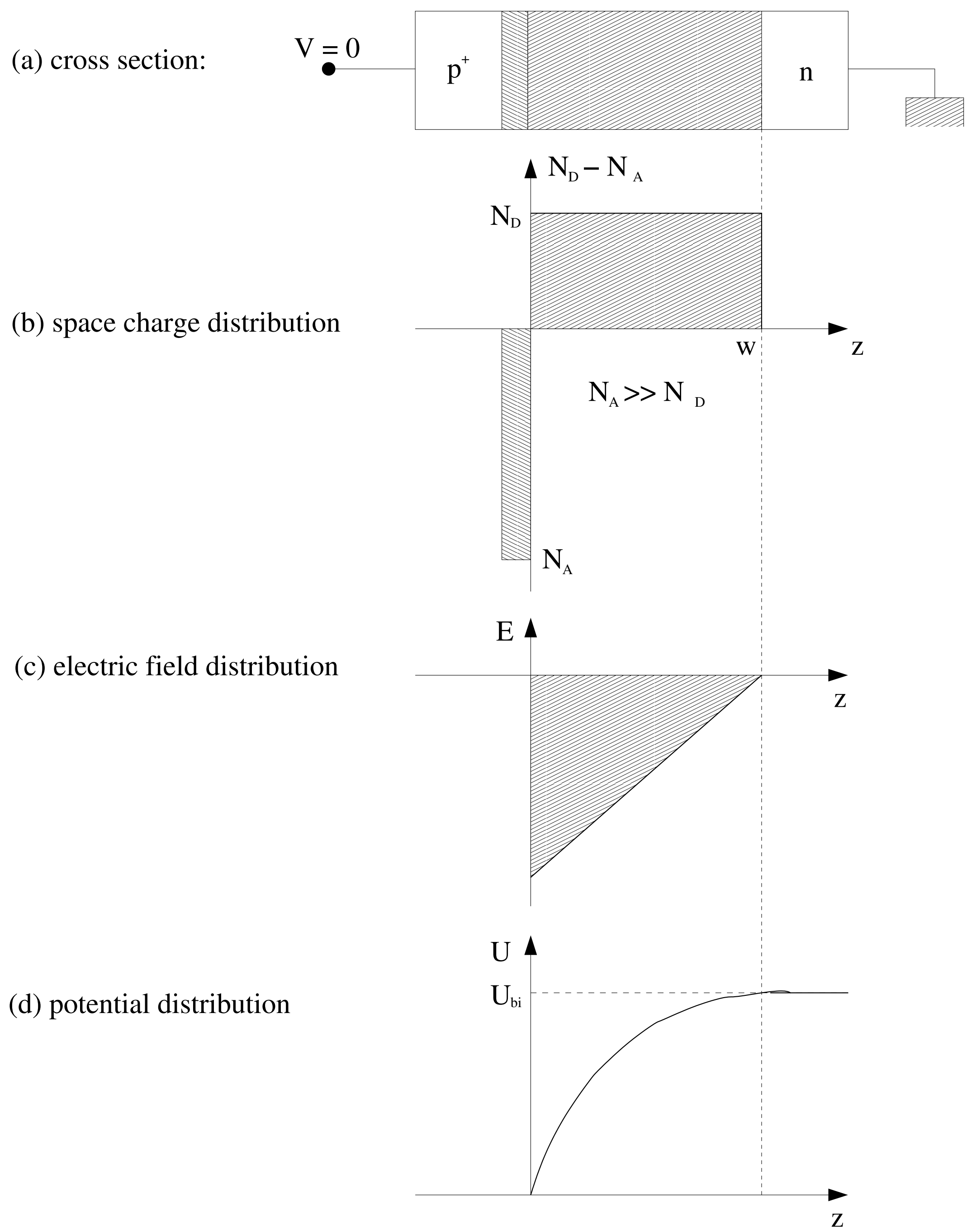

Figure 3.2: *Distributions of a pn-junction: a) one-sided abrupt junction (with $N_A >> N_D$), b) space charge distribution, c) electric field distribution, d) potential distribution [Sze85]*

The constants are the dielectric constant ($\epsilon_0 = 8.85 \cdot 10^{-12}\,\mathrm{As/Vm}$), the relative dielectric constant of silicon ($\epsilon_{Si} = 11.8$), the elementary charge ($q_0 = 1.6 \cdot 10^{-19}\,\mathrm{C}$). $|N_{eff}| = N_A - N_D$ is the effective doping concentration.

Typically high-resistive reverse biased diodes can be fully depleted with approximately 30-600 V. Therefore the whole diode can be used to detect particle tracks.

The electric field in the space-charge region separates the electron-hole pairs created by the traversing particles. The charge carriers move in the electric field to the electrodes. The signals appear already before the arrival of the charges at the electrodes.

3.4 Segmented Silicon Detectors

In order to get spatial information the silicon is segmented in one dimension or two dimensions, examples of which are shown in Fig. 3.3. In high energy particle physics typically strip or pixel designs are implemented, where dimensions are adapted to requirements like occupancy, signal-to-noise, number of readout channel etc.. The strip detector reads out a two dimensional information about the particle track, as the detector is segmented only in one space direction. The pixel detector and the CCD are providing three dimensional spatial information.

Pixel detector

The pixel detector consists of rectangular implantation at the front side and an unsegmented implantation at the back side (compare to Fig. 3.3 (c)). Each pixel of the pixel detector is connected to its own electronics leading to short signal transfer times and low capacitance. Disadvantage of this connection to the electronics is the additional material in the detector. The readout electronic can be found either on the pixel detector itself (active pixel detector) or on a chip connected to the pixel (hybrid pixel detector). Both kinds of detectors are investigated for future collider experiments. The hybrid pixel detector will be used for the vertex detector at ATLAS and CMS (compare to Sect. 2.2). In both cases it consists of a reverse biased diode connected to the electronics via bump bonding.

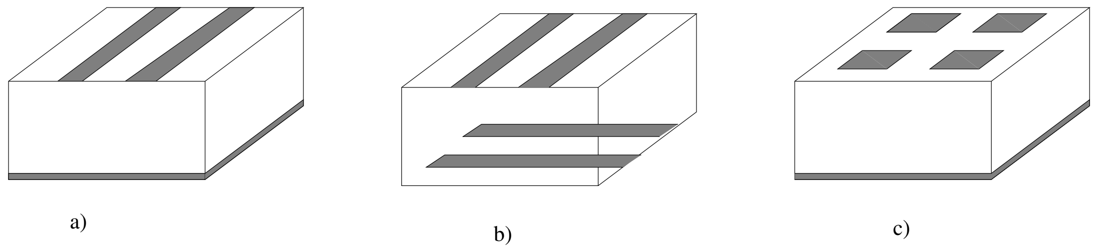

Figure 3.3: *Segmentation of the implantations of semiconductor detectors with position resolution: a) one-sided strip detector, b) double-sided strip detector, c) pixel detector*

Strip detector

Using masks p-strips are implemented in typically n-bulk material. The strips are as long as the sensor; thus providing just two dimensions (Fig. 3.3 (a)). Three dimensional spatial information can be obtained, if the two strip sensors are tilted to each other. These can be achieved by gluing two single sided strip detectors to each other under a small angle or by implanting strips on both sides (compare to Fig. 3.3 (b)). Strip detectors can only be used if the occupancy is not too high as already mentioned in Sect. 2.2. The advantage of strip sensors is that the electronics can be mounted at the sides of the strips.

3.5 Operation of Silicon Detectors

The basic features of silicon sensors have to be optimised for the desired application, in particular for a high-rate environment as at the LHC and radiation damage can occur:

Electric field:

The electric field has to be balanced between the two conflicting parameters:
a high electric field being beneficial to separate the electron hole pairs, however approaching the breakdown limit, on the other hand. As displayed in Fig. 3.2 the electric field changes linearly over the width of the depletion zone. It depends on the position between the electrodes called z-position (compare to Fig. 3.2), the full depletion voltage and the bias voltage applied, it is given by:

$$E(x) = \frac{U_{bias} - U_{depl}}{w} + \frac{2U_{depl}}{w}(1 - \frac{z}{w}). \tag{3.3}$$

Here w is the thickness of the depletion zone, which equals the sensor thickness for a fully depleted sensor. In segmented detectors like strip detector the electric field changes at the segmented side. There are high field regions around the implants and low field regions between the strips. The exact shape of these regions depends on the doping concentration, the geometry of the implants, the thickness of the detector and the applied voltage. Therefore the electric field does not follow the equation defined above in the implanted part of the detector.

The potential distribution parallel to the electric field lines is also shown in Fig. 3.2. Full depletion is defined as the voltage at which the structure is fully depleted meaning the whole detector volume is sensitive for particle detection. This is often not the case after radiation damage. The full depletion voltage can be computed with the help of equation 3.2. One recognizes that the most important dependency is given by the effective doping concentration N_{eff} and the detector thickness d:

$$U_{depl} = \frac{q_0}{2\epsilon_{Si}\epsilon_0} d^2 |N_{eff}| \tag{3.4}$$

Leakage current:

All the currents occuring in a reverse biased diode are named reverse leakage currents. The dominating component is the so-called volume generation current I_{vol}, which results from the separation of the charges generated in the depletion zone, depending on the diode's volume $V = w \cdot A$:

$$I_{vol} = \frac{q_0 n_i A}{\tau_e} \cdot w \propto \sqrt{U_{bias}}. \tag{3.5}$$

This current depends on the area of the diode A and the intrinsic charge carrier concentration n_i. Since the latter is a function of temperature, the leakage current also strongly depends on the temperature. The volume generation current I_{vol} is anti-proportional to the mean free time of electrons τ_e. The mean free time is defined as the average time between collisions with imperfection within the lattice. This corresponds to the average distance of the charge carries between collisions which is called mean free path.

Surface generation current I_{ox} occurs at the surface between silicon and silicon dioxide if crystal defects cause energy band distortions between both. It can cause a leak between the strips and the backplane. Therefore in silicon detectors so-called guard rings around the sensitive area of the sensor prevent this leak.

The diffusion current originates from the minority charge carriers created near the depleted zone, which diffuse in this zone and move to the electrodes due to the reverse bias. As this current depends on the mean free path the diffusion current strongly depends on temperature and the density of impurities. There exist a few silicon detectors operating with mainly diffusion current.

Breakdown currents:
Breakdown currents occur, when the electric field has high values leading to a rapid rise of currents through the diode and consequently a strong heating of the diode. The tunnel effect and the avalanche effect are the main breakdown mechanisms. The tunneling of an electron from the valence band to the conduction band at an electric field above 10^6 V/cm is called the tunnel effect. The resulting current is proportional to an exponential function with the ratio of the band gap energy and the electric field in the exponent. At the avalanche effect, an electron is accelerated by the high electric field, so that it can produce a new electron-hole pair at the collision. Therefore the resulting current depends on the number of collisions and the initial current.

Additional features:
In this section essentially the electrical parameters, like currents are discussed. Other issues being important for the design phase of silicon detectors are neglected because in this thesis the design of the CMS silicon detectors is not under study but the influence of the electrical parameters on the Lorentz angle. The segmentation, resolution and capacitance are not discussed for this purpose.

3.6 Radiation Damage

As already pointed out in Sect. 3.1 beside ionisation radiation damage may occur when a detector is irradiated significantly changing the behaviour of the detector. This section describes the mechanisms of radiation damage as well as their impact on the detector.

Bulk damage and surface damage:
Two different kinds of damage of a silicon device are possible: the bulk damage and the surface damage. Bulk damage is a change of the silicon crystals. Surface damage is the damage concerning the silicon/silicon-dioxide surface. While ionisation in the bulk is reversible and contributes to the signal of the detector, ionisation in the oxide is irreversible and the radiation damage of the surface is due to ionization. A natural distinction is therefore given between surface damage effects, depending on the ionization dose and bulk damage effects depending on the kind of particles, their energy and their number. The bulk damage results in a change of operation parameters, like the depletion voltage. The bulk is changed uniformly over the whole detector volume. During operation this damage can not be cured. Nevertheless it is possible to diminish the changes by improving the material. The surface damage is often a destructive damage, but the parameters of the surface damage are strongly depending on the material and the technology used. For example pinholes might occur, which is an ohmic contact through the dielectric layer. Therefore surface damage is a subject of production quality which needs to be ensured. The effects of surface damage are not discussed in this thesis.

Mechanism of bulk damage:
Particles crossing the silicon sensor might knock silicon atoms out of the crystal lattice sites. These silicon atoms are called primary knock on atoms or recoil atoms. An energy transfer of a displacement threshold energy of at least $E_d = 25\,\mathrm{eV}$ is necessary to remove a silicon atom from the lattice (compare to [vL$^+$80]). In this thesis it will mainly be dealt with particles transfering sufficient energy, so that the recoil atoms can knock secondary silicon atoms out of the lattice leading to a cascade. During this process a significant amount of the recoil energy E_R is lost in ionization. Only a portion $P(E_R)$ contributes to displacements. Although the primary interaction of radiation with silicon is strongly dependent on the type

and energy of the radiation, to a large extend this dependence is smoothed out by the secondary interaction of the primary knock on silicon atoms. Therefore the measurements on radiation damage can be scaled from one type of radiation to another. This scaling is called non ionising energy loss E_{NIEL}:

$$\frac{dE_{NIEL}}{dx} = \frac{N_A}{A} \cdot D(E). \tag{3.6}$$

It is proportional to the displacement damage cross section D(E) [Laz87]:

$$D(E) = \sum_{\nu} \sigma_{\nu}(E) \int_{E_d}^{E_R^{max}} f_{\nu}(E, E_R) P(E_R) dE_R. \tag{3.7}$$

Here the index ν indicates all possible interactions between the incoming particle with energy E and the silicon atoms in the crystal leading to displacements in the lattice. $\sigma_{\nu}(E)$ is the cross section corresponding to the reaction with index ν. The integration is done over all possible recoil energies E_R. $f_{\nu}(E, E_R)$ is the probability density for the production of a primary knock on atom and the energy loss of this atom due to the ionisation of crystal atoms (electron-hole pair creation). To scale the damage efficiency of different particles a hardness factor κ is defined which is normalized to 1 MeV neutrons:

$$\kappa = \frac{\int_{E_{min}}^{E_{max}} \Phi(E) D(E) dE}{D(E_n = 1MeV) \int_{E_{min}}^{E_{max}} \Phi(E) dE} \tag{3.8}$$

Φ is the fluence of the particles.

There are two different kinds of bulk damage: point defects and cluster defects. Defects are point defects as long as individual silicon atoms in a lattice leave the lattice structure of the semiconductor. Contrarily a cluster defect corresponds to a region with a high number of local point defects, where the whole lattice structure is deformed. The energy bands are bent as a result of the high defect density.

Point defects show two different defect types: interstitials (I) and vacancies (V). These two primary types of defects are mobile and can create secondary defects while moving. The secondary defects are for example point defects like closed pair, e-center like VP or VB, a-center like VO, ... and divacancies (VV). The defect types are sketched in Fig. 3.4. These defects create new energy bands between the valence band and the conduction band.

Effects on the behaviour of a silicon detector:
The defect levels have several effects on the electrical behaviour of semiconductor devices:

- Defect levels near the middle of the band gap increase the recombination and generation. Therefore the leakage current of the semiconductor device increases.

- Trapping centres near the conduction band influence the electrical behaviour in a twofold way: On one hand they trap the charge carriers and release them in a delayed way, and hereby decrease the charge collection and increase the noise in the silicon crystal. On other hand they compensate the acceptors (donators) or create themselves acceptors (donators). The change of the acceptor-donator ratio modifies the effective doping concentration N_{eff} and therefore the full depletion voltage. The change of doping concentration can be parametrised [Wun92]:

$$N_{eff}(\Phi) = N_{D,0} \cdot exp(-c_D\Phi) - N_{A,0} \cdot exp(-c_A\Phi) - b\Phi. \qquad (3.9)$$

  In equation 3.9 $N_{D,0}$ and $N_{A,0}$ are the donator and acceptor concentrations before radiation, c_D and c_A are the removal rates, b ist the increase of acceptor-like states after radiation. Given an n-doped sensor the effective doping concentration decreases during irradiation until it reaches a minimum. At higher radiation the material is converted from n-conducting to p-conducting material, the so-called bulk conversion. The depletion voltage changes during this process.

Beside these known changes some other changes of silicon sensors' characteristics due to bulk damage have been discussed since a few years: the change of the mobility and the change of the electric field.

The dependence of the mobility on the irradiation dose is still controversial. In Ref. [E$^+$95] no significant changes were observed in the transport properties of both electrons and holes up to $0.5{\cdot}10^{14}$ 1 MeV n/cm^2 and a prediction is made that a fluence of at least approximately 10^{15} 1 MeV n/cm^2 is necessary to significantly affect the carrier drift mobilities. In Ref. [B$^+$99] the mobility for both carrier types in irradiated sensors agree with those for the non-irradiated

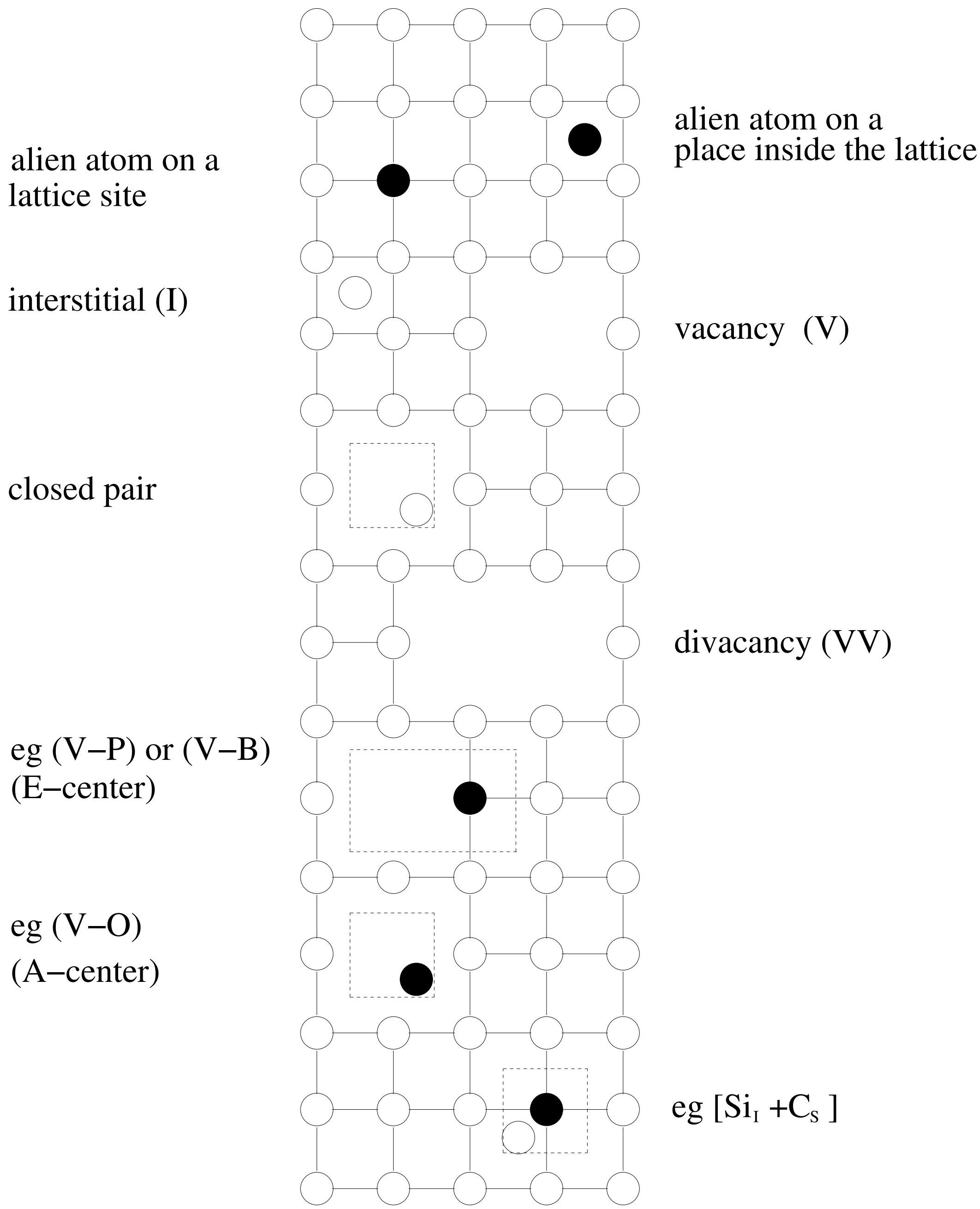

Figure 3.4: *Schematic sketch of some point defects in the silicon lattice [Wun92]*

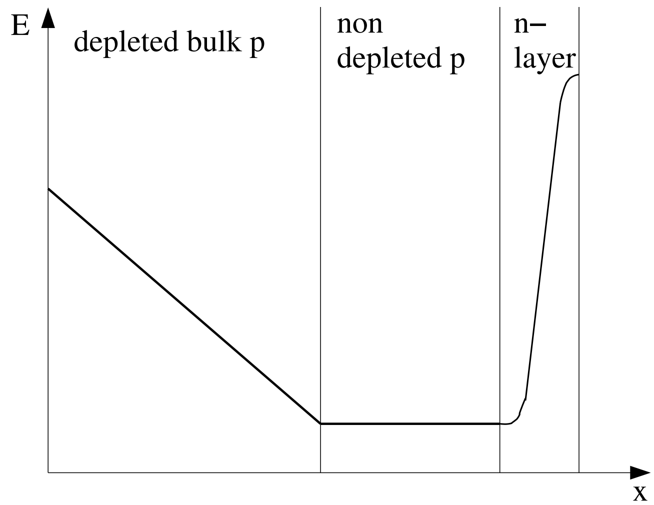

Figure 3.5: *Schematic diagram of the electric field pattern inside an irradiated detector deduced from [B+98]*

sensor within errors for fluences up to $2{\cdot}10^{14}$ 1 MeV n/cm^2. In contrast, a change of mobility after irradiation for holes and electrons was observed in Ref. [L+99]. The mobility μ_{low} of holes changes slightly from 470 cm^2/Vs to about 460 cm^2/Vs after irradiation to a fluence of 10^{13} 1 MeV n/cm^2. Above this fluence, the mobility does not change any more, and therefore it can usually be neglected. The mobility μ_{low} of the electrons changes more significantly from 1417 cm^2/Vs to 1000 cm^2/Vs.

Furthermore the so-called double junction effect arises in an irradiated detector. That means that the electric field behaves as if there were two junctions. The electric field inside the detector is schematically depicted in Fig 3.5. It is similar to that for a uniform space charge in the depleted region falling to near zero at the edge of the depleted region. There is also a strong local field in the vicinity of the electrode at the p^+ side and a non-zero field region near the p^+ side and the depleted region. The double junction effect has been observed (for example [B+98] and [C+99]). A modelling of this effect is difficult, although first attempts have already been made. A trend can be observed that the higher the bias voltage the less pronounced is the double junction effect. The double junction effect can decrease the charge collection efficiency. In the non-depleted area, the charge carriers diffuse through the detector without a tagged direction. Therefore these charge carriers have a high probability to be trapped and in the non-depleted region charge carriers accumulate, therefore charge between two strips can be shared.

As figured out earlier the mobility of the defects is temperature dependent. So above an annealing temperature the defects transform even after irradiation in more stable defects.

3.7 The CMS Silicon Sensors

To give an example of a silicon detector system, the CMS silicon sensors are presented. The change of characteristics after the anticipated radiation damage in the LHC environment is summarised. Both silicon strip sensors and silicon pixel sensors will be operated at -10°C in order to reduce the effects of radiation damage. Only in short maintenance periods they will be exposed to room temperature.

Silicon strip detector:
The schematic structure of the CMS silicon strip sensors is shown in Fig. 3.6. Before bulk conversion, the silicon tracker is of n-type substrate doped with phosphorus. At the back plane, an n^{++} layer serves as Ohmic contact. On the other side p^{++} strips are implanted. Applying an electric field across the bulk, results in the collection of holes on the p^{++} strips. The signal on the strips couples through a thin layer of SiO_2 to the Aluminium readout strips, which are connected to an amplifier. Each strip is connected to the bias ring, which surrounds the whole structure, via a bias resistor realised by poly-silicon deposition with a wiggle-shaped structure doped with phosphorus. The strips are directly connected to the read-out electronics. Charge transfer is realised by a thin silicon oxide layer and silicon nitride layer covering the whole silicon area and aluminium strips just above the p^{++} implants. The multi layer structure avoids the occurence of pinholes. The aluminium contacts are slightly broader than the implants and therefore reduce the field strength at the implant, since some field lines end in the metal overhang. The coupling through the oxide layer protects the read-out electronics from high leakage currents. All these efforts results in a high breakdown voltage.

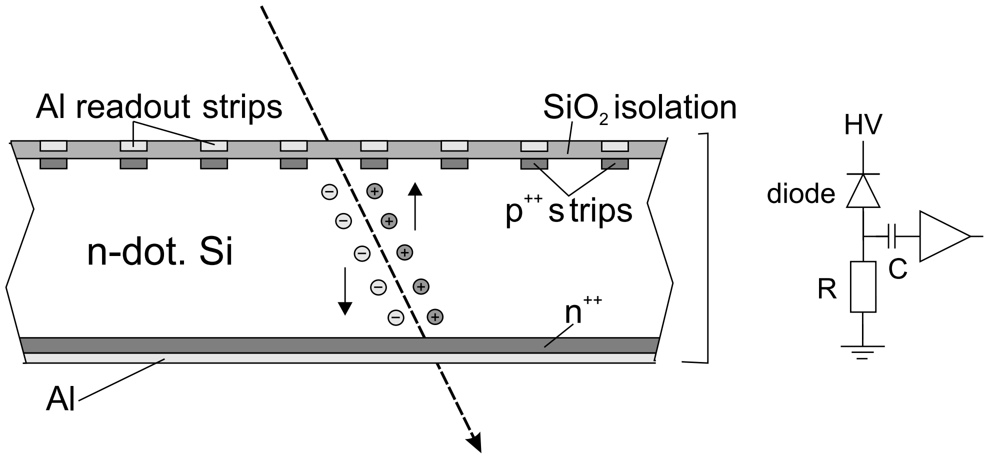

Figure 3.6: *Schematic structure of CMS silicon strip sensors*

The silicon tracker of CMS can be divided into an inner tracker, which consists of an inner barrel and an inner endcap, and an outer tracker, which consists of an outer barrel and an outer endcap. The sensors for the inner tracker will have a bulk resistivity of $\rho = 1.5\text{-}3\,\text{k}\Omega\text{cm}$ and a thickness of $d = 320\,\mu\text{m}$, whereas the outer tracker will have a bulk resistivity of $\rho = 3.5\text{-}6\,\text{k}\Omega\text{cm}$ and a thickness of $d = 500\,\mu\text{m}$. The $500\,\mu\text{m}$ thick sensors have strip pitches, that means distances between the implants, between 122 and $205\,\mu\text{m}$, the $320\,\mu\text{m}$ thick sensors have strip pitches between 80 and $158\,\mu\text{m}$. The ratio of strip width to strip distance is 0.25 for all layouts. This is a compromise between lower electric field peaks at the edges of the implants at smaller values and better resolution at higher values of the ratio. The maximum fluences, to which the silicon strip detectors of CMS are exposed, reach about $2{\cdot}10^{14}\,1\,\text{MeV}\,\text{n/cm}^2$ in the innermost layer at the expected luminosity of $500\,\text{fb}^{-1}$. The radial dependence of the particle flux in the silicon tracker is shown in Fig. 3.7.

The expected maximal final full depletion voltage for the highest fluence level reaches $\approx 350\,\text{V}$ [Mig01] after conversion of the material, [F$^+$00]. So the silicon strip detectors can still be operated in overdepletion, since the breakdown voltage is specified to be at least 500 V. This small change of depletion voltage is due to the fact that the doping of the bulk is converted. Therefore the difference between the full depletion voltage is 850 V in total. The change of the full depletion voltage is depicted in Fig. 3.8, demonstrating the small change in depletion voltage during the operation at -10°C. But after the maintenance periods the

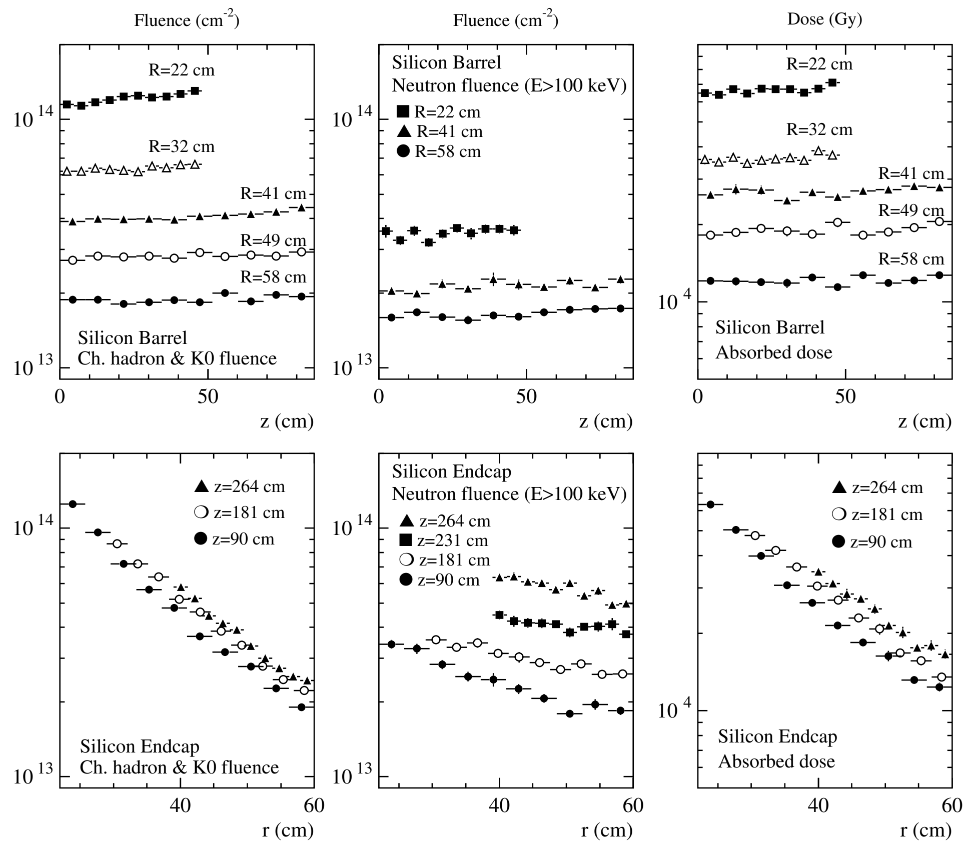

Figure 3.7: *Energy-integrated charged hadron and neutron fluences and absorbed dose in the silicon tracker. All values are for an integrated luminosity of* $5 \cdot 10^5$ pb^{-1}.

depletion voltage changes drastically as can be seen in the sharp peaks in Fig. 3.8. This is due to the fact that the constants in Eq. 3.9 are dependent on temperature.

Silicon pixel detector:

The fluence amounts up to about $2{\cdot}10^{15}$ 1 MeV n/cm^2 for an integrated luminosity of 500 fb^{-1}, which the pixel sensors have to stand. The distribution of the fluences over the silicon pixel detector is shown in Fig. 3.9.

The design phase of the pixel detector is still ongoing. The thickness of the sensors will presumably be 250 μm, the pixel dimensions 150 μm x 150 μm. A maximum bias voltage of about 300 V is foreseen. Due to the high radiation dose that close to the beampipe, type-inversion will occur very early in the

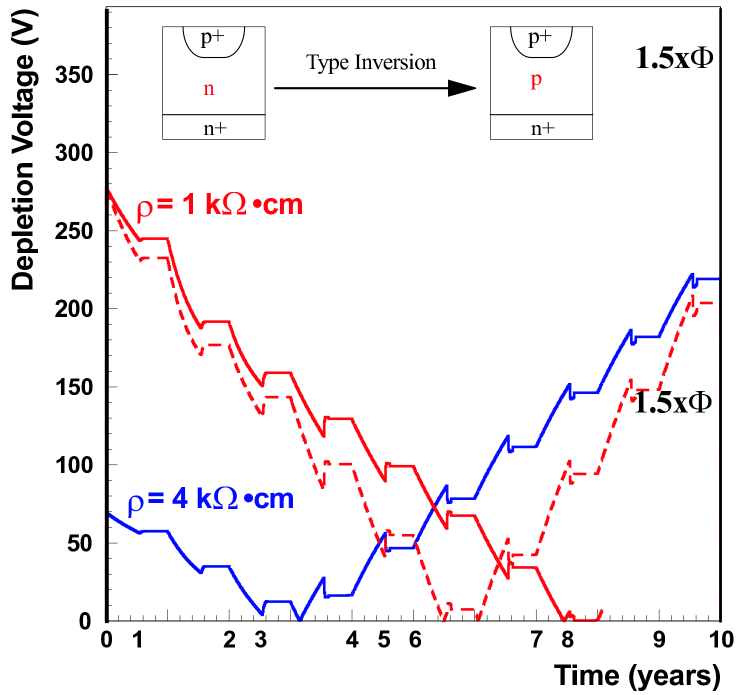

Figure 3.8: *Depletion voltage for silicon sensors of three different thicknesses and a resistivity of 1 and 4 kΩcm as function of time and therefore of the fluence Φ. In these calculations a maintenance scenario with the detector at 10° C during 10 days per year was assumed. [ADD00]*

experiment. Therefore n-side readout will be used, which after inversion can operate partially depleted as p-on-n silicon.

Fig. 3.10 shows that the full depletion voltage after a fluence of $3.6{\cdot}10^{14}$ pions/cm^2 of 300 MeV/c is about 500 V and would have to be increased to 1500 V after a fluence of $9{\cdot}10^{14}$ pions/cm^2 of 300 MeV/c. So the sensor cannot be fully depleted after exposure to these fluences and has to be operated below full depletion.

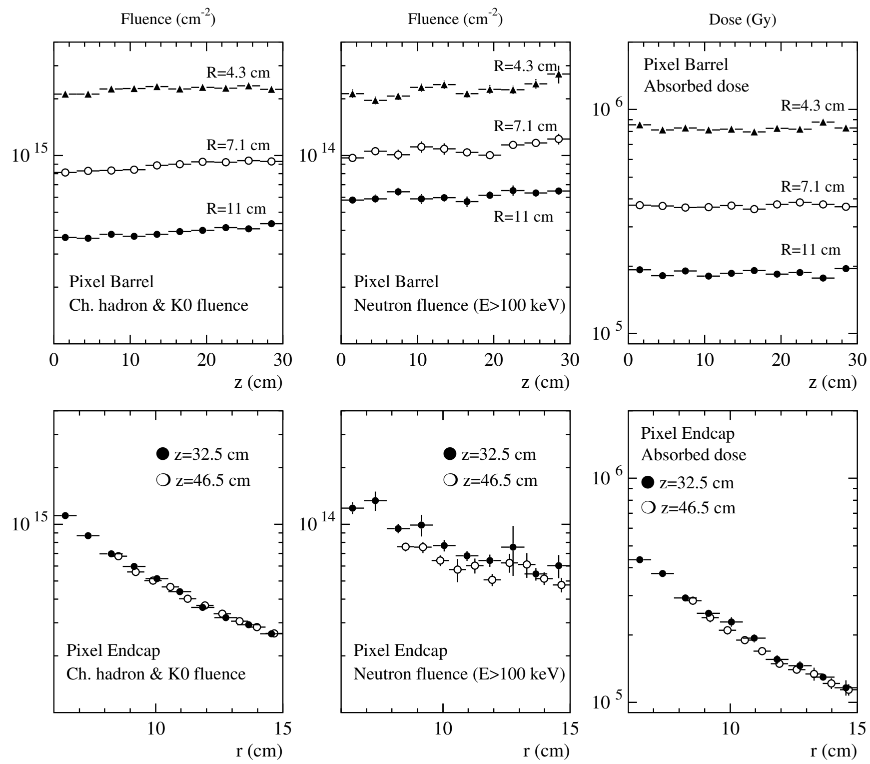

Figure 3.9: *Energy-integrated charged hadron and neutron fluences and absorbed dose in the pixel detector. All values are for an integrated luminosity of 500 fb*$^{-1}$.

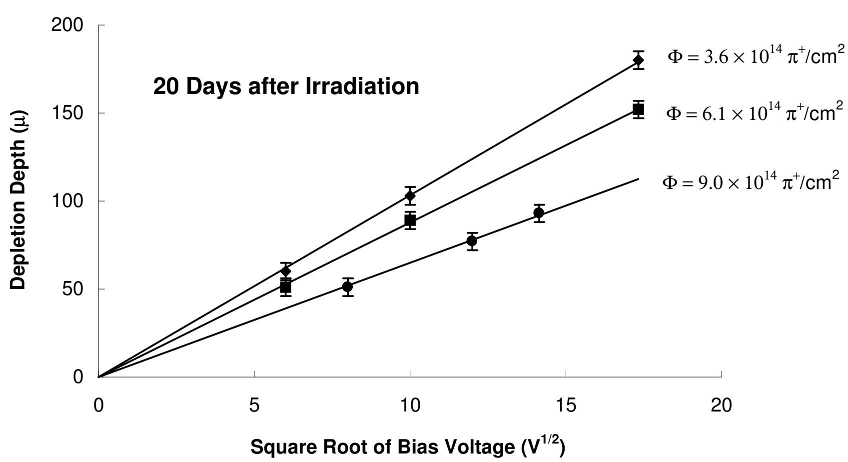

Figure 3.10: *Depletion depth versus bias voltage for prototype pixel detectors*

Chapter 4

Algorithm for Calculating the Lorentz Angle in Silicon Detectors

4.1 Theoretical Introduction

The silicon tracker of CMS is positioned inside the magnet. This 4 T magnetic field will cause a Lorentz shift of the charge carriers in the silicon such that the potentially reconstructed track would be shifted with respect to the passed particle position. Therefore this shift needs to be considered for the reconstruction of the charge carriers and a detailed study of this shift is done.

In a magnetic field the charge carriers are affected by a threefold force: The electric force F_{el}, the Lorentz force F_L and the effect of collisions called relaxation:

$$\vec{F} = F_{el} + F_L + m_e^\star \frac{\vec{v}}{\tau} = e\vec{E} + e(\vec{v} \times \vec{B}) + m_e^\star \frac{\vec{v}}{\tau}. \tag{4.1}$$

The first two forces are of fundamental nature. The third force describes the effect of relaxation scattering of charge carriers where τ is the mean free time between two collisions and $m_e^\star$ is the effective mass of the bounded electron. An electron in the conduction band is similar to a free electron, meaning it is relatively free to move around in a semiconductor. However, because of the periodic potential of the nuclei, the effective mass of a conduction electron is different from the mass of a free electron. From the Eq. 4.1 one can see that the Lorentz force $\vec{F_L}$ deflects the charge carriers perpendicular to the electric field without changing the value of the drift velocity (see Fig. 4.1). The Lorentz angle Θ_L by which charge carriers are deflected is defined by:

$$\tan(\Theta_L) = \frac{\Delta x}{\Delta z} = \mu_{\mathrm{H}} B = r_{\mathrm{H}} \mu B \tag{4.2}$$

where Δz corresponds to the detector thickness and Δx to the shift of the signal position. If the ionisation is produced at the surface, the drift distance corresponds to the detector thickness. If the ionisation is homogeneously produced by a traversing particle, the average drift distance is only half the detector thickness. The Hall mobility is denoted by μ_{H}, the conduction mobility by μ. The Hall mobility differs from the conduction mobility by the Hall scattering factor r_{H}. This factor describes the influence of the magnetic field on the mean free path of carriers of different energy [Smi68]. For small magnetic fields, for which the condition ($\mu B \ll 1$) holds, r_{H} can be calculated according to the Boltzmann transport theory [See73, Bla85]:

$$r_{\mathrm{H}} = \frac{<\tau^2>}{<\tau>^2} \tag{4.3}$$

At a magnetic field of 4 T, as proposed for the CMS detector and mobilities of less than 2.500 cm^2/Vs, the magnetic field can still be considered to be small and therefore the Boltzmann approximation is valid. Here the Hall scattering factor has a value of ≈ 0.7 for holes and ≈ 1.15 for electrons at room temperature.

The mobility μ increases with temperature proportional to $T^{-2.5}$ for holes and $T^{-2.2}$ for electrons [Sze85]. The hole mobility is about 470 cm^2/Vs at 300 K, the electron mobility is about 1417 cm^2/Vs at 300 K. Thus the drift mobility of electrons is about three times larger than the hole mobility. Consequently the Lorentz shift is significantly larger for electrons than for holes. So p-side readout shows a considerably smaller Lorentz shift than n-side readout, because the holes move to the p-side and the electrons to the n-side. Still the Lorentz shifts for holes reach about 40 μm (70 μm) in a magnetic field of 4 T for a 320 μm (500 μm) thick detector as it is used in CMS, so that the shifts need to be considered in the track fit.

Another important question is the dependence of the Lorentz shift on the irradiation dose. The change of drift mobility and the change of the electric field in the silicon detector due to defects introduced by the radiation damage results in

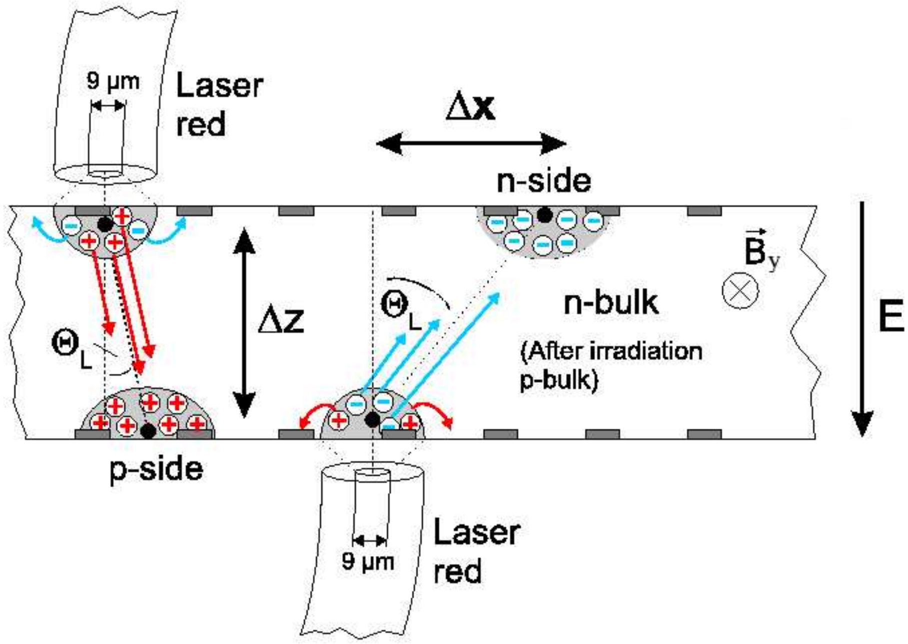

Figure 4.1: *The figure shows the principle of the Karlsruhe setup to measure the Lorentz angle of holes and electrons [dB+01]. It is equipped with two fibres delivering laser light to the silicon. The red lasers have a penetration depth of a few μm, so with a laser pulse on the n-side or p-side one can measure the drift from electrons and holes, respectively.*

a change of the Lorentz shift and thus of the calibration of the detector. These changes are considered in the next sections.

4.2 Experimental Setup

A comprehensive study of Lorentz shifts of non-irradiated and irradiated sensors was performed at Karlsruhe [dB+01, R̈98, Hei99, Hau00]. The Lorentz angle was measured for electrons and holes separately. For a temperature range of 77 K-300 K charges were injected at the surface on one side and their drift through the sensor was observed by measuring their position on the opposite side (see Fig. 4.1). Alternative methods are described in [B+83, Ale00].

Examples of measured signals are shown in Fig. 4.2 [Die03]. On the left hand side the signal generated by a red laser is shown, whereas on the right hand side the signal generated by a infrared laser is shown. One can see that the barycenter

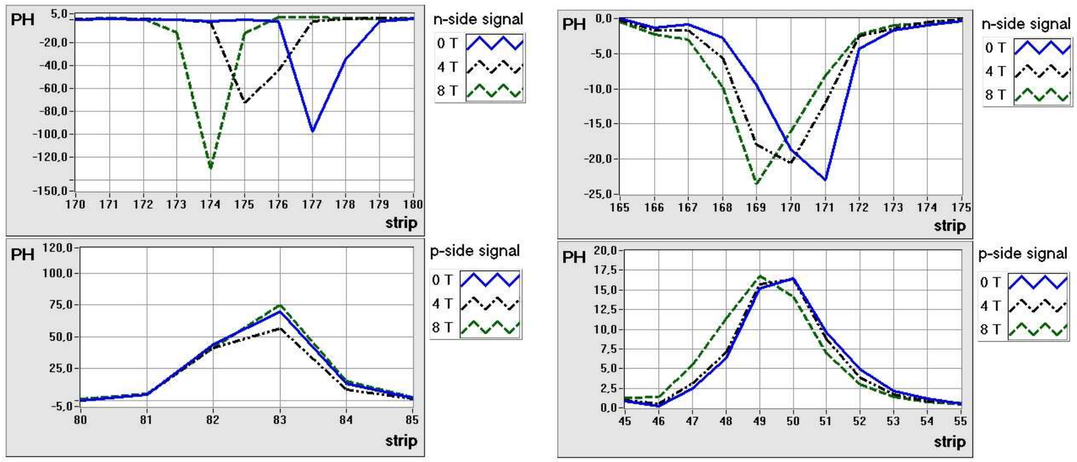

(a) (b)

Figure 4.2: *Comparison of signals generated by an infrared and red laser for a magnetic field of 0 T, 4 T and 8 T [Die03]. The total shift is the distance between the barycenter of the signal at 0 T and the barycenter at 4 T or 8 T. The shift of the signal generated by the infrared laser on the n-side, where electrons are collected, is about half the shift of the signal generated by the red laser. (a) 1060 nm Laser, about -10° C (b) 660 nm Laser on the p-side, about -25° C*

of the signal generated by the infrared laser is shifted about half of the distance that the signal of the red laser is shifted.

Charges are generated by injecting laser light with a wavelength of $\lambda \approx 650\,\mathrm{nm}$, which has an absorption length of $\approx 3\,\mu\mathrm{m}$ at 300 K. In this case charge carriers of one type (e.g. electrons) are collected at the nearest electrode, whereas the carriers of the other type (e.g. holes) drift towards the opposite side. This allows the measurement of the Lorentz angle for electrons and holes separately by injecting laser light either on the p- or n-side. The laser from Fermions Lasertech [fer] has a maximum power of 1 mW, which could be regulated with the pulse height and width of the input pulse to the laserdiodes. Typically a laser pulse with a width of 1 ns was generated. The laser pulse was sent to the sensor via a single-mode fibre with an inner diameter of a few microns.

For the measurements, the JUMBO magnet from the Forschungszentrum Karlsruhe [H$^+$99] was used in a $B \leq 10\,\mathrm{T}$ configuration with a warm bore of

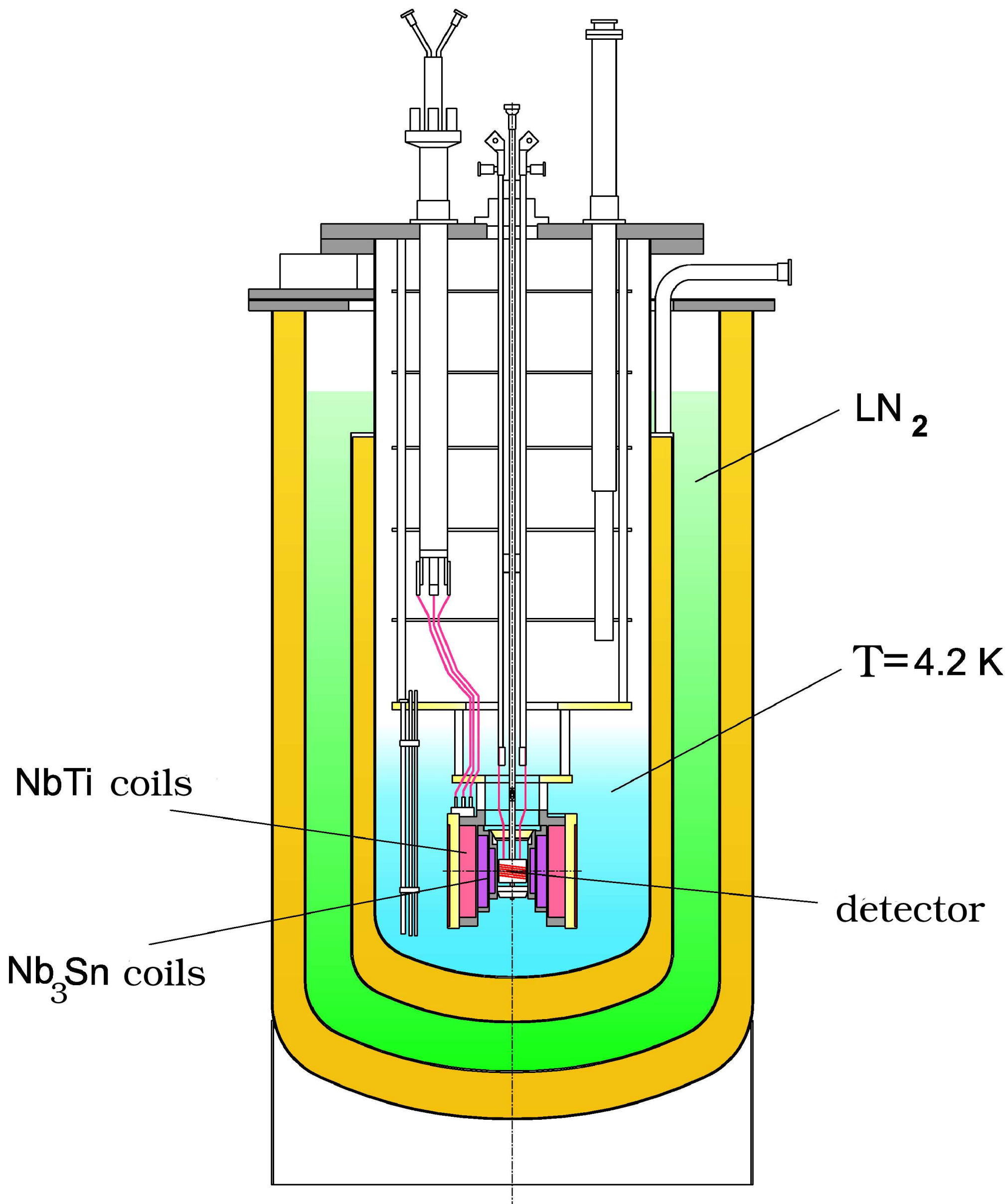

Figure 4.3: *Cross section of the JUMBO magnet. It consists of a vacuum chamber surrounding a chamber with liquid nitrogen LN_2, another vacuum chamber and finally the supraconducting coils. The liquid nitrogen chamber is operated at 77 K, the supraconducting coil is cooled with helium to 4.2 K. [H^+99]*

72 mm. The magnet consists of supraconducting $NbTi$ and Nb_3Sn coils, which are cooled with liquid helium. For an efficient cooling, the cryostat is built out of several isolating chambers as depicted in Fig. 4.3.

The sensors are double sided microstrip detectors of a size of approximately $2{\times}1\,\mathrm{cm}^2$ from the HERA-B production by Sintef [A+01]. They have a strip pitch of $50\,\mu$m on the p–side and $80\,\mu$m on the n–side; the strips on opposite sides are oriented at an angle of 90° with respect to each other. The capacitively coupled readout strips are connected to the bias ring through a $1\,\mathrm{M}\Omega$ resistor. The readout chip used for the readout of the strip detectors is the Premux128-Chip with a shaping time of 45 ns [Jon95]. The chip's common mode is suppressed by a double correlated sampling technique, which substracts the signal's baseline. The threshold could be adjusted. The signal to noise ratio from the laser pulse, corresponding to a few times the signal of a MIP, was sufficiently high, so that the thresholds were not critical.

The averaged signal position $\bar{x}$ is computed from either a fit with the sum of two Gaussians one modelling the signal to noise ratio and the second on the pulse heights or from the center of gravity of the pulse heights p_i on neighbouring strips x_i, i.e. $\bar{x} = \sum p_i \cdot x_i / \sum p_i$. Both methods gave comparable results. The first method has been selected for the studies. A detailed description can be found at [Hei99, Hau00].

The signal position is plotted as function of the magnetic field in Fig. 4.4, which shows clearly the dependence of the Lorentz shift on the strength of the magnetic field up to 9 T. This implies that Eq. 4.2 can be used for the 4 T magnetic field of CMS.

Before irradiation, the sensor depletes fully at a bias voltage of 40 V, while after irradiation with $1.0{\cdot}10^{13}\,1\,/\,\mathrm{cm}^2$ protons of an energy of 21 MeV, the depletion voltage increased to 100 V. This implies that the bulk is inverted from n-type to p-type material, as expected [Ros01]. The bulk damage of 21 MeV protons is about 2.1 times the damage from 1 MeV neutrons [Huh01]. Numerical results on the Lorentz angles and shifts are displayed in Figs. 4.5 and 4.6 before and after irradiation, respectively.

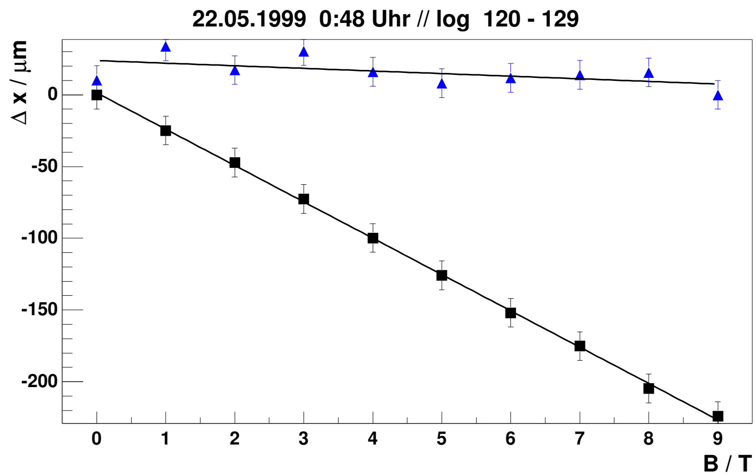

Figure 4.4: *The Lorentz shift of electrons (top curve) and holes (lower curve) shift versus the magnetic field. The red laser (≈ 650 nm) pulse on the n-side side hardly penetrates, so the electrons are immediately collected by the neighbouring strips on the n-side and the holes drift through the detector to the p-side. Therefore a significant shift is only seen for the holes. The temperature is 166K, the bias voltage 150V.*

The Lorentz shift for holes does not strongly depend on irradiation as shown in Fig. 4.5, while for electrons there is a clear dependence on the irradiation dose as shown in Fig. 4.6. The calculated values in the Figures are discussed in the next section. The strong decrease of the Lorentz shift for electrons after irradiation for bias voltages below 100 V originates from the fact that the detector is not depleted for these voltages any more, thus the Lorentz angle is only computed in the depleted zone as will be discussed in section 4.3.

4.3 Algorithm for the Compensation of the Lorentz Angle in Silicon Strip Detectors

The algorithm for the Lorentz angle in silicon sensors has already been published in [B+03] and [B+01] under CMS specific aspects.

At moderate irradiation doses, detectors usually can be operated at full depletion or overdepleted. However, for pixel detectors located close to the LHC beampipe,

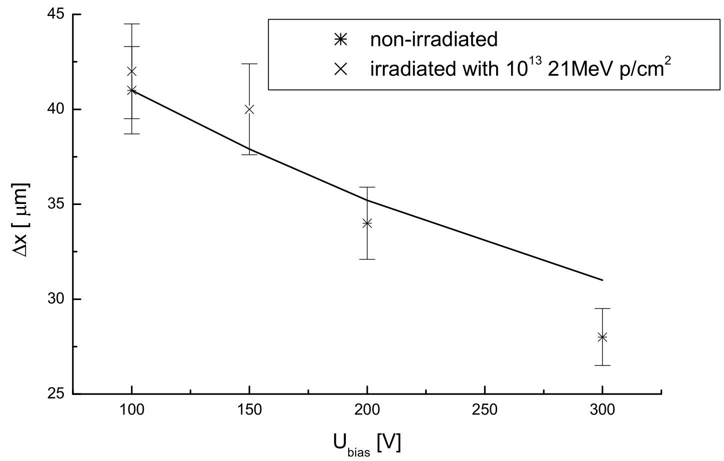

Figure 4.5: *The Lorentz shift Δx for holes generated at the surface for a 300 μm thick sensor in a 4 T magnetic field versus bias voltage U_{bias}. The bars represent systematic errors. The temperature is 260 K. The line is calculated according to the algorithm discussed in the text.*

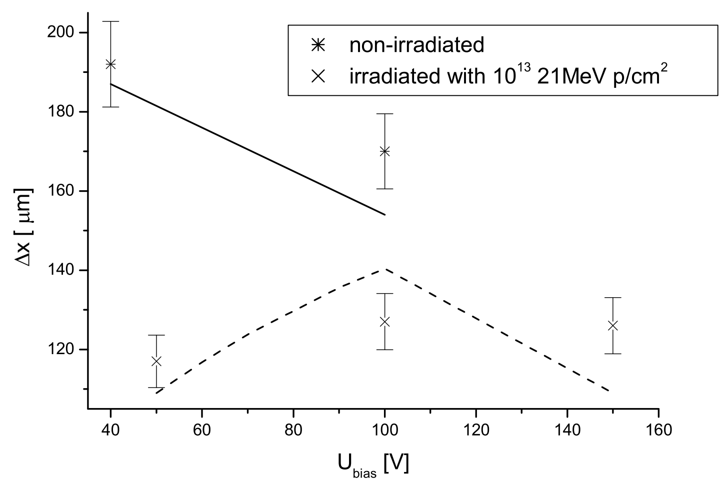

Figure 4.6: *The Lorentz shift Δx for electrons generated at the surface for a 300 μm thick sensor in a 4 T magnetic field versus bias voltage U_{bias}. The bars represent systematic errors. The temperature is 280 K. The lines are calculated according to the algorithm discussed in the text.*

non-irradiated					irradiated with $10^{13}\,$p/cm^2			
U_{bias} [V]	Δx [μm] (270 K)	Δx [μm] (260 K)	Θ_{meas} (270 K)	Θ_{sim} (270 K)	U_{bias} [V]	Δx [μm] (260 K)	Θ_{meas} (260 K)	Θ_{sim} (260 K)
100	38	41	7.2°	7.2°	100	42	8.0°	7.8°
200	31	34	5.9°	6.1°	150	40	7.6°	7.2°
300	25	28	4.8°	5.3°				

Table 4.1: *The Lorentz shift Δx for holes for a 300 μm thick detector in a 4 T magnetic field as function of bias voltage for a non-irradiated detector and an irradiated detector. The detector was irradiated with 21 MeV protons up to a fluence of 10^{13} p/cm^2. The full depletion voltages are 40 V for the non-irradiated detector and 100 V for the irradiated detector. The Lorentz shift for the non-irradiated detector was measured at 270 K and corrected to 260 K using Eq. 4.2, 4.4, 4.5. In addition, the calculated Lorentz angle Θ_{sim} is given.*

non-irradiated				irradiated with $10^{13}\,$p/cm^2			
U_{bias} [V]	Δx [μm] (280 K)	Θ_{meas} (280 K)	Θ_{sim} (280 K)	U_{bias} [V]	Δx [μm] (280 K)	Θ_{meas} (280 K)	Θ_{sim} (280 K)
40	192	33°	32°	50	117	21°	20°
100	170	30°	27°	100	127	23°	25°
				150	126	23°	22°

Table 4.2: *The Lorentz shift Δx for electrons for a 300 μm thick detector in a 4 T magnetic field as function of bias voltage for a non-irradiated detector and an irradiated detector. The detector was irradiated with 21 MeV protons up to a fluence of 10^{13} p/cm^2. The full depletion voltages are 40 V for the non-irradiated detector, 100 V for the irradiated detector. Θ_{sim} was obtained from the algorithm developed in Chapter 4.3.*

this is often not possible due to radiation damage, as discussed in Sect. 3.6. I first discuss an algorithm to calculate the Lorentz angle at full depletion, while the case without full depletion will be discussed in Sect. 4.4. In this section I first discuss the calculation of the Lorentz shift correction for non-irradiated sensors and then the changes needed for moderately irradiated sensors which still can be fully depleted.

Non-irradiated sensors

The mobility $\mu(E)$ is proportional to the mobility at low electric field μ_{low}. It decreases with an increasing electric field until it saturates. This behaviour is depicted in Fig. 4.7. Here, instead of the mobility, the drift velocity $v(E) = \mu(E) \times E$ is plotted against the electric field at several temperatures. From these plots, the behaviour of the mobility has been parametrised as [C+75]:

$$\mu(E) = \frac{\mu_{\mathrm{low}}}{(1 + (\frac{\mu_{\mathrm{low}} E}{v_{\mathrm{sat}}})^{\beta})^{\frac{1}{\beta}}} \tag{4.4}$$

The value β is a fitting parameter, whereas the value v_{sat} has the physical meaning of a saturation velocity, which is obtained at large electric fields. For holes, the parameter values determined in reference [C+75] are used:

$$\mu_{\mathrm{low}} = 470.5 \frac{cm^2}{Vs} \cdot \left(T/300K\right)^{-2.5}$$

$$\beta = 1.213 \cdot \left(T/300K\right)^{0.17}$$

$$v_{\mathrm{sat}} = 8.37 \cdot 10^6 cm/s \cdot \left(T/300K\right)^{0.52}$$

while for electrons the following values are determined by [C+75]:

$$\mu_{\mathrm{low}} = 1417 \frac{cm^2}{Vs} \cdot \left(T/300K\right)^{-2.2}$$

$$\beta = 1.109 \cdot \left(T/300K\right)^{0.66}$$

$$v_{\mathrm{sat}} = 1.07 \cdot 10^7 cm/s \cdot \left(T/300K\right)^{0.87}$$

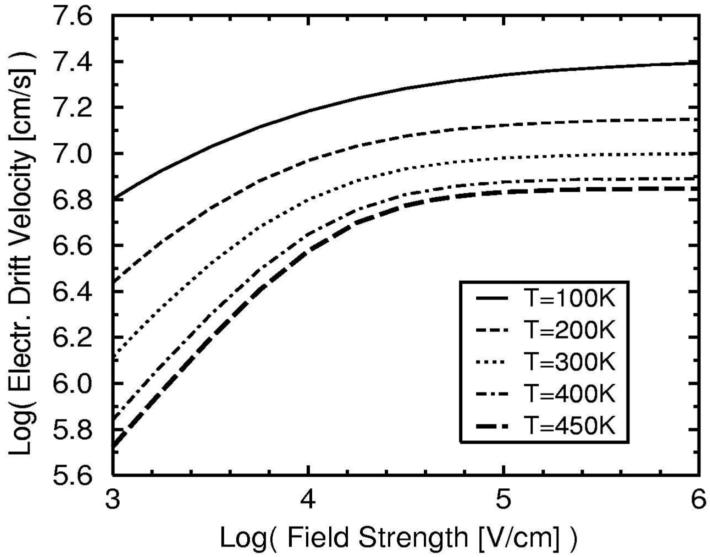

Figure 4.7: *Drift velocity plotted against field strength for several temperatures. [C+75]*

The electric field $E(z)$ given by Eq. 3.3 is only an approximation for highly segmented detectors because of the perturbation of the field near the highly doped collection zones of a thickness of a few μm. Since these zones are only a few per cent of typical sensor thickness of 300 or 500 μm. The average electric field can be calculated from Eq. 3.3 to be:

$$E_{\text{mean}} = \frac{E(z=0) + E(z=w)}{2} = \frac{U_{\text{bias}}}{w} \tag{4.5}$$

This E_{mean} is independent of the depletion voltage. The electric field $E(z)$ is not constant in a sensor. For full depletion it varies from $2\,U_{\text{depl}}/w$ to zero. For large values of U_{depl} the electric field $E(z)$ can change from the saturation regime to zero with a correspondingly strong change in the mobility. The total Lorentz shift can be obtained by integrating Eq. 4.2 over the thickness of the sensor using at each position the mobility given by Eq. 4.4. For small depletion voltages the use of an average electric field and corresponding mobility is sufficient to calculate the Lorentz shift from Eq. 4.2. In addition, for electrons the nonlinear saturation regime is reached at lower fields than for holes, because of the higher ratio $\mu_{\text{low}}/v_{\text{sat}}$ in Eq. 4.4. This difference in nonlinearity between electrons and

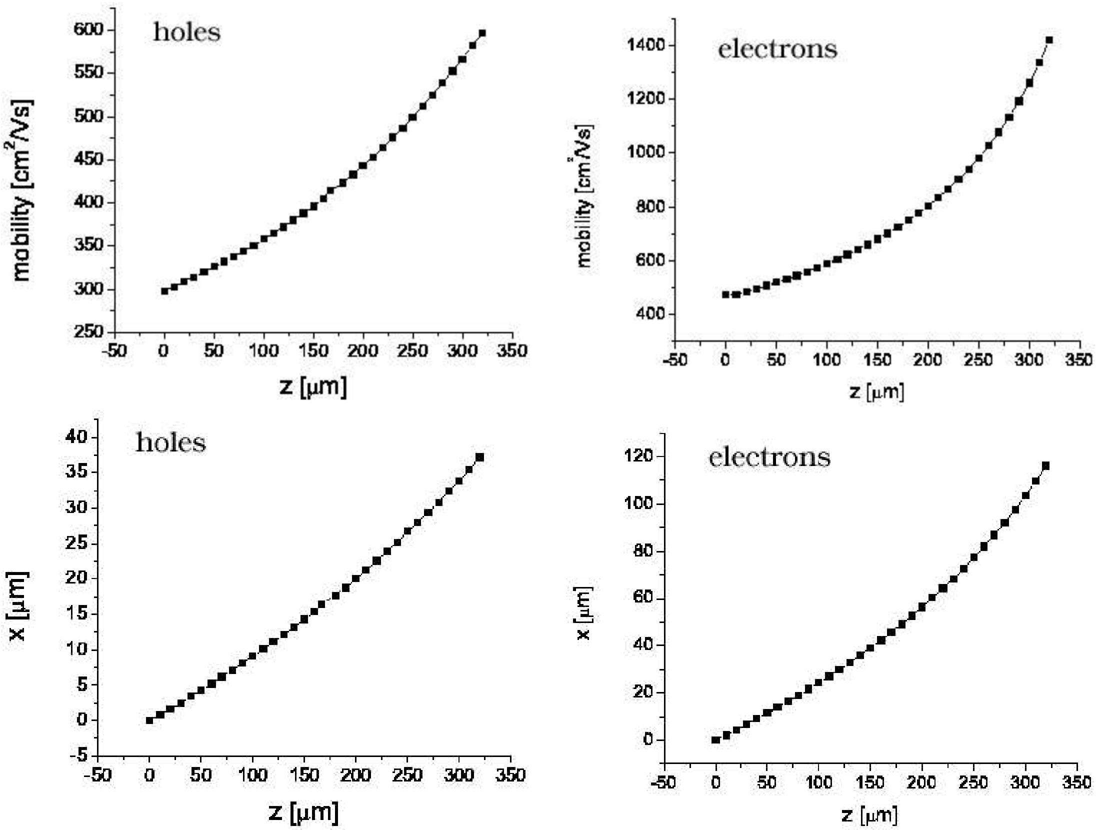

Figure 4.8: *Simulated mobility (top curve) and mean trajectory (lower figure) of holes (left hand side) and electrons (right hand side) at a full depletion voltage of 280 V and a bias voltage of 350V at a temperature of 263 K in a 4 T magnetic field. The thickness of the sensors is 320 µm. The total Lorentz shift for holes is 37 µm, for electrons 116 µm, the total shift calculated with a mean electric field for holes is 36 µm, for electrons 104 µm.*

holes is displayed in Fig. 4.8 for a sensor with a large depletion voltage of 280 V.

Given the electric field, the mobility can be calculated from Eq. 4.4 and the corresponding Lorentz shift from Eq. 4.2. Figs. 4.5 and 4.6 show that the calculations match the measurements quite well. The figures also show the calculated Lorentz angle as a function of the bias voltage. The dependence is approximately linear for fully depleted sensors.

In the case of CMS silicon strip detectors the sensors are biased with a volt-

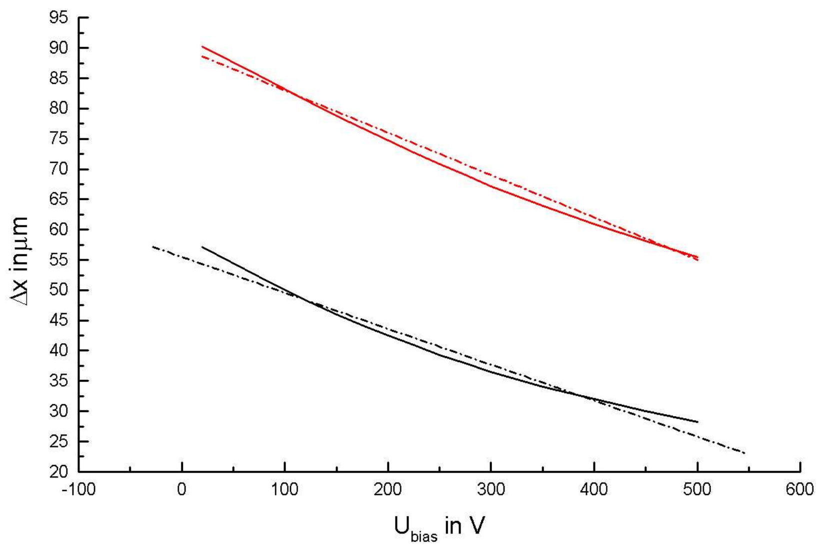

Figure 4.9: *The Lorentz shift Δx simulated for a 320 μm thick detector (lower lines) and a 500 μm thick detector (upper lines) in a 4 T magnetic field by Eq. 4.2, 4.4 and 3.3. The dashed lines represent the linear approximation.*

age, which amounts most of the time twice the depletion voltage. The expected maximal final depletion voltage for the highest fluence level reaches about 350 V [TRA98, ADD00]. The breakdown voltage is specified to be at least 500 V. It was tested that for the CMS sensors the approximation made in Eq. 4.5 is valid. Fig. 4.9 shows the simulated Lorentz shift as a function of the voltage for a 320 and 500 μm thick detector. The dependence of the Lorentz shift on the bias voltage is quite linear for fully depleted detectors. Instead of calculating the Lorentz shift from the mobility the approximate linearity between bias voltage and Lorentz shift can be used:

$$\Delta x = A - B \cdot U_{bias} \tag{4.6}$$

For a 320 μm thick detector at 263 K in a 4 T magnetic field A = 90 μm and B = 0.07 μm/V. For a 500 μm thick detector A = 55 μm and B = 0.06 μm/V.

The temperature dependence of the Lorentz shift is shown in Fig. 4.10. The Lorentz shift varies about 8 μm for a 300 μm thick sensor at 100 V in a 4 T

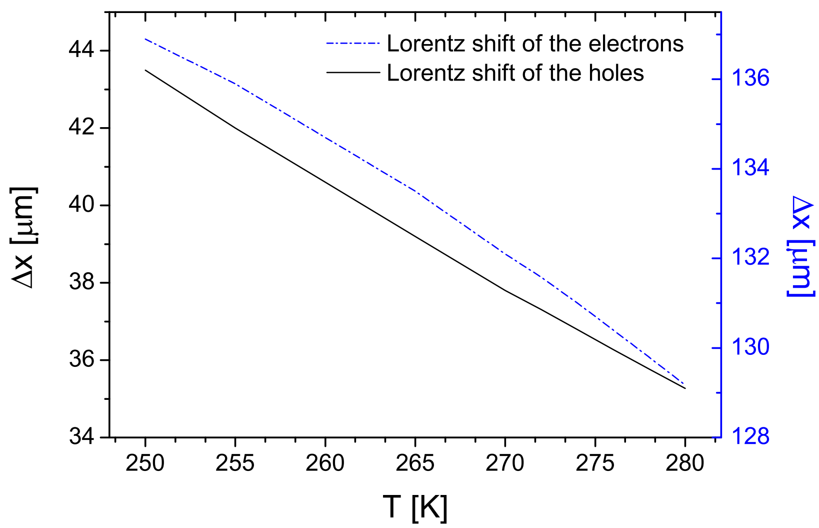

Figure 4.10: *The temperature dependence of the Lorentz shift Δx for holes (lower curve, left scale) and electrons (top curve, right scale) predicted for a 300 µm thick sensor in a 4T magnetic field at a bias voltage $U_{\rm bias}$ of 100 V.*

magnetic field, if the temperature is varied between 250 K and 280 K, for both: electrons and holes.

Irradiated sensors

As pointed out in the Chapter 3.6 there are several characteristics of a silicon detector, which changes after irradiation damage. For the algorithm the change of mobility, electric field and depletion voltage are considered. In addition, the Hall scattering factor $r_{\rm H}$ may change after irradiation. Concerning the Lorentz shift, this is equivalent to a change in drift velocity. Therefore $r_{\rm H}$, is kept constant and the data are fitted with a variable electron mobility describing the data well as shown in Tab. 4.3. The needed shift in mobility is within the range given in Ref. [L$^+$99].

Here Eq. 4.5 is used to calculate the electric field, since the depletion voltages were reasonably low. For higher depletion voltages the bias voltage is so high, that the saturation of the drift velocity has to be taken into account, which implies the use of Eq. 3.3 instead of 4.5. In this case, the depletion voltage has to be known.

In this model, the effect of double junctions after irradiation is neglected and the effect of defects ([B+98, C+99, M+99, E+02]). In general, this neglection can only be justified by the present agreement between the model and available data. In the case of the CMS silicon sensors the neglection can be justified because of the relatively low radiation damage, which the sensors have to stand, and the high bias voltage, which is about twice the depletion voltage.

Table 4.3: *The Lorentz shift Δx for electrons generated at the surface for a 300 μm thick sensor in a 4 T magnetic field at 280 K as function of bias voltage. The sensor was irradiated with 21 MeV protons up to a fluence of 10^{13} cm^2. The full depletion voltage is 100 V. Θ_{sim} with the reduced mobility fits the data Θ_{meas} better.*

U_{bias} in V	Δx in μm	Θ_{meas} in °	Θ_{sim} in degree $\mu_{\text{low}} = 1417\,\text{cm}^2/\text{Vs}$ at 300 K	Θ_{sim} in degree $\mu_{\text{low}} = 1100\,\text{cm}^2/\text{Vs}$ at 300 K
50	117 ± 7	21 ± 1	24	20
100	127 ± 7	23 ± 1	29	25
150	126 ± 7	23 ± 1	25	22

4.4 Algorithm for the Compensation of the Lorentz Angle in Silicon Pixel Detectors

Pixel detectors are located near the beam pipe and therefore have to stand higher radiation doses than the strip detectors. At distances between 4.3 cm to 11 cm from the beampipe, the resulting fluence is up to about $2{\cdot}10^{15}$ 1 MeV n/cm^2 for an integrated luminosity of $5{\cdot}10^5\,\text{pb}^{-1}$. Therefore the CMS pixel detector can not be fully depleted after some operation time. A maximum bias voltage of about 300 V is foreseen.

One can generally state some facts about pixel detectors: Since the bulk inverts after strong irradiation from n-type to p-type, the pn-junction will be on the n-side and the depletion starts from the n-side. If not fully depleted, there will

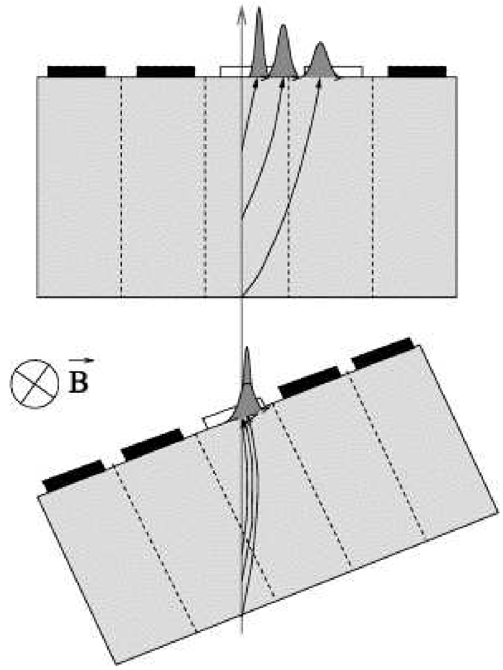

Figure 4.11: *Drift of charge carriers under the influence of a magnetic field. The upper figure shows a perpendicular particle, in the lower the incident particle crosses the sensor at the Lorentz angle. [Ale02]*

be a region without electric field, where only diffusion takes place (see Fig. 4.12) contributing significantly to the signal, so one can consider this sensor as having a sensitive thickness corresponding to the depleted zone. I assume in my description that the Lorentz shift is determined by the sensitive thickness, thus ignoring the undepleted zone. My calculation is compared with measurements for the ATLAS pixel sensor reported in Ref. [Ale00]. In this case the approach for measuring the Lorentz angle was different from the one in the Karlsruhe measurements. The charge carriers were generated with a pion beam of a momentum of 180 GeV/c. The Lorentz angle was determined by measuring the minimum mean cluster size as a function of angle of the incident beam particles as depicted in Fig. 4.11. The ATLAS pixel sensors are 280 μm thick and have a full depletion voltage before irradiation of about 150 V. The magnetic field during the measurements was 1.4 T and the temperature 300 K for the non-irradiated sensors and 263 K for the irradiated ones. The measured values are compared to the simulated ones in Tab. 4.4. To measure the depletion zone depth, data were taken with particle beam incident on the sensor at an angle of 20^0 or 30^0 with

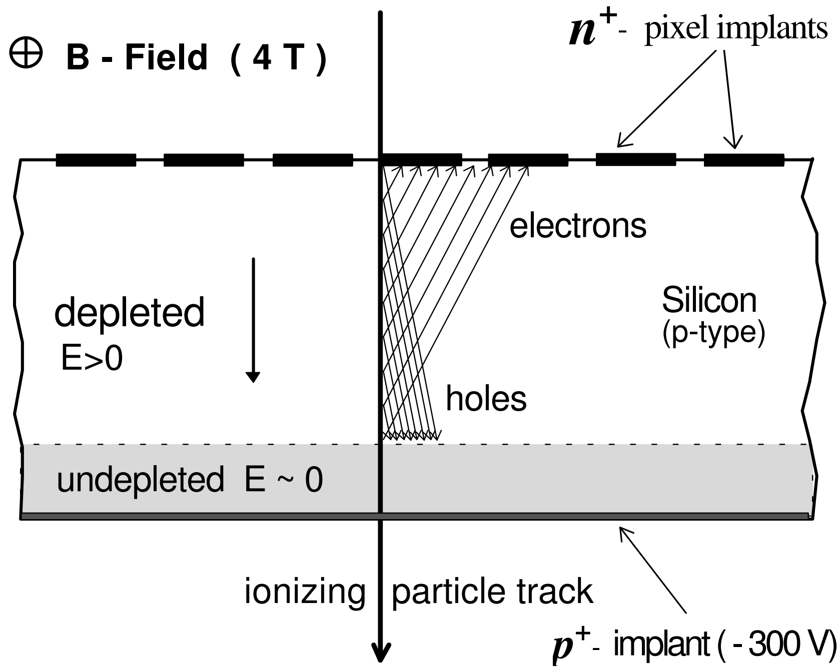

Figure 4.12: *After type inversion the sensor depletes from the n-pixel side. With increasing radiation dose, the sensor cannot be fully depleted and the total Lorentz shift is reduced. [TRA98]*

respect to the normal to the pixel plane (Fig. 4.13(a)). A particle crossing the detector produces a cluster of hits consisting of the pixel cells that collect the charges. When the sensor is not fully depleted, the cluster width may be smaller than expected by purely geometric considerations. To measure the depth of the depleted region the maximum depth of track segments was used (see Fig. 4.13(b)).

Since the electric field in the pixel sensor changes more than in the strip sensor, the mobility of the electrons varies appreciably as can be seen in Fig. 4.14. Therefore the algorithm integrates over the sensor thickness. In each part the average mobility and corresponding Lorentz shift was calculated using the standard and reduced mobilities μ_{low} of Tab. 4.3. The total Lorentz shift is then the sum of the shifts in the integration steps. Throughout the sensor the Lorentz angle varies because of the changing electric field and the changing mobility (see Eq. 4.4), so the Lorentz angle can be defined as the mean Lorentz angle, calculated by the shift and the drift distance in the detector. A comparison of the simulation with the measurements reveals that the data can be better

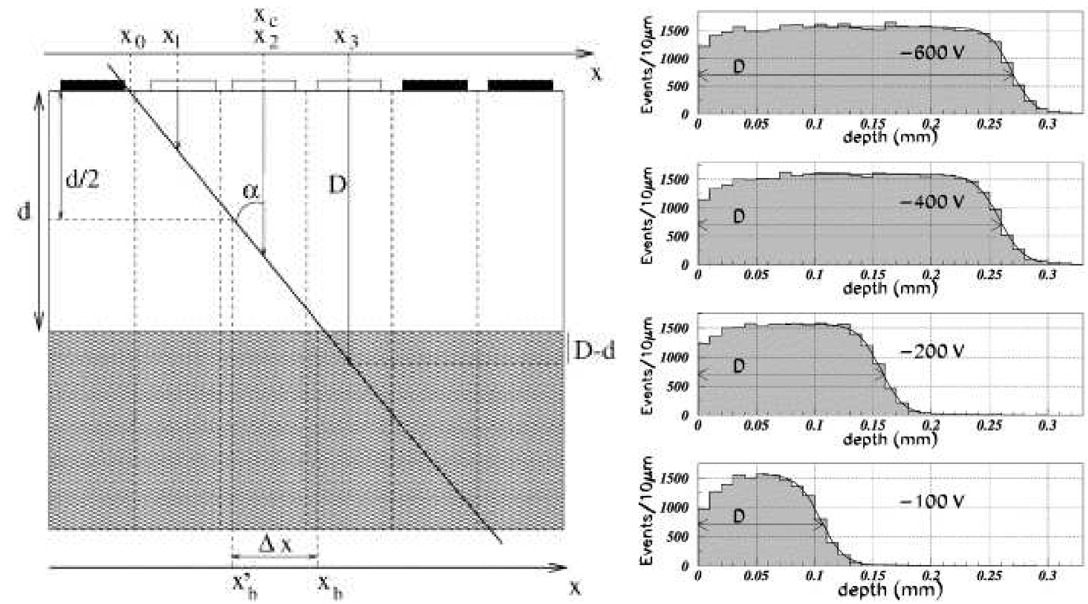

(a) (b)

Figure 4.13: *(a) schematic view of an irradiated sensor crossed by a track, the hatched zone corresponds to the not-depleted zone, (b) distribution of the track-segment depth for sensors irradiated to a fluence of $0.5{\cdot}10^{15}$ $1MeV\,n/cm^2$ for four different voltages, [Ale02]*

fitted with lower mobilities after irradiation, as expected from the discussion on mobilities in Sect. 4.3. So it was shown that the proposed algorithm also works for the pixel detectors, if the reduced sensitive thickness is taken into account.

4.5 Conclusions for the Implementation

The Lorentz angle is determined by electric and magnetic fields and can be modelled by Eqs. 4.2, 4.4 and 3.3 or 4.5. Because of the different mobility and Hall scattering factor for holes and electrons, the Lorentz shift for electrons is at least four times the one for holes. Irradiation decreases significantly the electron mobility at low electric fields μ_{low} while the hole mobility is almost unaffected by irradiation.

Fluence n/cm^2	U_{bias} in V	Depl. depth in μm	Θ_{meas} in degree	Θ_{sim} in degree $\mu_{\text{low}} = 1417\,\text{cm}^2/\text{Vs}$ at 300 K	Θ_{sim} in degree $\mu_{\text{low}} = 1100\,\text{cm}^2/\text{Vs}$ at 300 K
0	150	283 ± 6	9.0 ± 0.9	8.4	
$5{\cdot}10^{14}$	150	123 ± 19	5.9 ± 1.3	6.7	5.7
$5{\cdot}10^{14}$	600	261 ± 8	2.6 ± 0.5	4.4	3.9
10^{15}	600	189 ± 12	3.1 ± 1.0	3.8	3.5
10^{15}	600	217 ± 13	2.7 ± 0.8	3.2	3.0

Table 4.4: *The Lorentz angle for electrons for a 280 μm thick sensor in a 1.4 T magnetic field. The full depletion voltage before irradiation is 150 V. The measured data are taken from [Ale00]. The algorithm used for the simulation integrates over the sensor, in which the mean electric field and the corresponding Lorentz shift are calculated. The average Lorentz angle is defined to be the arc tangent of the total Lorentz shift divided by the depletion depth. Θ_{sim} with the reduced mobility fits the data Θ_{meas} better.*

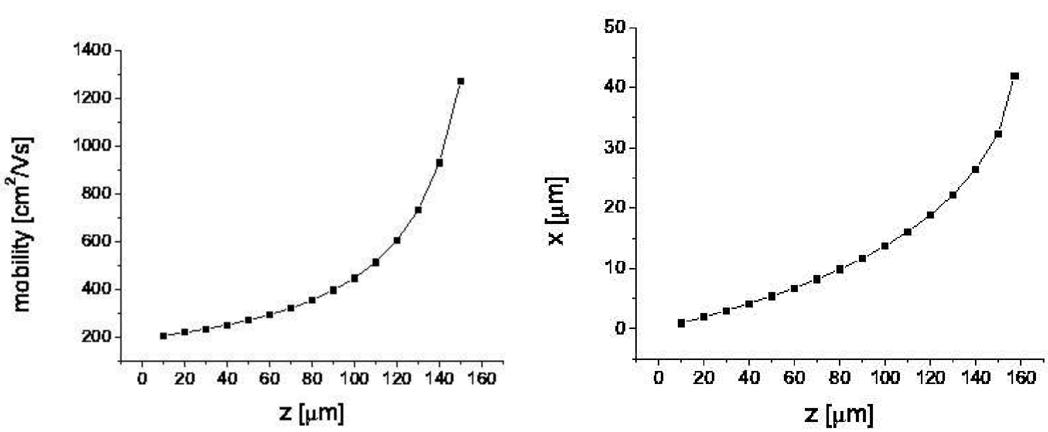

Figure 4.14: *Simulated mobility (left hand side) and mean trajectory (right hand side) of electrons at a full depletion voltage of 1100 V and a bias voltage of 300 V at 263 K change strongly in the depleted zone of the sensor.*

The simulated data are compared with measured values from HERA-B test structures and the ATLAS pixel sensor. It is shown that the algorithms developed here simulate the Lorentz shifts reasonably well, if the reduced electron mobility after irradiation is taken into account.

For the implementation of the Lorentz angle in the CMS reconstruction software the Eqs. 4.2, 4.4 and 4.5 were used. The parameters from [C$^+$75] were used. A short introduction into the implementation of the Lorentz angle into the CMS software is found at Sect. A.

Chapter 5

Higgs Particle

5.1 The Higgs Boson in the Standard Model

The Standard Model is the theory for the quantitative descriptions of all interactions of fundamental particles except for gravity effects. The non-abelian gauge symmetry of the gauge group $SU(3)_{color} \times SU(2)_{left} \times U(1)_{hypercharge}$ unifies Quantum Chromodynamics [D$^+$91] described by the SU(3) group of colour interactions of quarks and gluons and Electroweak Theory [Wei67, G$^+$70] described by the SU(2)×U(1) group of weak and electromagnetic interactions of quarks and leptons. The gauge bosons of the three interactions derive from the invariance under local gauge transformations. This is illustrated by the example of the U(1) group.

The gauge principle:
The Lagrangian for a Dirac particle in vacuum has the following form:

$$L = i\bar{\psi}\gamma^\mu \partial_\mu \psi - m\bar{\psi}\psi. \tag{5.1}$$

The local gauge invariance requires the wave-function ψ to be invariant under a local phase transformation. Such a local phase transformation depends on space and time, whereas a global phase transformation does not. In the electroweak theory such a transformation has the following form:

$$\psi' = \psi \exp(iq\chi(x)), \tag{5.2}$$

q being the electric charge. This gauge transformation will in general not leave the Lagrangian invariant. A possibility to obtain a locally gauge-invariant theory is to introduce an additional vector field A_μ, which transforms in such a way that the covariant derivative D_μ,

$$D_\mu \psi = (\partial_\mu - iqA_\mu)\psi \tag{5.3}$$

transforms as ψ. That is,

$$(\partial_\mu - iqA'_\mu) \exp iq\chi(x)\psi = \exp iq\chi(x)(\partial_\mu - iqA'_\mu)\psi \tag{5.4}$$

and it follows that

$$A'_\mu = A_\mu - \partial_\mu \chi(x). \tag{5.5}$$

The vector potential A_μ, the photon field, appears as the new gauge field, when U(1) is made into a local gauge group. The new Lagrangian

$$L = i\bar{\psi}\gamma^\mu D_\mu \psi - m\bar{\psi}\psi = \bar{\psi}(\gamma^\mu \partial_\mu - m)\psi + e\bar{\psi}\gamma^\mu \psi A_\mu \tag{5.6}$$

is, by construction, invariant under the local gauge group. So, for the electromagnetic theory with massless gauge bosons, gauge invariance holds as stated above. Because A_μ is the physical photon field, a term corresponding to the kinetical energy has to be added. This term must be invariant under Eq. 5.5 and therefore is:

$$F_{\mu\nu} = \partial_\mu A_\nu - \partial_\nu A_\mu. \tag{5.7}$$

Thus the Lagrangian of the quantum electrodynamics finally is:

$$L = \bar{\psi}(\gamma^\mu \partial_\mu - m)\psi + e\bar{\psi}\gamma^\mu \psi A_\mu - \frac{1}{4} F_{\mu\nu} F^{\mu\nu}. \tag{5.8}$$

But it is impossible to obtain gauge invariance in a theory with massive gauge bosons. An additional mass term $\frac{1}{2}M^2 A_\mu A^\mu$ would be added to the Lagrangian after a corresponding local gauge transformation and therefore the gauge invariance would be destroyed. But it is known by experiments that two gauge bosons, the $W^\pm$ boson and the Z boson, have masses of about 80 GeV and 91 GeV [H$^+$02]. An elegant way to include massive gauge bosons into the theory is the so-called spontaneous symmetry breaking.

Higgs mechanism:

The mechanism is explained for the example of the U(1) gauge group, which is one of the easiest examples. The spontaneous symmetry breaking assumes all particles being massless in the first place. Masses are generated by introducing an additional scalar field, Φ, the so-called Higgs field. As Higgs field a complex field is chosen:

$$\Phi = \frac{1}{\sqrt{2}}(\Phi_1 + i\Phi_2) \tag{5.9}$$

The corresponding Lagrangian for the Higgs field and the electromagnetic field can be used:

$$L_{Higgs} + L_{em} = \frac{1}{4}F_{\mu\nu}F^{\mu\nu} + |(\partial_\nu - ieA_\nu\Phi)|^2 + V(|\Phi^2|). \tag{5.10}$$

The choice of the potential $V(|\Phi|^2)$ is based on the requirements to have local gauge invariance and renormalizability of the interaction in the Lagrangian:

$$V(|\Phi|^2) = -\mu^2|\Phi|^2 + \lambda|\Phi|^4. \tag{5.11}$$

Fig. 5.1 shows the potential for the case that $\mu^2 > 0$ and $\lambda > 0$. The symmetrical state $\Phi = 0$ is unstable and the ground state Φ_0 is,

$$\Phi_0 = \sqrt{-\mu^2/2\lambda} = v/\sqrt{2}, \tag{5.12}$$

$v = \sqrt{-\mu^2/\lambda}$ is the absolute value of the vacuum expectation value. The vacuum expectation value still has an arbitrary phase. If one now considers excitations around the groundstate, it becomes:

$$\Phi_0 = (v + \eta(x) + i\zeta(x))/\sqrt{2}). \tag{5.13}$$

The Lagrangian of this potential looks like this:

$$\begin{aligned} L = (\frac{1}{2}(\partial_\mu\eta)(\partial^\mu\eta) - \mu^2\eta^2) + (\frac{1}{2}\partial_\mu\zeta\partial^\mu\zeta) - \frac{1}{4}F_{\mu\nu}F^{\mu\nu} + \\ \frac{1}{2}q^2v^2A_\mu A^\mu + qvA_\mu(\partial)^\mu\zeta + \mathcal{O}(\zeta^3, \eta^3). \end{aligned} \tag{5.14}$$

Terms of higher orders have been neglected. The η-field describes a particle with the mass $m_\eta = \sqrt{2}\mu$, the Higgs boson [Hig66]. The ζ-field describes a massless particle, the so-called Goldstone boson [G$^+$62]. After a local gauge transformation the Lagrangian looks like:

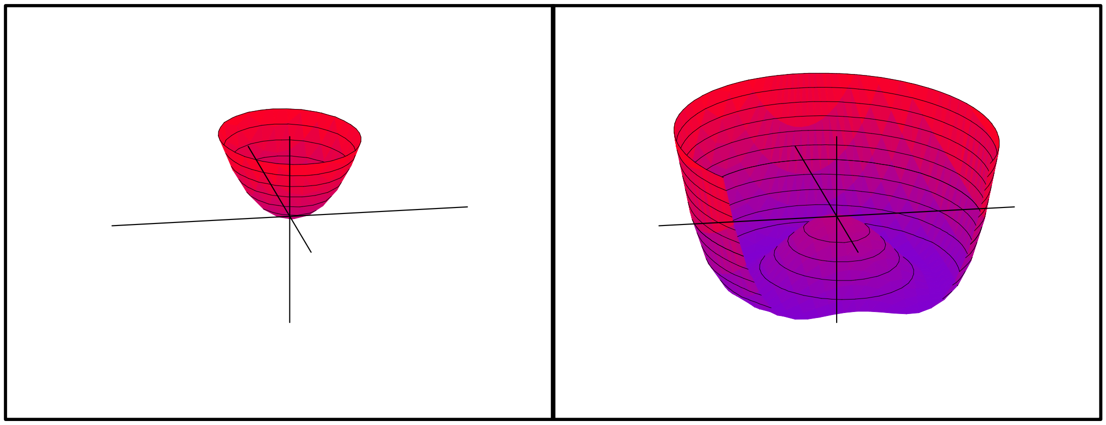

(a) (b)

Figure 5.1: *Higgs potential $V(\Phi(x))$: (a) $\mu^2 > 0$, in other words the symmetry is unbroken and only x=0 exists as a trivial minimum. (b) $\mu^2 < 0$, the symmetry is broken and nontrivial minima exist. The Higgs potential has now the well-known mexican hat shape.*

$$L = (\frac{1}{2}(\partial_\mu \eta)(\partial^\mu \eta) - \mu^2 \eta^2) + \frac{1}{4} F_{\mu\nu} F^{\mu\nu} + \frac{1}{2} q^2 v^2 A_\mu A^\mu + \mathcal{O}(\zeta^3, \eta^3). \tag{5.15}$$

The ζ-field and the term $qvA_\mu(\partial)^\mu\zeta$ vanish. But the balance of the number of degrees of freedom stays the same. Before the local gauge transformation there is one η-field, one ζ-field and two transverse degrees of freedom of the electromagnetic field. After the local gauge transformation there is one η-field, two transverse and one longitudinal degree of freedom of the electromagnetic field. In this easy example the photon field A_μ obtains a mass $\frac{1}{2}q^2v^2$ and therefore a concept giving mass to the gauge bosons is found. Of course from experiment it is known that the photons are massless, so for a realistic theory a more complicated system needs to be used: the SU(2) group with two massive gauge bosons.

Masses of the gauge bosons:

In the same manner as the mechanism described above the mass of the gauge bosons $W^\pm$ and Z can be obtained. To consider the coupling of the Higgs boson to the charged $W^\pm$ boson Higgs fields with different charges are necessary:

$$\Phi = \frac{1}{\sqrt{2}} \begin{pmatrix} \Phi_1^+ + i\Phi_2^+ \\ \Phi_1^0 + i\Phi_2^0 \end{pmatrix}. \tag{5.16}$$

The corresponding Lagrangian of the gauge fields L_{gauge} has to be added to the total Lagrangian:

$$L_{gauge} = -\frac{1}{4} F^i_{\mu\nu} F^{i\mu\nu} - \frac{1}{4} f_{\mu\nu} f^{\mu\nu} \tag{5.17}$$

with

$$F^i_{\mu\nu} = \partial_\nu W^i_\mu - \partial_\mu W^i_\nu + g\epsilon_{ijk} W^j_\mu W^k_\nu \tag{5.18}$$

$$f_{\mu\nu} = \partial_\nu B_\mu - \partial_\mu B_\nu. \tag{5.19}$$

W and B represent the field tensors of the weak and electromagnetic interactions. The covariant derivative, necessary to conserve gauge invariance, has the form:

$$D_\mu = \partial_\mu + i\frac{g'}{2} B_\mu Y + i\frac{g}{2} B^a_\mu \tau_a. \tag{5.20}$$

Here g and g' represent the coupling constant for SU(2)$_{left}$ and U(1)$_{hypercharge}$ respectively. Y is the weak hypercharge and τ are the Pauli matrices. Now the usual procedure of replacing the regular derivative in the Lagrangian by its corresponding covariant form is applied and leads to a gauge invariant form of the Lagrangian. The kinetic part assuming a weak hypercharge Y of 1 is:

$$L_{kin} = \frac{1}{4}[(gW^i_\mu \tau_i + g' B_\mu)\Phi]^2 \tag{5.21}$$

The physical fields A$_\mu$, Z$_\mu$ and W$^\pm_\mu$ are connected to W^i_μ and B_μ by the following relations:

$$A_\mu = B_\mu \cos\theta_W + W^3_\mu \sin\theta_W \tag{5.22}$$

$$Z_\mu = -B_\mu \sin\theta_W + W^3_\mu \cos\theta_W \tag{5.23}$$

$$W^\pm_\mu = \frac{1}{\sqrt{2}}(W^1_\mu \pm iW^2_\mu), \tag{5.24}$$

here θ_W is the Weinberg angle. These equations stress the close relation between the electromagnetic and the weak interaction. By expressing W^i_μ and B_μ with the physical fields A$_\mu$, Z$_\mu$ and W$^\pm_\mu$ one ends up with a Lagrangian containing the massive Higgs particle, the gauge field Lagrangian and two mass terms of W$^\pm$ and Z^0. The photon does not obtain a mass, which is in agreement with experimental observations.

Masses of the fermions:
The Lagrangian dealing with the Higgs coupling to fermions contains a free parameter, the so-called Yukawa coupling G_f which is different for every charged lepton and quark. As a result the mass terms for the fermions m_f are proportional to the Yukawa coupling and therefore to the coupling of the Higgs boson:

$$m_f = G_f \frac{v}{\sqrt{2}} \tag{5.25}$$

The coupling constant G_f is a free parameter of the theory and therefore has to be adjusted to the mass of the fermion.

Important issues:
Some issues have to be emphasised: The mass of the Higgs boson depends on μ, thus on λ and v. The gauge boson mass determines v, but λ is a free parameter. Therefore, the mass of the Higgs boson is unknown. The masses of the fermions and gauge bosons, in other words the coupling constants determine the production mechanisms and decays of the Higgs boson. The Higgs sector of the Standard Model is not understood from a fundamental point of view, although it performs technically as an effective low energy theory, without conflict or contradiction.

5.2 Predictions on the Higgs Mass

To set limits on the Higgs mass, some arguments can be made. Consistency arguments of the Standard Model give constraints on the Higgs mass. As all couplings in gauge theories the unknown quartic coupling λ evolves with the energy scale, and consistency arguments require λ to be finite and positive. If λ is large, which corresponds to a heavy Higgs boson, the requirement on remaining finite up to some large scale Λ gives an upper bound on the Higgs mass [Daw97]:

$$m_H^2 < \frac{8\pi^2\nu^2}{3\log(\frac{\Lambda}{m_H})}. \tag{5.26}$$

Λ is an energy scale at which the Standard Model is expected to be no longer valid and new physics is supposed to arise. This is an approximate relation since the effects of gauge couplings and the top quark within this model are neglected. A more sophisticated analysis, including the running of all gauge and Yukawa couplings, yield a similar bound (compare [C+95b, HR97]). For low energy scales Λ of about 10^3 GeV the allowed Higgs mass is in order of 1 TeV. For higher values of Λ the upper bound on the Higgs mass decreases to about 200 GeV. This bound is called triviality bound.

From experiment, some more bounds have been found for the Higgs boson. The negative direct search dominated by the Higgs Strahlung process $e^+e^- \rightarrow \mathrm{Z\,H}$ at the LEP2 collider (Large Electron Positron 2 collider) yields a lower bound of 114 GeV on the Standard Model Higgs mass [LEP03b]. The upper bound on the Higgs mass can be set because of quantum fluctuations of electroweak precision observables due to higher order corrections. The observables used are the masses of the heavy gauge bosons, their decay widths and the top quark mass. Unfortunately the contribution of the Higgs boson is small and only logarithmic in most cases. Therefore a mass region below 219 GeV at 95% confidence level is favoured by a Standard Model analysis of electroweak precision data [LEP03a] as is depicted in Fig. 5.2.

In extensions of the Standard Model, like the Minimal Supersymmetric Model, the upper limit on the Higgs boson mass is even lower. The Minimal Supersymmetric Model puts a limit on mass of the lightest Higgs boson, which is similar to the Standard Model Higgs boson, of 125 GeV.

5.3 Production and Decay Mechanisms at LHC

Production mechanisms:
At the LHC the Higgs boson will be produced primarily via the gluon fusion mechanism for the entire relevant Higgs mass range up to about 1 TeV within the Standard Model. The gluon fusion process proceeds primarily through a top quark triangle loop as depicted in Fig. 5.3. Next-to-leading order QCD corrections to the production cross sections of scalar as well as pseudoscalar Higgs bosons have been calculated (compare [DSZ91, Daw95, G+93, DK94, S+93]). They are significant for the theoretical prediction of the cross sections leading to an increase by up to a factor of two, compared to the lowest order results. The ratio between the leading order cross section and the next-to-leading order cross

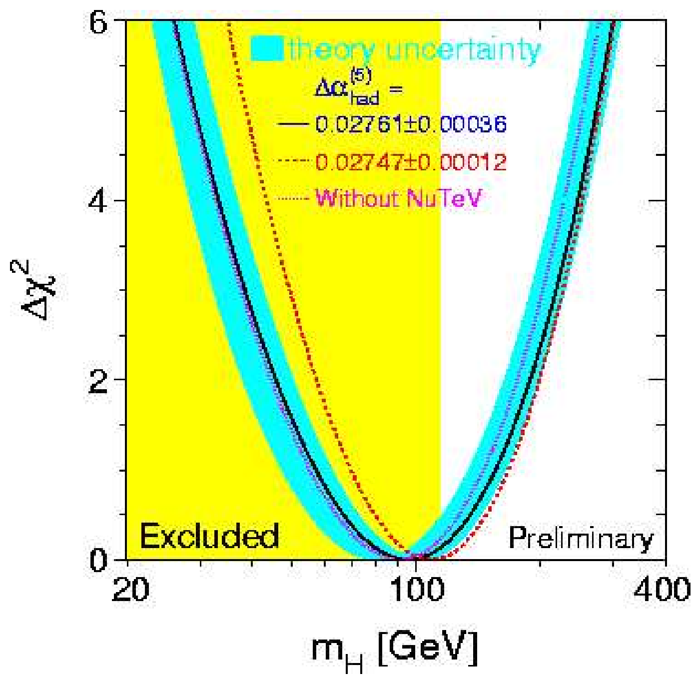

Figure 5.2: *The figure shows the $\Delta\chi^2$ curve derived from the precision electroweak measurements [LEP03a]. The preferred value for its mass, corresponding to the minimum of the curve, is about 96 GeV. The blue (dark shaded) band reaches at about 219 GeV $\Delta\chi^2 = 2.7$ and here it puts here an upper limit on the Higgs mass. The blue band considers theoretical uncertainties. The yellow (light shaded) region is the mass region excluded with 95% confidence level in the direct search at LEP.*

section is called K-factor. Very recently, the full next-to-next-to-leading order calculation, in the heavy top quark limit became available [Har00, HK02]. This limit is demonstrated to approximate the full massive K-factor at next-to-leading order within 10% in the entire mass region. Fig. 5.4 shows the resulting K-factors at the LHC and the scale variation of the K-factor. Up to now, there are no Monte Carlo generators capable of the next-to-leading order corrections of the Higgs production. So in the next chapters, the cross section available for next-to-leading order corrections (as summarised in Tab. 5.1) is considered but not the change of the observables due to next-to-leading order corrections. The gluon fusion cross section is called σ_{HIGLU} in Tab. 5.1.

The second largest contribution to the Higgs production cross section at the LHC is the weak boson fusion (see Fig. 5.5). The weak boson fusion cross section becomes comparable to the gluon fusion cross section for Higgs masses beyond

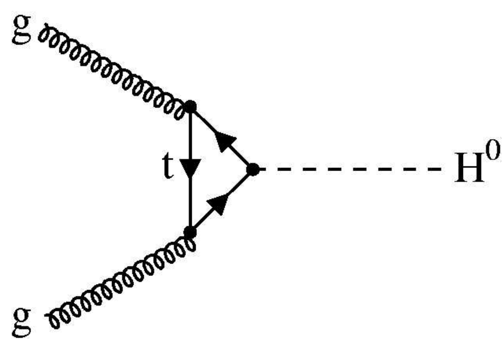

Figure 5.3: *Gluon fusion process at leading order. The Higgs boson couples to gluons mainly via the top loop.*

$\approx$600 GeV. Here the quark and anti-quark, both radiate virtual vector bosons which then annihilate to produce the Higgs boson. So beside the Higgs boson there are two quarks in the final state. These quarks can produce two highly energetic jets in forward and backward direction which can be used for the signal selection. The weak boson fusion can enhance the signal significance for low Higgs masses. There are only small theory uncertainties on the cross section, the next-to-leading order correction changes the production cross section only by about 10% [H$^+$92]. So the weak boson fusion allows a direct determination of Higgs-W coupling. The cross section for weak boson fusion σ_{VV2H} is given in Tab. 5.1.

There are two more Higgs production processes: the Higgs Strahlung and the associated Higgs production. The cross sections of these processes are usually negligible as can be seen in Tab. 5.1. The Higgs Strahlung cross section is called σ_{V2HV}, the associated Higgs production cross section is called σ_{HQQ}. The total cross section as well as the single production cross sections are depicted in Fig. 5.6 as function of the Higgs mass.

Decay mechanisms:

Depending on the Higgs mass, different Higgs decay channels can be exploited for a discovery. The Higgs coupling is proportional to the particle masses as described in Sect. 5.1. So the Higgs prefers to decay to particles as heavy as kinematically possible - particular if the decay products are on mass-shell. This can be seen in Fig. 5.7. With increasing Higgs mass, new decay channels open up

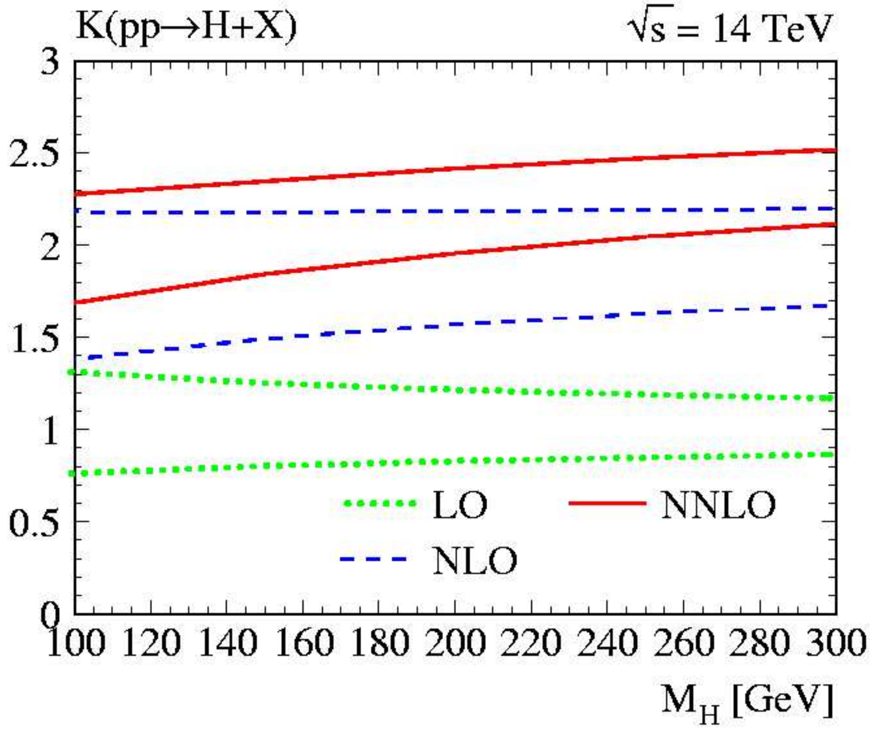

Figure 5.4: *Scale dependence of the K-factor at the LHC. Lower curves for each pair are for $\mu_R = 2m_H$, $\mu_F = m_H/2$, upper curves are for $\mu_R = m_H/2$, $\mu_F = 2m_H$. The K-factor is computed with respect to the leading order cross section at $\mu_R = \mu_F = m_H$. [HK02]*

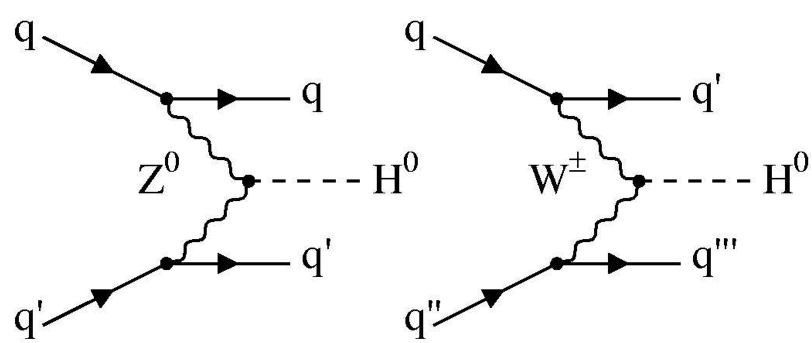

Figure 5.5: *Weak Boson Fusion at leading order. The Z fusion leaves the quark flavours unchanged. $W^{\pm}$ fusion changes the quark flavours.*

Table 5.1: *Production cross sections for different Higgs masses. The gluon fusion cross section σ_{HIGLU} is calculated by the programme HIGLU based on [Spi95], the weak boson fusion cross section σ_{VV2H} by the programme VV2H based on [H+ 92] and Higgs Strahlung cross section σ_{V2HV} by the programme V2HV based on [C+ 95a] and the associated Higgs production cross section σ_{HQQ} by the programme HQQ based on [Kun84, MP91, DW89, Spi98]. The associated Higgs production is not known at next-to-leading order.*

	leading order				next-to-leading order		
m_H GeV	σ_{HIGLU} pb	σ_{VV2H} pb	σ_{V2HV} pb	σ_{HQQ} pb	σ_{HIGLU} pb	σ_{VV2H} pb	σ_{V2HV} pb
115	15.86	5.01	1.79	0.43	35.59	4.85	2.08
120	14.80	4.84	1.57	0.38	35.73	4.68	1.82
125	13.85	4.64	1.38	0.34	33.16	4.51	1.60
130	12.99	4.47	1.22	0.30	30.90	4.33	1.41
140	11.50	4.18	0.96	0.24	27.04	4.12	1.11

and dominate the branching ratio of the Higgs. So for Higgs masses below about 130 GeV, the decays into $b\bar{b}$ pairs and $\tau^+\tau^-$ pairs dominate the branching ratio. Above that mass region the Higgs decays to off mass-shell particles get interesting. The Higgs boson begins to decay to vector boson pairs already at a mass of around 100 GeV. This means that one of the two vector bosons is off mass-shell being virtual with a different mass from the real particle. Their production cross section is smaller than the cross section for on mass-shell particles. At a mass region twice the W mass, which is equivalent to about 160 GeV the decay into W pairs peaks, whereas the decay into Z pairs is suppressed until the decay to two on mass-shell Z bosons is possible as well. At higher masses $t\bar{t}$ pairs are produced.

The importance of the decay channels for detection is not necessarily equivalent to their total cross section because the significance achievable depends heavily on the capability to experimentally detect the signal and reject the background. In addition the magnitude of the background varies for the decay channels. Figs. 5.8 and 5.9 show the significance depending on the Higgs mass for the CMS detector. The important decay channels are amongst others:

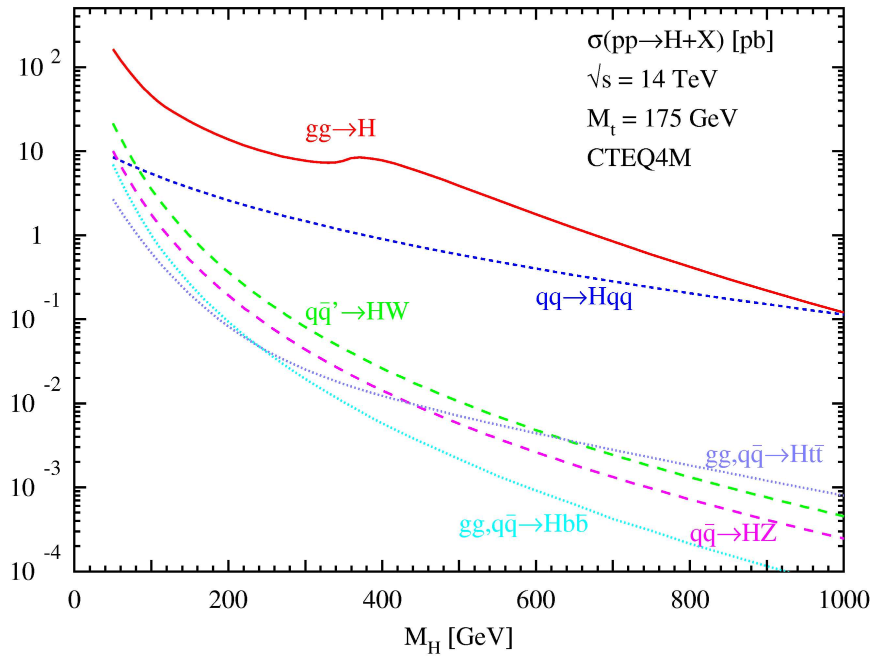

Figure 5.6: *Higgs production cross section at* $\sqrt{s}$= *14 TeV as function of the parton density function CTEQ4M.*

- h→ $\gamma\gamma$: This decay channel allows an observation of a Higgs boson over the low mass region of approximately 80 - 130 GeV. This channel has only a small branching ratio, because the H→ $\gamma\gamma$ coupling is forbidden at tree level and therefore the decay occurs only at higher order through a top quark loop. There are two main backgrounds to fight against. $\gamma\gamma$ production is an irreducible background, because it has the same final states as the signal; γ plus jet and jet-jet production with one or two jets faking a photon is a reducible background. This channel has a high significance compared to the decay h→ b$\bar{\text{b}}$, which is used for the same Higgs mass region.

- h→ b$\bar{\text{b}}$: This decay has a branching ratio close to 100% in a Higgs mass region < 130 GeV. But it is impossible to observe only b$\bar{\text{b}}$ events above the huge QCD background and even to select it at trigger level. The associated production and the Higgs Strahlung with h→ b$\bar{\text{b}}$ and with an additional lepton coming from the decay of the accompanying particles, has a much smaller cross section but gives rise to final states which can be isolated from the background.

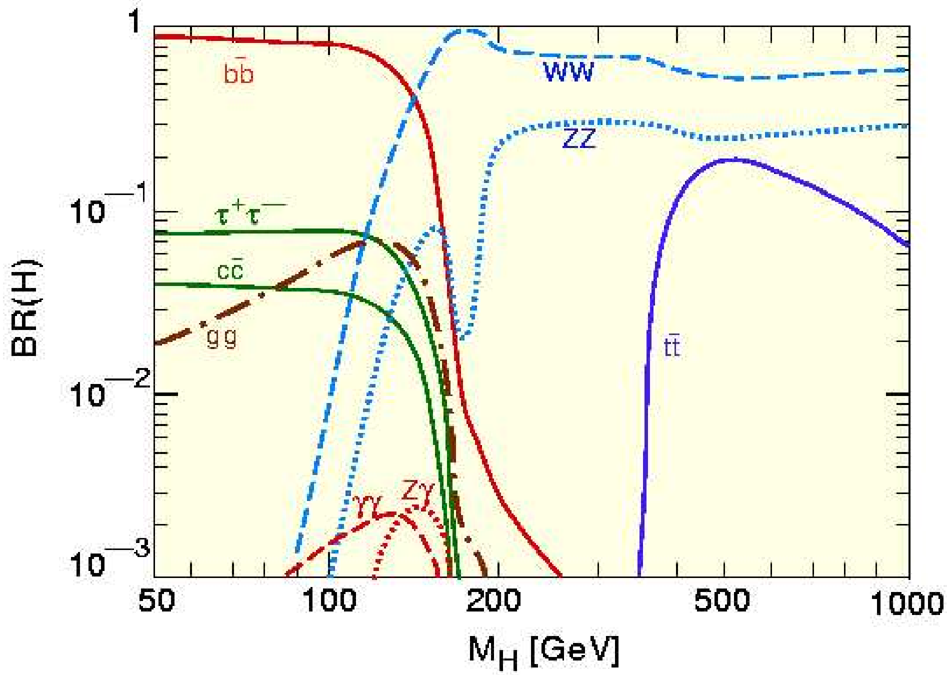

Figure 5.7: *Main branching ratios BR(H) of the Higgs decay as a function of Higgs mass in the Standard Model [DKS98]*

- h→ W^+W^-: This mode is very important for Higgs masses above W-pair but below Z-pair threshold. In order to suppress the $t\bar{t} \to b\bar{b}W^+W^-$ background a jet veto is crucial. Other main backgrounds are W^+W^- and off mass-shell $t\bar{t}$ production. In the semileptonic decays of the W bosons a neutrino occurs and therefore one gets only a very coarse prediction of the Higgs mass.

- h→ ZZ→ 4l: This channel, which can be observed at LHC over a mass region of approximately 120-700 GeV, gives rise to a very distinctive signature, consisting of four leptons. The Z boson decays into leptons with a branching ratio of about 3.4% for each lepton. Detectable are the electrons and the muons. A detailed and fully simulated study of the electron channel can be found in [Pul00] for the intermediate Higgs mass region. The muon channel is the subject of this thesis. If $m_H < 2m_Z$ the number of expected Higgs events decreases rapidly with the Higgs mass. In addition only one Z boson is real and therefore the background suppression needs to be adapted searching for one real and one off-mass shell Z boson. If $m_H > 2m_Z$, both Z

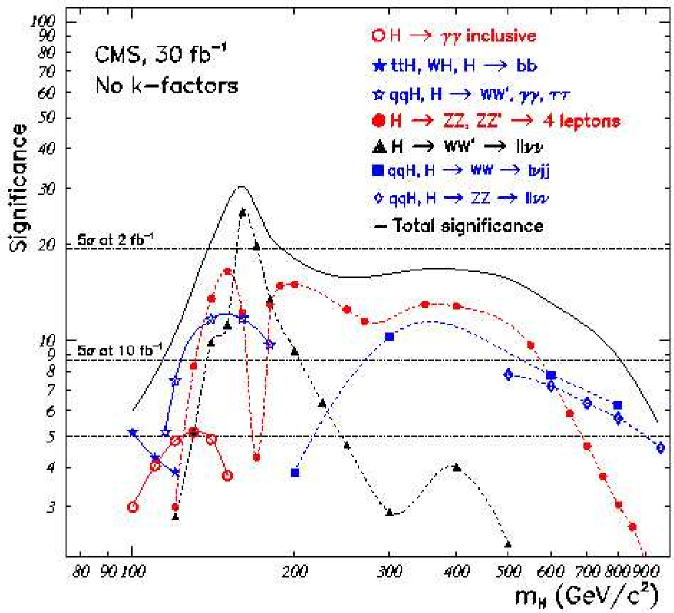

Figure 5.8: *Expected statistical significance for 30 fb^{-1} for the Standard Model Higgs boson as a function of m_H with leading order cross sections for all processes [D+03].*

bosons in the final state are real. In this region the backgrounds are small compared $m_H < 2m_Z$. The low Higgs mass case will be analysed in this thesis.

The Higgs decay width is shown in Fig. 5.10. The decay width increases with increasing Higgs mass, because new decay channels open up. A direct measurement of the decay width becomes possible at a Higgs mass > 200 GeV at LHC. At about 1 TeV the width of the Higgs is as big as its mass. So the Higgs boson looses its particle character and can not be detected but is dissolved in the background.

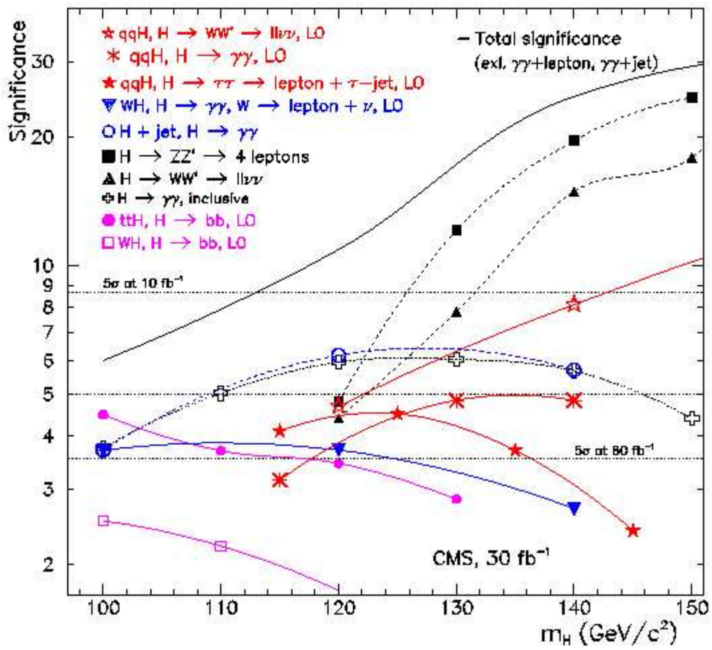

Figure 5.9: *Expected statistical significances for 30 fb^{-1} for the Standard Model Higgs Boson as a function of m_H for m_H < 150 GeV. The next-to-leading order cross sections are used for the inclusive h→ $\gamma\gamma$ and for h→ ZZ→ 4l and for h→ $W^+ W^+ \to$ ll$\nu\nu$ [D^+03].*

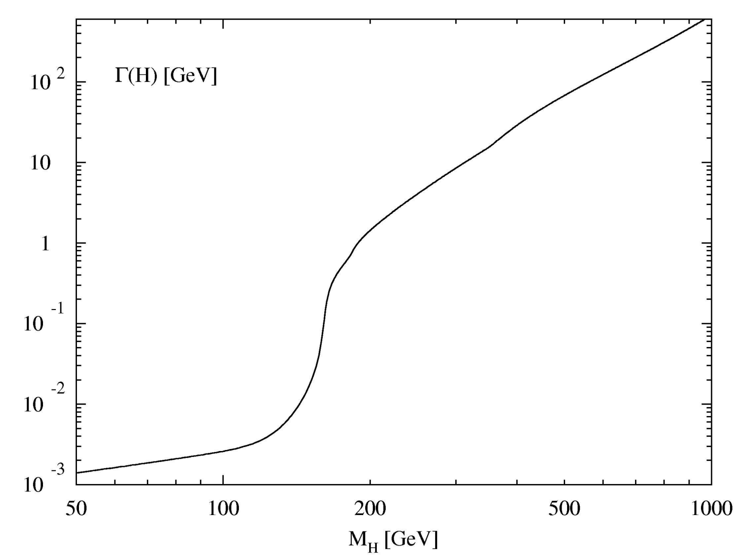

Figure 5.10: *Total decay width Γ_H of the Standard Model Higgs boson [DKS98]. For Higgs bosons lighter than 150 GeV the width is of the order of some MeV.*

Chapter 6

Simulation and Reconstruction of the Channel $\mathrm{H} \rightarrow \mathrm{ZZ}^* \rightarrow 4\,\mu$ and its Backgrounds

6.1 Overview of the Signal and Backgrounds

In this subsection the cross sections of the signal process and its main backgrounds and their main characteristics are presented. If no other citations are given, the branching ratios in this chapter are taken from the Particle Data Book [H+02].

Signal:

Many Higgs decays can be exploited to search for the Higgs boson in the mass region from 115 GeV to 140 GeV. One of the most important is $\mathrm{H} \rightarrow \mathrm{ZZ}^* \rightarrow$ 4 leptons. In this decay, the explorable final states can be divided into three classes: $4e^{\pm}$, $2e^{\pm}\,2\mu^{\pm}$ and $4\mu^{\pm}$. There is of course the possibility of the decay into τ leptons as well but this decay has not been studied in detail up to now. As subject of this thesis the channel $\mathrm{H} \rightarrow \mathrm{ZZ}^* \rightarrow 4\,\mu$ is chosen. The contribution from the decay $\mathrm{H} \rightarrow 2\,\tau 2\,\mu$ and the subsequent decay of the τ leptons into muons and neutrinos is not taken into account. The neutrinos would carry away momentum and therefore the invariant mass of all four muons would not be equal to the Higgs mass. So the small contribution of this possible decay channel would be cut away in this analysis even if considered at generator level. As shown in Fig. 6.1 the Higgs boson decays into two Z bosons, which then decay into two muons with a branching ratio of 3.4 % each. The resulting muons are easy to detect. But

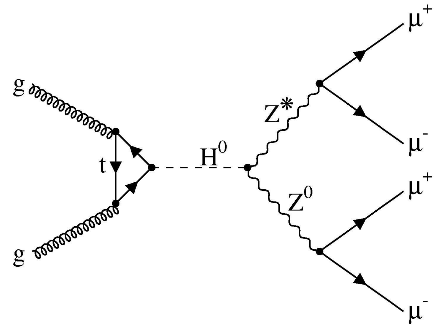

Figure 6.1: *Higgs boson produced via gluon fusion and decaying into two Z bosons. The Z bosons decay in two muons each.*

the signal cross section decreases rapidly for Higgs masses lower than twice the Z mass, because at least one Z boson has to be created off-mass shell. The partial decay width $\Gamma(H \to ZZ^*)$ for this case has the following analytical form:

$$\Gamma(H \to ZZ^*) = \delta \frac{G_F^2 m_H m_Z^4}{16\pi^3} R(\frac{m_Z^2}{m_H^2}) \tag{6.1}$$

with the constant $\delta = 7/12 - 10\sin^2\theta_W/9 + 40\sin^4\theta_W/27$. The function $\mathrm{R(x)} = \mathrm{R}(\frac{m_Z^2}{m_H^2})$ is shown in Fig. 6.2. For a Higgs mass larger than the mass of one of the gauge bosons, the decay ratio into a gauge boson pair gets important. The decay ratio reaches the level of per cents at a Higgs mass of about 110 GeV. The number of events being produced in one year of LHC operation after preselection cuts varies from 4 to 30 events for Higgs boson masses from 115 to 140 GeV. In order to avoid a further reduction the final cuts have to be chosen so that they do not reduce the signal events. Although the decay channel is considered to leave a clear signature in the detector, it has backgrounds with cross sections of about a factor hundred larger than the signal cross section even after preselection cuts (compare Tabs. 5.1 and 6.3).

Preselection cuts:

In order to produce only background events which are compatible with the signal a few preselection cuts are applied at generator level (compare to Tab. 6.2). The cut on the pseudo-rapidity η is applied to ensure that all muons are in the sensitive region of the detector. This cut has a slightly wider acceptance than will be used in the later analysis. A cut on the transverse momentum p_T

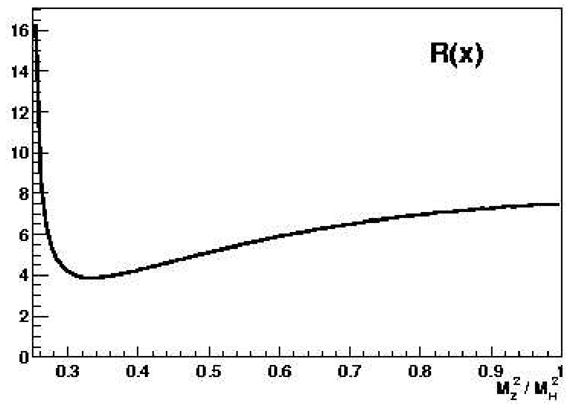

Figure 6.2: *Distribution of the function R(x) in the intervall* ($\frac{1}{4} \leq x \leq 1$) *corresponding to* ($m_Z \leq m_H \leq 2m_Z$).

Table 6.1: *Cross sections for the channel* $H \rightarrow ZZ^* \rightarrow 4\,\mu$ *at several Higgs masses. The total cross section* σ_{tot} *is given by the sum of the four main production processes for Higgs production as determined from the next-to-leading order calculations. The numbers were taken from Tab. 5.1. The branching ratio* $Br(H \rightarrow 4\,\mu)$ *is calculated by the programme HDECAY described in [DKS98], with a branching ratio* $Z \rightarrow \mu^+\mu^-$ *of 3.37%. The quoted acceptance* ϵ *is the fraction of events with four muons surviving the preselection cuts of Tab. 6.2. For the Higgs mass of 115 GeV, there were no preselection cuts applied. The number of expected events after one LHC year operating at low luminosity corresponding to an integrated luminosity of 20 fb*$^{-1}$*, is given in the last column. The statistical errors of the parameters given in the table are negligible.*

m_H GeV	σ_{tot} pb	Br(H$\rightarrow$4 μ)	ϵ	$\sigma_{tot} \cdot \epsilon \cdot$ Br fb	exp. events at 20 fb^{-1}
115	43.0	9.42 10^{-6}	1	0.22	4.4
120	42.6	1.73 10^{-5}	0.53	0.39	7.8
125	40.0	2.89 10^{-5}	0.56	0.64	12.8
130	37.3	4.35 10^{-5}	0.57	0.93	18.6
140	32.5	7.75 10^{-5}	0.60	1.51	30.3

Table 6.2: *Overview of the preselection cuts on the signal and background samples*

$\lvert\eta\rvert < 2.5$ for all muons
$p_T > 3.0\,\mathrm{GeV}$ for all muons
$10\,\mathrm{GeV} < m_{inv1} < 60\,\mathrm{GeV}$
$60\,\mathrm{GeV} < m_{inv2} < 110\,\mathrm{GeV}$
$100\,\mathrm{GeV} < m_{inv} < 150\,\mathrm{GeV}$

is applied to ensure a sufficiently good reconstruction efficiency. In each event, there must be one pair of oppositely-charged muons with an invariant mass, m_{inv1} compatible with a real Z boson; among all pairings, the one with the best agreement with a real Z is identified, and a second pair of remaining muons must have an invariant mass, m_{inv2}, consistent with a low-mass virtual Z boson. The invariant mass of all four muons m_{inv} is required to lie in the Higgs mass range.

Backgrounds:
The main backgrounds have a signature similar to the signal containing four muons in the final state. Most relevant are the $\mathrm{t\bar{t}}$, $\mathrm{Zb\bar{b}}$ and the $\mathrm{ZZ^{*}}$ background processes containing a heavy gauge boson either directly or in the decay chain[2].

- $\mathrm{t\bar{t}}$ background: The top quark decays almost exclusively into a W boson and a b quark. W bosons have a probability of 10.47 % to decay into a muon and its corresponding neutrinos. The b quark hadronises with a muon from semi-leptonic b-hadron decays occurring in about 10% of the jets.

  The $\mathrm{t\bar{t}}$ pair can be either produced via gluon fusion or quark annihilation as depicted in Fig. 6.3. The next-to-leading order cross section has been calculated and the results at the LHC centre-of-mass energy are given in [lhca]. The total cross section amounts to $\sigma_{LO} = 515 \pm 233\,\mathrm{pb}$ in leading order, while the next-to-leading-order value is $\sigma_{NLO} = 886 \pm 94\,\mathrm{pb}$. The cross section depends on the uncertainty in the choice of the renormal-

[2]Heavy gauge bosons were forced to decay directly into muons, and therefore the small additional contribution of muons from decays of quarks originating from the heavy gauge boson decay are neglected in the study presented here.

isation scales in the proton structure function and in the parton-level cross section calculations. For this study the calculation for the parton density function CTEQ5M and the scale $\mu = m_t$ was chosen. For this process, much less energy is needed than provided by the two protons. The parton distribution function of the proton shows that gluons peak at a low momentum fraction of the proton's momentum whereas the quarks peak at larger momentum fractions. So according to the parton density distribution, it is much more likely that gluons produce $\mathrm{t\bar{t}}$ pairs than quarks. The gluon fusion process has an about six times higher cross section than the quark annihilation process. The same holds for the $\mathrm{Zb\bar{b}}$ background.

The $\mathrm{t\bar{t}}$ background can be easily suppressed. Except for the identical final state, it does not show any other characteristic of the signal. There are non-isolated muons in this background, no Z boson is involved in the process and therefore the Z mass reconstruction often fails. This background however is relevant because of its large cross section.

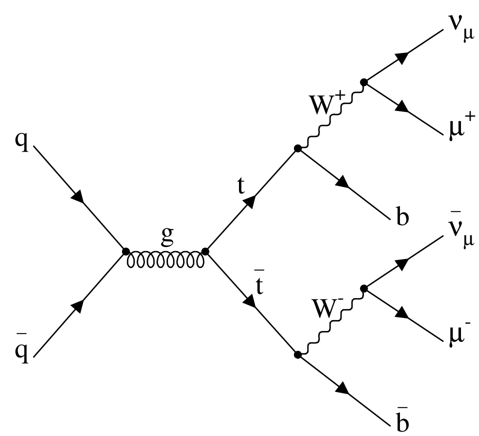

Figure 6.3: $\mathrm{t\bar{t}}$ *production. Two initial quarks or gluons produce a* $\mathrm{t\bar{t}}$ *pair.*

- $\mathrm{Zb\bar{b}}$ background: The background can be produced either from gluons or from quarks in the initial state as depicted in Fig. 6.4. The $\mathrm{gg} \rightarrow \mathrm{Zb\bar{b}}$ cross section has been calculated and in [vEK90] it is found that the cross section has an uncertainty of 50 % from the scale and structure functions choice. The total leading order calculation with the event generator COMPHEP, with both gluon and quark initial states, yields 746 pb. The structure function CTEQ5m is used. Next-to-leading order calculations done with the programme MCFM [CE03] for both gluon and quark initial states, result in a K-factor of 2 for this process. The next-to-leading order cross section thus amounts 1492 pb .

Because this process is not implemented in the event generator PYTHIA [S+01], the production is done with COMPHEP. The same structure function as for the $t\bar{t}$ background, CTEQ5m, is used. About 80 % of the events are produced from gluons in the initial state, about 20 % of the events are produced from quarks. For performance reasons this background is generated with only gluons in the initial state. A study on the transverse momentum and rapidity distribution of b quarks and the Z boson in the $Zb\bar{b}$ production is described in [Pul00]. The results are depicted in Fig. 6.5. It can be seen that the p_T distribution is similar for gluon and quark initial states, whereas the rapidity distribution differs, with the Z bosons being more centrally produced in the gluon fusion process.

This background contains a Z boson, so it is insensitive to a real Z mass cut, but it has two muons from the b quarks which are not isolated.

In addition to the $Zb\bar{b}$ production one can study any $Zq\bar{q}$ production, for example the $Zt\bar{t}$ or $Zc\bar{c}$ production. The total production cross section depends on the mass of the quark q. The production cross section for $Zt\bar{t}$ is 726 fb at leading order calculated by COMPHEP [Com] and therefore about a factor 1000 lower than the one for $Zb\bar{b}$. Compared to the $Zb\bar{b}$ background the $Zt\bar{t}$ background has a higher branching ratio into four muons. The top quark decays into W bosons and bottom quarks which then can both decay into muons. But the cross section to produce four muons after preselection cuts is only 0.29 fb and therefore negligible. A similar study on generator level for the $Zc\bar{c}$ production can be found at [SC03] and is found to be also negligible.

- ZZ^* background: For a Higgs mass lower than twice the Z boson mass instead of the ZZ background the ZZ^* background is relevant. The

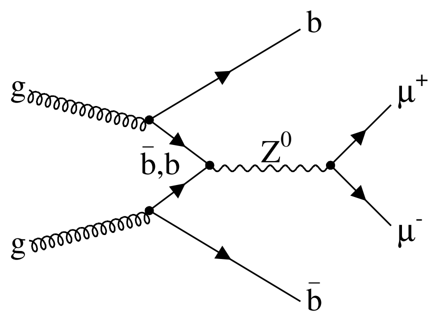

Figure 6.4: *$Zb\bar{b}$ production from gluons. The gluons split into $b\bar{b}$ pairs, two b quarks produce a Z boson, two b quarks produce jets. The Z decays into muons.*

production rate o fthe ZZ^* background, that means one Z boson being virtual, is much lower than the one for the ZZ background, that means two Z bosons being real. The ZZ^* background can be either produced from quarks in the initial state or via a loop from initial-state gluons (compare to Fig. 6.6). Only the quark initial state is implemented in the event generator PYTHIA. The next to leading order calculation of the process give a K factor of 1.33 [lhca]. The cross section of 18.2 pb given in Tab. 6.3 includes the gluon contribution and the K factor.

This background is called irreducible, because the two Z bosons decay into muons as they do for the signal events. So the only observable of this background which is different to the signal, is the Higgs mass.

A final state with four muons from ZZ^* production is also possible if one or both of the Z bosons decay to pairs of τ leptons, with a subsequent decay of each tau into a muon and two neutrinos with a probability of 17.37 %. This process amounts to 14 % of the background sample after preselection cuts. As the neutrinos from the tau decays carry away energy and momentum,

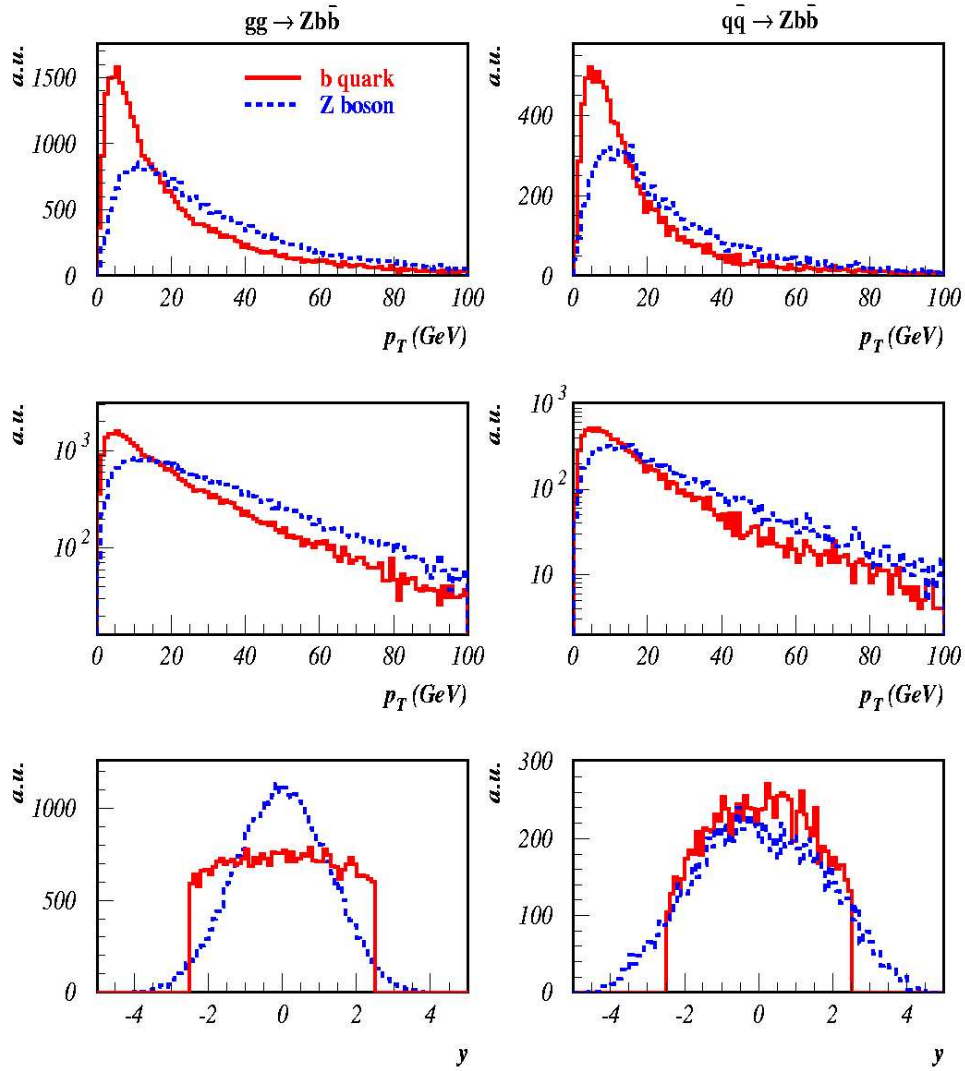

Figure 6.5: *Transverse momentum (on linear and logarithmic scales) and rapidity distributions of b quarks and Z bosons in the $Zb\bar{b}$ production for both production channels. A rapidity cut $|y_{b,\bar{b}}| = |\eta_{b,\bar{b}}| < 2.5$ is applied at generator level [Pul00].*

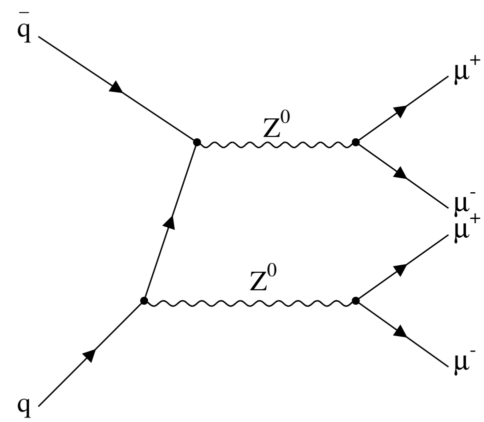

Figure 6.6: *ZZ* production: Two quarks produce two Z bosons via an intermediate quark.*

the virtual Z boson can be closer to the mass shell or even on-shell, while the muons still pass the preselection cuts on m_{inv2}. Because the ZZ* production cross section is larger for a Z* mass closer to the Z mass, the contribution of decays to muons via tau leptons is larger than naively expected from the $\tau \rightarrow \mu$ branching fraction alone.

So far, only background processes with four muons were considered. In the presence of an additional muon from other sources, *e.g.* a real muon from the other collisions in the bunch-crossing or a misidentified hadron, also processes with only three muons in the final state can contribute to the background. Since three-muon final states have a much higher rate than four-muon processes, such a background could be potentially dangerous. This background can be efficiently suppressed by requiring a common vertex for all muons. An estimate on this background is given in Sect. 7.9.

Cross sections:

In Tab. 6.3 the total cross section, the branching ratio and the acceptance after the preselection cuts, ϵ (summarised in Tab. 6.2) are shown. The expected number of events for an integrated luminosity of $20\,\text{fb}^{-1}$ is also given. Compared to the signal, the number of preselected background events is no longer enourmously high, but still the final cuts applied to the reconstructed events must reduce

Table 6.3: Cross section for the main backgrounds of the channel $\mathrm{H} \rightarrow \mathrm{ZZ}^* \rightarrow 4\,\mu$. The total cross section, σ_{prod}, are given in next-to-leading order approximation. The branching ratio, Br, for four muons in the final state is given in the second column. The quoted acceptance, ϵ, is the fraction of events with four muons surviving the preselection cuts of Tab. 6.2. The number of expected events after one year of LHC operation is given in the last column.

	σ_{prod} [pb]	$\sigma_{prod}\cdot$ Br [fb]	ϵ	$\sigma_{prod}\cdot\epsilon\cdot$ Br [fb]	expected events at 20fb^{-1}
$\mathrm{Zb\bar{b}}$	1492 (NLO)	51.2	0.24 %	122.8	2456
$\mathrm{t\bar{t}}$	886 (NLO)	8.86	0.74 %	65.5	1310
ZZ^*	18.2 (NLO)	0.084	1.37 %	1.14	23

the background by several orders of magnitude, as is described in the following sections.

6.2 Event Generation

This chapter describes the software used to generate Monte Carlo events, the simulation of the passage of particles through - and their interactions with - the CMS detector, and the simulation of the response of the detector elements. It also describes the first steps in the reconstruction of the particle tracks. The experiment specific software used in this section is more thoroughly described in Appendix B.

Monte Carlo Event Generation:
Standard Monte Carlo generators, such as PYTHIA (see [S$^+$01]) and COMPHEP (see [Com]), are used to simulate the collisions between two protons at a centre of mass energy of 14 TeV. They are the first step in the production chain as depicted in Fig. 6.7. The events produced are stored in the standard HEPEVT structure in HBOOK [hbo] ntuples with an average event size of about 24 kB depending on the information stored. These ntuples can already be read by ORCA and the main variables can be extracted into a ROOT tree [roo]. So already at this stage one can select the part of the background events which are

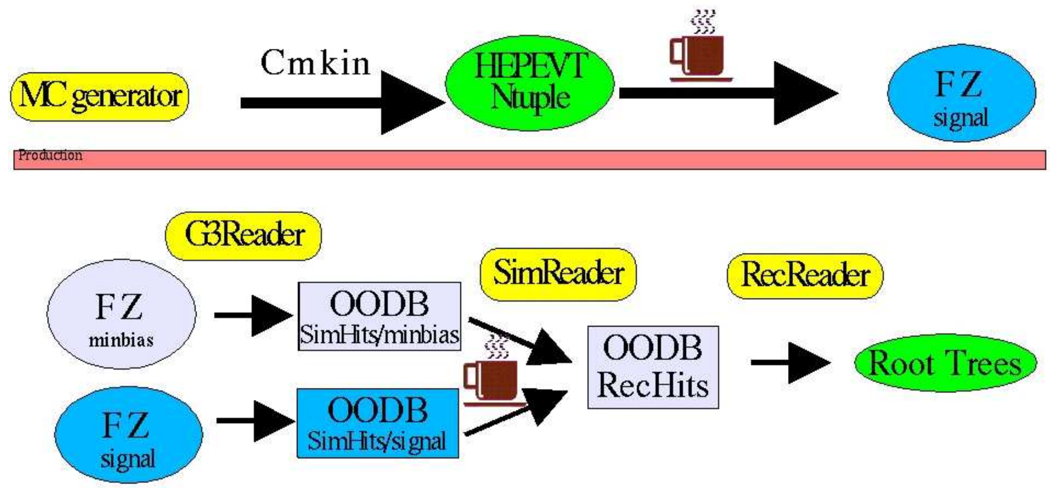

Figure 6.7: *The production chain for the full simulation at CMS. The events are produced by a Monte Carlo generator (in this case either PYTHIA or COMPHEP), then the simulated hits computed by CMSIM and finally the underlying event structure is created with the help of the full reconstruction software ORCA. The data is read out as ROOT trees.*

compatible with the signal properties.

The PYTHIA interface to the user, the interface to the Monte Carlo generator and the input/output software is steered by the CMKIN program. CMKIN also sets the LHC specific parameters. In the following the differences between the datacards used for the data sample production in this analysis and the official production datacards are described. The initial particles of the $\mathrm{Zb\bar{b}}$ background, namely the Z boson and the two b quarks, were produced with COMPHEP and the fragmentation was done by PYTHIA [3]. Most notably, the options used are *MSTJ 11=3* (choice of fragmentation function), *MSTP 51=4* (choice of structure function), *MSTP 81=1* (multiple parton interactions) and *MSTP 82=4* (definition of multi-parton model). They were set identically in all cases with the exception of $\mathrm{Zb\bar{b}}$, where *MSTP 82=4* was not switched on. An overview is given in Tab. 6.4.

Detector Description and Simulation (CMSIM)

The results of the CMSIM simulations are stored in GEANT3/CMSIM data structures in the form of ZEBRA banks. The information stored in the ZEBRA

[3]The interface between COMPHEP and PYTHIA was provided by Alexander Sherstnev.

Table 6.4: *Differences between the PYTHIA datacards used in this analysis and the official production datacards.*

Channel	Difference to official datacard
signal	none
$ZZ^{*} \rightarrow 4\,\mu$	decay in τ leptons enabled
$t\bar{t}^{*} \rightarrow 4\,\mu$	none
$Zb\bar{b}^{*} \rightarrow 4\,\mu$	*MSTP 82=4* not switched on, no cuts on COMPHEP level

files is imported into ORCA and stored in the Objectivity/DB databases. The average storage size of a single event of the ZEBRA banks is about 0.6 MB. The CPU time required to simulate one event with CMSIM on the university cluster amounts 71 s on average for a four muon event. It is therefore the most timeconsuming step in the production chain. The CMSIM step can be distributed on several computers and the cluster of the Forschungzentrum at Karlsruhe (FZK) has been used. The translation of the simulated hits into an Objectivity/DB database takes about 3 s and an average event size amounts 0.4 MB.

Simulation of Detector Response (Digitisation)

After combining a signal event with the selected pile-up events for a particular luminosity, the detector response (digitisation) is simulated taking into account the simulated hits of all events of a crossing (see Fig. 6.7). For hits of pile-up from another bunch crossing the time information is taken into account.

For the simulation the minimum bias or pile-up events are distinguished from hard scattering events that trigger the detector readout. In the low luminosity phase with $2{\cdot}10^{33}\,\mathrm{cm}^{-2} \cdot s^{-1}$ about 3.46 pile-up events contribute to each bunch crossing on average, in the high luminosity phase with $10^{34}\mathrm{cm}^{2}/\mathrm{s}$ about 17.5. The number of bunch crossings to be piled up is determined by the subdetector with the slowest response time. The values are -5 and +3, in other words five bunch crossings preceding the trigger bunch crossing and three following it. The slowest detection time in the whole CMS detector have the drift tubes of the muon

Table 6.5: *Number of fully simulated events after the preselection cuts summarised in Tab. 6.2.*

channel	no. of simulated events (low luminosity phase)	no. of simulated events (high luminosity phase)
signal: m_H=115 GeV	9.500	9.250
signal: m_H=120 GeV	9.500	9.500
signal: m_H=125 GeV	9.500	9.500
signal: m_H=130 GeV	10.000	10.000
signal: m_H=140 GeV	10.000	10.000
$\mathrm{Zb\bar{b}}$	41.000	29.000
$\mathrm{t\bar{t}}$	19.000	19.000
$\mathrm{ZZ^*}$	10.000	10.000

chambers. Their drift times are distributed up to 350 ns. The CMS detector will integrate over pile-up events produced before and after the signal event. In total up to about 160 pile-up events need to be overlaid with a single signal event to properly simulate the detector response at high luminosity. For each crossing, an individual signal event is combined with a random set of minimum bias events taken from a pool of mimimum bias events. The size of the pool of pile-up events is chosen to be large enough to ensure a unique combination for each crossing. The pile-up events used for the production were taken from the official spring production in the year 2002 [Lef02]. One needs 12 s seconds on an Athlon T-bird 1.300 MHz to produce one low luminosity event with a size of about 0.9 MB. For the high luminosity case a memory of 800-900 MB was needed. In total over 100.000 events were fully simulated (compare to Tab. 6.5).

6.3 Muon Reconstruction

Reconstruction programs may be run either as online event filter, where the prime purpose is the extraction of a few key physics features allowing the event to be accepted or rejected, or as offline tools to make further processing and physics analysis possible. These two different applications are described below for the CMS muon reconstruction.

Online event selection:

The CMS muon online trigger chain consists of a First Level Trigger, implemented on dedicated programmable hardware, and of a software High Level Trigger (HLT) system. While the Level-1 Trigger can only access data from hardware components and muon detectors with limited granularity, the fine granularity data from all CMS subdetectors can be accessed and analysed at the HLT stage.

The Level-1 Global Muon Trigger combines the trigger information from three different detector components, the drift tube, the cathode strip chamber and the resistive plate chamber, and determines the four best muon candidates in the entire CMS detector. To be accepted, an event has to exceed the Level-1 Single-Muon Trigger p_T thresholds (one muon with $p_T > 14\,\mathrm{GeV}$ for low luminosity, $p_T > 20\,\mathrm{GeV}$ for high luminosity) or the Level-1 Di-Muon Trigger thresholds (two muons with $p_T > 3\,\mathrm{GeV}$ for low luminosity, $p_T > 5\,\mathrm{GeV}$ for high luminosity). The geometrical acceptance of the Level-1-Trigger is limited to the pseudo-rapidity range $|\eta| < 2.1$, and the efficiency to find a single muon depends on $|\eta|$ and p_T. For the Z$\rightarrow \mu\mu$ channel the efficiency to find a single muon has turned out to be close to 99.0% for low luminosity and about 97.0% for high luminosity. For details see Ref. [Neu]. The muon HLT is further divided into two selection steps:

The Level-2 Trigger takes a decision based on data from muon detectors and calorimeters. In the first step, track segments in the drift tubes and cathods strip chambers are reconstructed by clustering hits in the regions of interest defined by the Level-1 muon trigger. Then the reconstructed tracks segments are combined using a Kalman-Filter algorithm in order to reconstruct a local muon trajectory. Bad measurements are rejected by applying a χ^2 cut. After that, tracks are projected through the calorimeters to the nominal vertex position in order to assign a p_T value at the interaction point. The projection/refit procedure is repeated for the next drift tube or cathode strip chamber, until the outermost layer of the muon detector is reached. The Level-3 Trigger starts from a muon reconstructed at Level-2, the muon trajectory is extrapolated from the innermost muon station to the tracker, taking into account the muon energy losses in the material and multiple scattering. Then the algorithm defines a region of interest to start regional track reconstruction. Tracks are reconstructed starting from seeds generated by the regional seed generator. Then, to resolve ambiguities, all reconstructed tracks are refitted including the reconstructed hits in the muon chambers from the original Level-2 muon. Finally, good tracks are selected on the basis of a χ^2 cut. To be accepted here, an event has to satisfy the HLT muon selection, which is divided in a Single-muon HLT Selection and a Di-muon HLT Selection. For the Single-muon HLT Selection, a Level-2 muon candidate must satify higher p_T thresholds (one muon with $p_T > 19$ GeV for low luminosity, $p_T > 38$ GeV for high luminosity) and a calorimeter isolation criteria, while a Level-3 candidate must satisfy the tracker and pixel isolation criteria. The selection criteria for each muon in the di-muon-trigger are the same as for those for the single muon-trigger, except that the isolation criteria need only be satisfied by one of the two muons. In addition, at Level-3, both muons are required to have originated from the same vertex in z to within 5mm whereas di-muons that have $\Delta\phi < 0.05, |\Delta\eta| < 0.01$ and $\Delta p_T < 0.1$ GeV are rejected in order to remove ghost tracks. The p_T thresholds here are one symmetric di-muon threshold of $p_T > 7$ GeV for low luminosity and a symmetric di-muon threshold of $p_T > 12$ GeV for high luminosity. A detailed description can be found in [HLT03].

In order to demonstrate sufficient Level-1-Trigger efficiency for the channel investigated in this thesis, the acceptance of the Level-1-Trigger on the signal sample for $m_H = 130$ GeV was investigated. It turned out that the Level-1 Single-Muon Trigger (one muon with $p_T > 14$ GeV, $|\eta| < 2.1$, quality flag > 1) accepts 99.7%, and the Level-1 Di-Muon Trigger (two muons with $p_T > 3$ GeV, $|\eta| < 2.1$, quality flag > 1) 99.9% of the finally reconstructed signal events. In this thesis the HLT selection efficiencies were not studied.

Offline muon reconstruction:

The available offline reconstruction consists of the *GlobalMuonReconstructor*, which performs its own seed generation using information from muon detectors and the tracker independently of the Level-1 Trigger. Therefore the offline muon reconstructor works in an $|\eta|$ region up to 2.4, while the Level-1 Trigger in CMS is only sensitive in the range $|\eta| < 2.1$. Once the seeds are found, the algorithms to reconstruct a muon trajectory are the same as used for Level-2. In the next step, the *L3MuonReconstructor* is used.

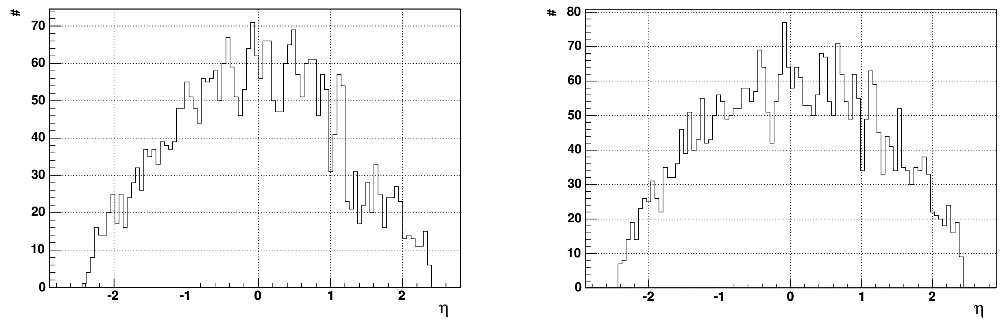

Figure 6.8: *(a) Number of reconstructed muons by the GlobalMuonReconstructor. (b) Number of reconstructed muons by the L3MuonReconstructor. The number of muons reconstructed by the L3MuonReconstructor is* 12.0% *higher than the number of muons found by the GlobalMuonReconstructor, mostly due to an inefficiency in the region* $1 < \eta < 2.0$.

A comparison of the *GlobalMuonReconstructor* and the default HLT online event selection chain showed that the HLT reconstructs significantly more muons, Fig. 6.8 demonstrates this. As a consequence, in this analysis the HLT online reconstruction is used. To achieve better performance, the Level-1 Trigger sensitivity region was widened to $|\eta| < 2.4$ by setting a special option in the reconstruction program [4], whereas for all other parameters default values of the online event selection were used. This proceeding is legitimate, since the *GlobalMuonReconstructor* is designed to also cover this $|\eta|$ region. Consequently, the results shown in this note represent a lower limit of the performance ultimately achievable with an optimised offline reconstructor.

Reconstruction Efficiency:

In the production of the data samples a pseudo-rapidity range of $|\eta| <2.5$ was chosen, which is slightly larger than the actual coverage by the muon system reaching only up to $|\eta| <2.4$. The $|\eta|$ distributions of individual muons from the signal are shown in Fig. 6.9. About 5 % of the signal events have muons within an $|\eta|$ range of 2.4 to 2.5.

[4] The option is *CSCtrigger:TwentyDegreeSubSectors=1* in the *.orcarc* steering file.

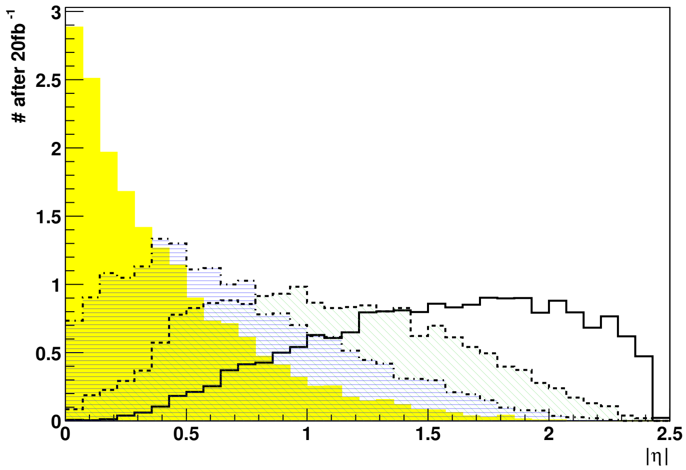

Figure 6.9: $|\eta|$ *distribution of individual muons from the signal data sample with* $m_H = 130\,GeV$*, at low luminosity. The reconstructed muons are sorted by increasing* $|\eta|$*.*

Table 6.6: *Efficiency of the muon reconstruction after preselection cuts as summarised in Tab. 6.2 and in an* η *range of 2.4 for low luminosity.*

channel	$4\ \mu$ reco efficiency at low luminosity
$\mathrm{H} \to \mathrm{ZZ}^* \to 4\,\mu$: $m_H = 115\,\mathrm{GeV}$	68 %
$\mathrm{H} \to \mathrm{ZZ}^* \to 4\,\mu$: $m_H = 120\,\mathrm{GeV}$	71 %
$\mathrm{H} \to \mathrm{ZZ}^* \to 4\,\mu$: $m_H = 125\,\mathrm{GeV}$	73 %
$\mathrm{H} \to \mathrm{ZZ}^* \to 4\,\mu$: $m_H = 130\,\mathrm{GeV}$	75 %
$\mathrm{H} \to \mathrm{ZZ}^* \to 4\,\mu$: $m_H = 140\,\mathrm{GeV}$	77 %
$\mathrm{ZZ}^* \to 4\,\mu$	67 %
$\mathrm{t\bar{t}} \to 4\,\mu$	61 %
$\mathrm{Zb\bar{b}} \to 4\,\mu$	48 %

Tab. 6.6 shows the efficiency to reconstruct all four muons for the $\mathrm{H}\to\mathrm{ZZ}^* \to 4\mu$ channel and for the main backgrounds for the low luminosity case. The reconstruction efficiency is defined as the number of events with four reconstructed muons divided by the number of simulated events surviving the preselection cuts of Tab. 6.2 with the additional requirement that all four muons are inside the η range of $|\eta| < 2.4$. It is worth mentioning that the value of p_T of the muons with

the lowest p_T is often quite small (compare Figs. 7.4 and 7.5), and therefore the muon with the lowest p_T limits the total efficiency. In Ref. [B$^+$02] for a single muon, a higher Level-3 efficiency of 97% is specified for transverse momenta of the muons higher than 10 GeV and $|\eta| < 2.1$. With the same cuts on my data sample I observed an efficiency of 95 % for a single muon, a number which largely confirms the earlier study.

Resolution:

To study the resolution achieved for various reconstructed quantities a matching between the reconstructed muons and the generated muons has to be performed. The matching procedure adopted here is simply based on the geometrical angles θ and ϕ of the muon track at the primary vertex, combining the two in a χ^2-like quantity given by

$$\chi^2 = \frac{(\phi_{rec} - \phi_{gen})^2}{\sigma_\phi^2} + \frac{(\theta_{rec} - \theta_{gen})^2}{\sigma_\theta^2} = \frac{(\Delta_\phi)^2}{\sigma_\phi^2} + \frac{(\Delta_\theta)^2}{\sigma_\theta^2}, \tag{6.2}$$

where ϕ_{rec}, θ_{rec} are the angles of the reconstructed muons and ϕ_{gen}, θ_{gen} the angles of the generated muons. Because the distributions of $\Delta\phi$ and $\Delta\theta$ are not Gaussian as depicted in Fig. 6.10, the function defined above is not a χ^2 but only a χ^2-like function. σ_ϕ and σ_θ are the standard deviations of the distributions, in both cases they result in 0.4 mrad. As shown in Fig. 6.12 σ_ϕ and σ_θ show only small variations over the whole θ range, corresponding to the *r.m.s.* of the distributions. Fig. 6.11 shows the χ^2 distribution. A reconstructed muon is considered as matching a generated one if χ^2 is less than 14; the tail beyond the cut corresponds to an integrated total of only 2% of the muons.

The $\frac{\Delta p_T}{p_T}$ resolution after the Level-3 reconstruction is shown in Fig. 6.13(a). Its standard deviation is 0.014 GeV. The p_T resolution changes slightly with transverse momentum as shown in Fig. 6.13(b). The points show the central value of the resolution in each bin of p_T, the dash-dotted error bars indicate the *r.m.s.*. The fat error bars show the statistical errors on the mean, in other words the *r.m.s.* value divided by the square root of the number of bin entries. Variations of the resolution in p_T are compatible with the statistical error on the mean. The p_T resolution is between 1 % and 2 % throughout the whole range. The tracker technical design report [TRA98] specifies the momentum resolution to be δp/p $\approx$ 1.2% with p_T in the central region gradually degrading in the outer

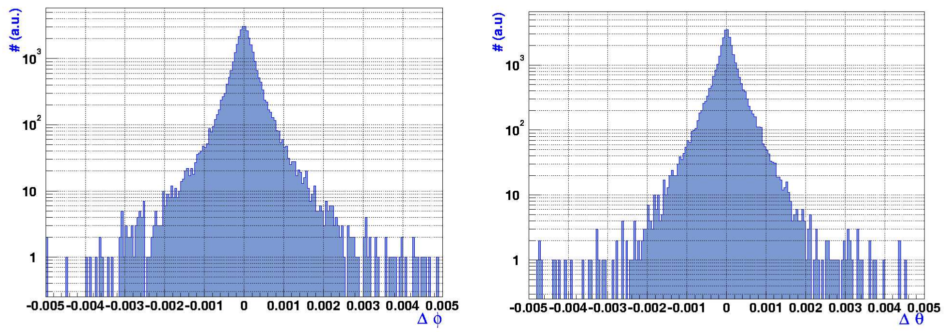

(a) (b)

Figure 6.10: *(a) $\Delta\phi$ distribution, (b) $\Delta\theta$ distribution on the right hand side. The standard deviation of both distributions is equal to $4 \cdot 10^{-4}$. All values in rad. The low luminosity scenario and the Higgs data sample with $m_H = 130\,GeV$ were studied.*

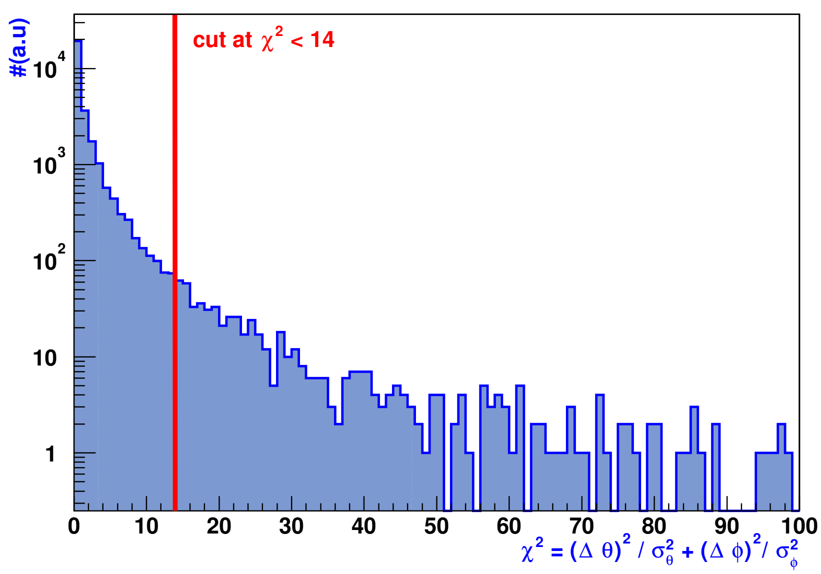

Figure 6.11: *Distribution of the matching criterion, χ^2, used to assign a reconstructed muon to a generated one. It is possible to match 98% of the muons within a χ^2 of 14. The low luminosity scenario and the Higgs data sample with $m_H = 130\,GeV$ were studied.*

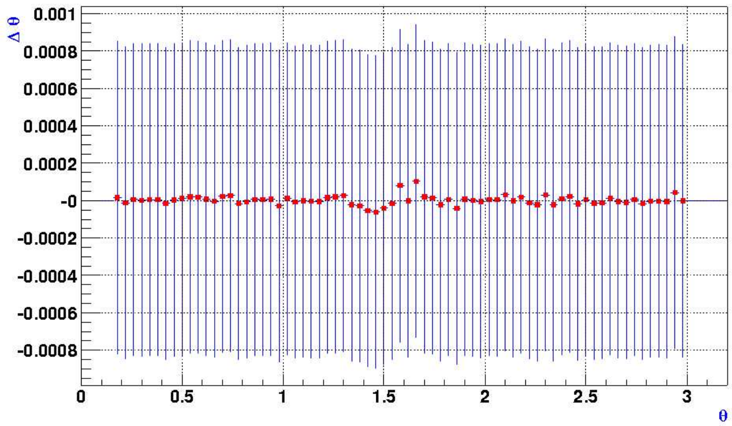

Figure 6.12: *$\Delta\theta$ versus θ distribution. Both values are given in rad. The error bars represent the standard deviation of the values. The distribution is flat.*

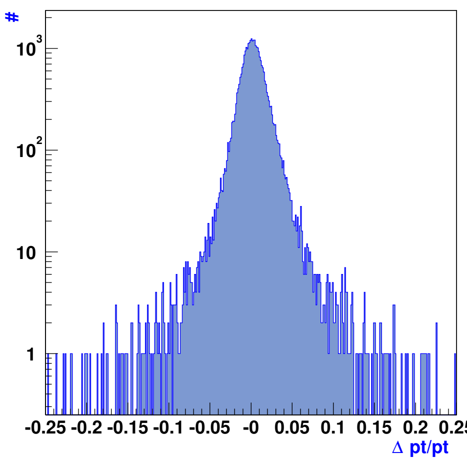

(a)

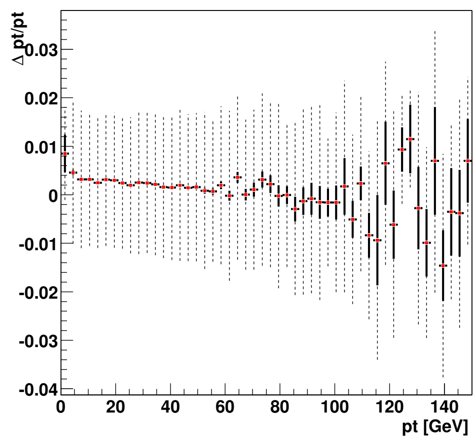

(b)

Figure 6.13: *(a) Distribution of the relative resolution of the reconstructed transverse momentum, $\frac{\Delta p_T}{p_T} = \frac{(p_{T,gen} - p_{T,rec})}{p_{T,gen}}$. The standard deviation of the distribution is 0.014. (b) $\frac{\Delta p_T}{p_T}$ versus p_T. The dash-dotted error bars are the* r.m.s. *of the distribution, the fat error bars are the statistical errors on the mean. The resolution is 1.5 - 2 % throughout the whole p_T range.*
These results were obtained for low luminosity and $m_H = 130\,GeV$.

regions. In combination with the muon system, above approximately 100 GeV the muon resolution gets worse ($\delta p/p \approx 4.5\%$). To compare these values with Fig. 6.13(b) one has to notice that the muons used for this figure are in a higher η region. Therefore the relative error is a bit higher than the one given in the Technical Design Report.

The distributions of the invariant masses of the two pairs of muons forming the Z and the Z* bosons and of all four muons, corresponding to the mass of the Higgs candidate, are shown in Fig. 6.14. The standard deviation is 0.3 GeV for the virtual Z boson mass and 0.9 GeV for the real Z boson mass. The four-muon mass distribution has a σ of 1.2 GeV, corresponding to the fitted width of the reconstructed Higgs boson after all cuts (compare to Sect. 7.6).

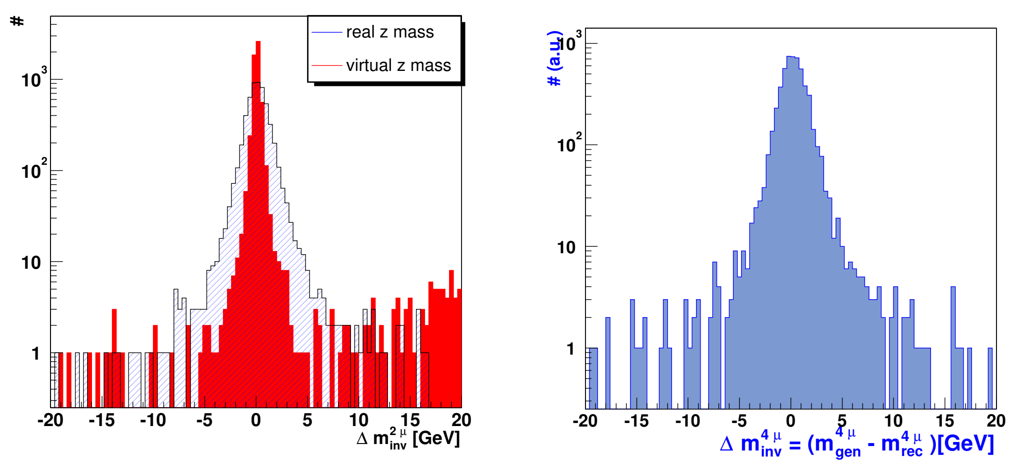

(a) (b)

Figure 6.14: *(a) Resolution of the reconstructed real and virtual Z boson masses, $\Delta m_{inv} = m^{2\mu}_{inv,gen} - m^{2\mu}_{inv,rec}$. The values of σ from Gaussian fits to the distributions are 0.3 GeV for the virtual Z mass and 0.9 GeV for the real Z mass.*
(b) Resolution of the reconstructed four-muon mass, $\Delta m^{4\mu}_{inv} = m^{4\mu}_{inv,gen} - m^{4\mu}_{inv,rec}$. A Gaussian fit gives a σ of 1.2 GeV.
For both cases the low luminosity scenario and the Higgs data sample with $m_H = 130$ GeV were studied.

Chapter 7

Selection of the Signal $\mathrm{H} \rightarrow \mathrm{ZZ}^*$ $\rightarrow 4\,\mu$ in the Mass Range of 115 GeV to 140 GeV

7.1 Kinematical Cuts applied on the Signal and the Backgrounds

This section describes the selection cuts applied at the level of the reconstructed quantities. The cuts are adapted to the search for each specific value of the Higgs mass in order to maximise the signal significance. For the high luminosity scenario almost the same cuts are applied, as will be discussed in Sect. 7.7.

To begin with, all events considered in the following must have four reconstructed muons. The cuts described below are then applied in the same order as mentioned.

Kinematical cuts on the Z boson masses:

The invariant mass of two unlike-sign muons is required to be equal to the Z boson mass. The pairing giving an invariant mass closest to the real Z boson mass is taken as the Z boson candidate. The other combination is the candidate for the virtual Z boson. The distributions of the invariant masses of the Z bosons are depicted in Fig. 7.1. Fig. 7.1(a) shows the real Z boson mass and Fig. 7.1(b) the virtual Z boson mass for various Higgs masses. Due to the decreasing cross sections, the number of events after $20\,\mathrm{fb}^{-1}$ decreases for lower Higgs masses.

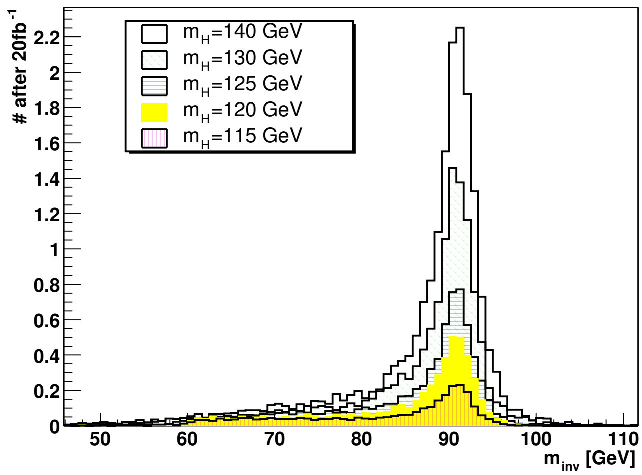

(a)

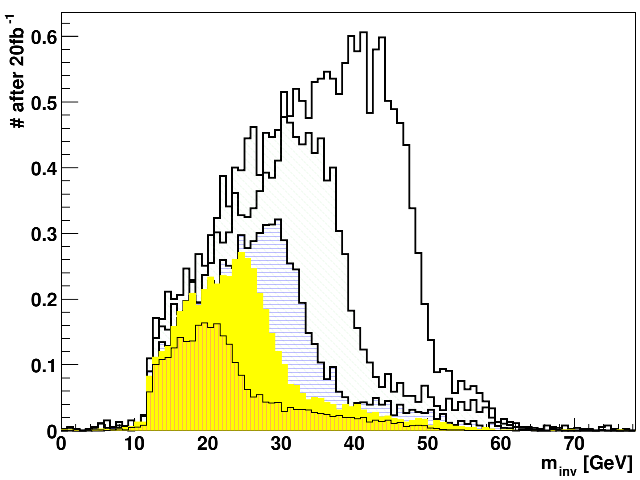

(b)

Figure 7.1: *Distribution of the invariant mass of two muons in the low luminosity case for signal samples with various Higgs masses: (a) Invariant mass distribution of the real Z boson candidate (b) Invariant mass distribution of the virtual Z boson candidate. The curves are the simulated distributions for a Higgs boson mass of 140 GeV, 130 GeV, 125 GeV, 120 GeV and 115 GeV.*

The shape of the distributions of the virtual Z mass also changes with Higgs mass, while the shape of the distribution of the real Z mass is not expected to change, and indeed does not show a significant variation. In principle, cuts on the value of the on-mass shell Z boson do not have to be changed for various Higgs masses. For lower Higgs massses, however, where it is more important to minimise the signal losses, the cuts might be relaxed. The invariant mass of the virtual Z mass decreases with decreasing Higgs mass as expected, and therefore the cuts on the Z^* mass is adapted to the Higgs mass value considered.

The γ radiation is done with PYTHIA for these data samples. A more exact treatment of the γ radiation could have been done with PHOTOS [BW94] but it is checked on generator level that the change of the distribution is very small. The resulting Higgs mass distribution for a mass of 130 GeV with PYTHIA treatment of γ-radiation and with PHOTOS is shown in Fig. 7.2.

The distribution of the invariant masses of the main backgrounds is plotted in Fig. 7.3. In Fig. 7.3(a) the real Z candidate is plotted whereas in Fig. 7.3(b)

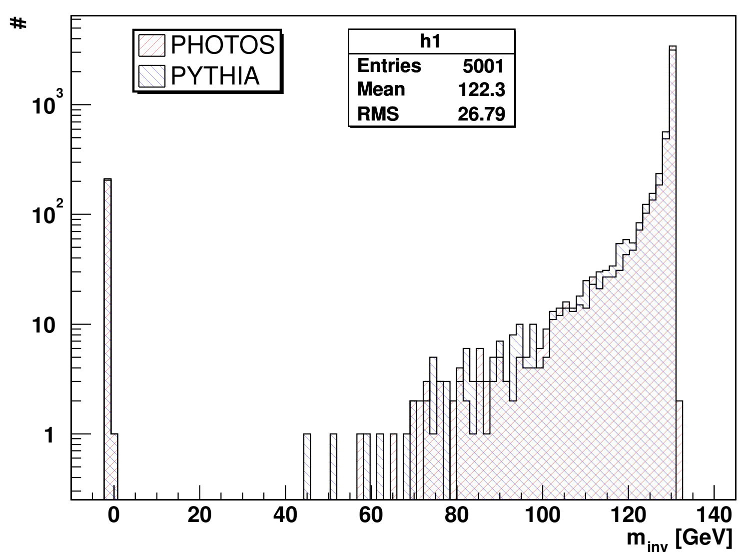

Figure 7.2: *Distribution of the generated Higgs mass for a mass of 130 GeV. For comparison the entries are unweighted. The red curve (light shaded) is the curve with γ radiation done with PHOTOS, the blue (dark shaded) is the curve with PYTHIA.*

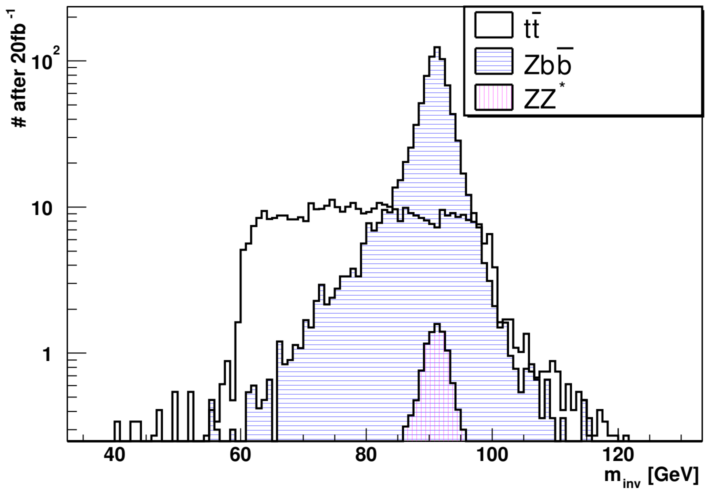

(a)

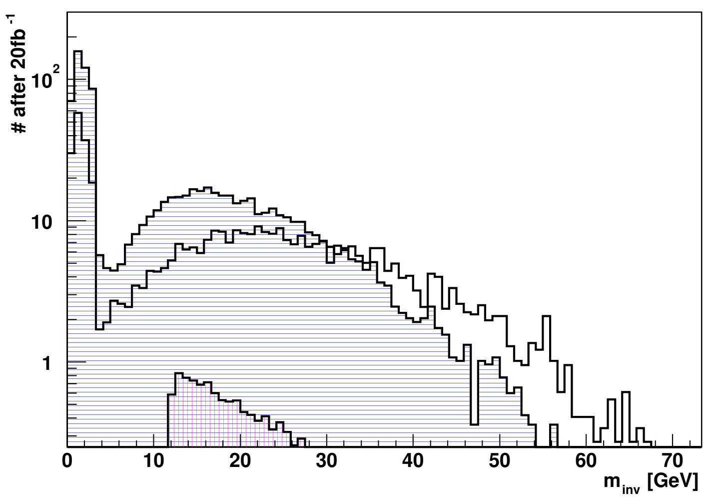

(b)

Figure 7.3: *Distribution of the invariant mass of two muons for the background processes. (a) Invariant mass distribution of the real Z boson candidate (b) Invariant mass distribution of the virtual Z boson candidate. The curves are the distribution of the* $\mathrm{t\bar{t}}$ *background, the* $\mathrm{Zb\bar{b}}$ *background and the ZZ* background.*

the virtual Z candidate is plotted. The distribution shows sharp edges because of the preselection cuts. In addition, the pairing of muons based on the generated four-momenta can be different from the one made on the basis of reconstructed properties. Therefore events show up outside the regions defined by the preselection cuts. For this reason the distribution of the virtual Z mass shows a peak at low masses for both the $t\bar{t}$ and the $Zb\bar{b}$ background.

There is no real Z boson in the $t\bar{t}$ background and therefore the invariant mass of two muons only by chance lies in the mass region of a real Z boson. One can see that the invariant mass distribution of the two muons forcing the real Z boson mass is flat over the preselected area. The Z mass cut thus is a good criterion to suppress this background. This cut, however, does not suppress the $Zb\bar{b}$ background due to the presence of a real Z, see Fig. 7.3(a). The ZZ^* background is signal-like, and cannot be suppressed beyond the preselection level. The Z mass cuts applied and their rejection power can be found in Tab. 7.1.

Table 7.1: *Values for the Z mass cut and their rejection power. The Z mass cuts are the same for both the low and the high luminosity phase. The rejection power of the cuts is given for the low luminosity samples.*

	cut on the Z mass		rejection on			
m_H in GeV	virtual in GeV	real in GeV	signal	$t\bar{t}$	$Zb\bar{b}$	ZZ^*
140	20-60	80-96.7	25%	90%	83%	61%
130	18-60	80-96.7	32%	89%	81%	53%
125	10-60	60-96.7	2%	63%	66%	7%
120	10-60	60-96.7	5%	63%	66%	9%
115	10-50	60-96.7	6%	65%	66%	9%

Cut on the transverse momenta:

The muons of the Higgs signal have high values of p_T compared to many background processes. The p_T spectrum for the signal events is shown in Fig. 7.4. The p_T distributions of the muons with highest and second highest transverse momentum only slightly depend on the Higgs mass (compare to Fig. 7.4(a)-(b)), but the p_T distributions of the muon with the lowest and the second lowest transverse momentum show a clear dependence (compare to Fig. 7.4(c)-(d)).

The decay products of the on-shell Z boson are often the muons with the highest and second highest p_T, while the muons with the lowest and second lowest p_T come from the off-mass-shell Z boson.

In comparison with the p_T spectra of the background processes (depicted in Fig. 7.5) the muons with the highest and second highest p_T (compare to Fig. 7.4(a)-(b) and Fig. 7.5(a)-(b)) in each Higgs event have a distribution similar to the background. This is due to the fact that events from the dominant background processes contain an on-mass-shell heavy gauge boson in their decay chain. For all backgrounds these gauge bosons (either Z bosons for the ZZ^* and $Zb\bar{b}$ background or W bosons for the $t\bar{t}$ background) are forced to decay directly into muons. So the additional contribution of muons from decays of quarks originating from the heavy gauge boson decay are neglected. On the other hand p_T distributions of the muons with the lowest and second lowest transverse momentum of each event, shown in Fig. 7.4(c)-(d) and Fig. 7.5(c)-(d), are quite different from the signal distributions. The background distributions peak at very low transverse momenta due to the softer muons originating from the b quarks in the $t\bar{t}$ and $Zb\bar{b}$ background. The cuts on the backgrounds are summarised in Tab. 7.2.

Table 7.2: *Values for the cuts on the transverse momenta and their rejection power. The selection cuts are the same for both low and high luminosity. The rejection power of these cuts is given for the low luminosity sample.*

	cut on p_T				rejection on			
m_H in GeV	highest in GeV	2. highest in GeV	2. lowest in GeV	lowest in GeV	signal	$t\bar{t}$	$Zb\bar{b}$	ZZ^*
140	15	12	12	8	19%	54%	81%	38%
130	15	12	12	8	28%	55%	83%	41%
125	15	11	11	8	32%	56%	86%	53%
120	9	8	8	6	17%	32%	63%	32%
115	8	7	6	5	11%	19%	42%	12%

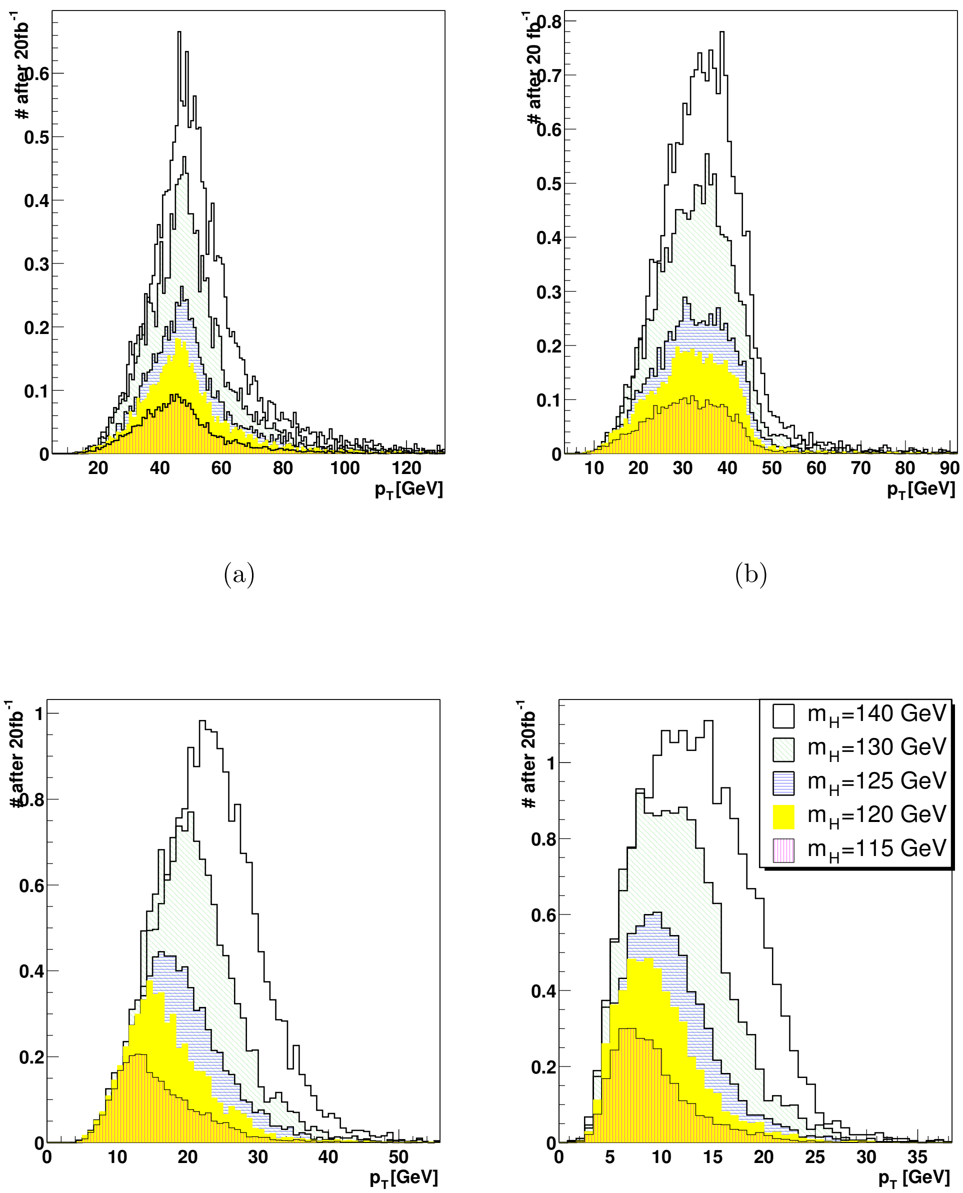

(a) (b)

(c) (d)

Figure 7.4: *Distribution of the sorted p_T's of the signal events for low luminosity. (a) highest p_T, (b) second highest p_T, (c) second lowest p_T, (d) lowest p_T. As in Fig. 7.1 the curves are the simulated distributions for a Higgs boson mass of 140 GeV, 130 GeV, 125 GeV, 120 GeV and 115 GeV.*

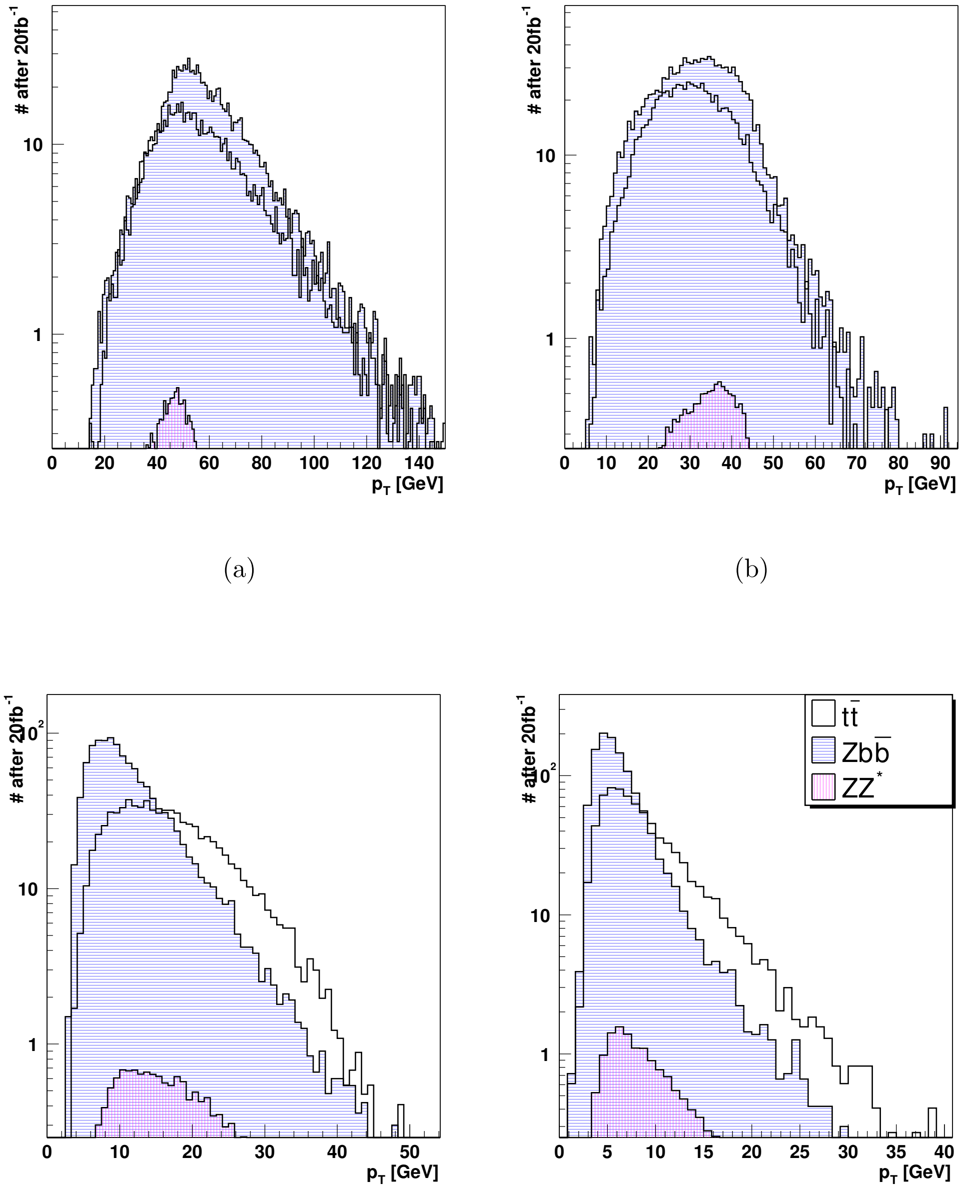

(a) (b)

(c) (d)

Figure 7.5: *Distribution of the sorted p_T's of the background events for low luminosity. (a) highest p_T, (b) second highest p_T, (c) second lowest p_T, (d) lowest p_T. As in Fig. 7.3 the curves are the distribution of the* $\mathrm{t\bar{t}}$ *background, the* $\mathrm{Zb\bar{b}}$ *background and the ZZ^* background.*

7.2 Muon Isolation Cut

An important characteristic of the signal events is the presence of four isolated muons in the final state. This is also true for the ZZ^* background, but the backgrounds $t\bar{t}$ and $Zb\bar{b}$ have two muons coming from b-jets, which therefore are non-isolated. These latter backgrounds can be suppressed significantly by an application of an isolation criterion.

Already at the High Level Trigger a selection on the muon isolation is done. Since this selection is not incorporated in the data samples used, the rejection power of the selection cuts applied offline is increased. It has not been studied up to now if an additional improvement compared to the offline isolation criteria is obtained by the selection on Trigger level.

In order to determine whether a muon is isolated, an existing ORCA package, the *Muon Isolation* [A$^+$02] is used. This package provides three isolation techniques: the calorimeter isolation considering the deposited energy in the calorimeter, the pixel isolation reconstructing tracker tracks around the muon and finally the tracker isolation using full reconstructed tracks. The calorimeter isolation is less effective at high luminosity as more pile-up events are included in the energy sum. The pixel isolation is less sensitive to pile-up events as only tracks originating from the same collision vertex are considered. This package requires the reconstruction of three pixel hits and therefore it is sensitive to inefficiencies and not as robust as the tracker isolation. In this thesis only the tracker isolation package, and for some values of the Higgs mass at low luminosity also the calorimeter isolation package, was applied. For the high luminosity phase only the tracker isolation was found to be useful.

The packages search for tracks or energy clusters, respectively, in a cone $\Delta R = \sqrt{\Delta\eta^2 + \Delta\phi^2}$ around a muon and sum up p_T or E_T found within this cone. If the sum over all transverse momenta or the sum of the transverse energy deposits exceeds a maximum value p_T^{max} (E_T^{max}) a muon is considered non-isolated. The threshold value and the size of the cone have to be optimised in order not to reject isolated muons with uncorrelated soft particles from pile-up in their proximity, while still efficiently rejecting non-isolated muons accompanied by jets. The muon isolation was applied on all of the four muons in order to suppress efficiently the $\mathrm{t\bar{t}}$ and $\mathrm{Zb\bar{b}}$ backgrounds, although only two of the four muons of these backgrounds are non-isolated. For tracker isolation the cone $\Delta R = 0.24$ was found to be the optimal choice. For a Higgs mass of 130 GeV the tracker isolation cut $p_{T,max} = 4.0\,\mathrm{GeV}/c$ rejects 9 % of the signal, 98 % of the $\mathrm{t\bar{t}}$ background, 89 % of the $\mathrm{Zb\bar{b}}$ background and 8 % of the ZZ^* background after all other cuts.

Fig. 7.6(a) shows the deposited transverse momentum of the signal and the $\mathrm{t\bar{t}}$ and $\mathrm{Zb\bar{b}}$ backgrounds around the muon track for a cone size of 0.24 after the Z mass cuts and the p_T cuts for a Higgs mass of 130 GeV. Cone size 0.24 has the optimal size for an isolation cut. A small peak invisible in Fig. 7.6(a) peak occurs at 10 GeV, because any single transverse momentum above 10 GeV is set to 10 GeV.

Fig. 7.6(b) shows the deposited transverse energy of the signal and the $\mathrm{t\bar{t}}$ and $\mathrm{Zb\bar{b}}$ backgrounds around the muon track after all other cuts including the tracker isolation 130 GeV. For the isolation in the calorimeter a wider cone was chosen, $\Delta R = 0.45$. For a Higgs mass of 130 GeV, a calorimeter isolation cut $E_{T,max} = 11.5\,\mathrm{GeV}$ rejects a relatively large fraction of the signal, 16 %, but also much of the remaining background, 62 % of the $\mathrm{t\bar{t}}$, 55 % of the $\mathrm{Zb\bar{b}}$ and 13 % of the ZZ^* background after all other cuts including tracker isolation. Application of this cut therefore results in a small gain in signal significance. For lower Higgs boson masses, $m_H = 115\,\mathrm{GeV}$ and 120 GeV, the cut on calorimeter isolation is effectively disabled by setting the cut at a very high value (26.0 GeV). This is necessary because signal losses have to be minimised, given the anyway very small signal rate. The cuts for both, tracker isolation and calorimeter isolation are summarised in Tab. 7.3. The rejection power is given after all other cuts.

The high rejection power of the muon isolation cut is of crucial importance to this analysis and depends on details of the generator options, like multi-parton interactions, and on details of the detector and pile-up simulations. Without studying different options, no reliable systematic error on the present study can be assigned. This remains a task for the future.

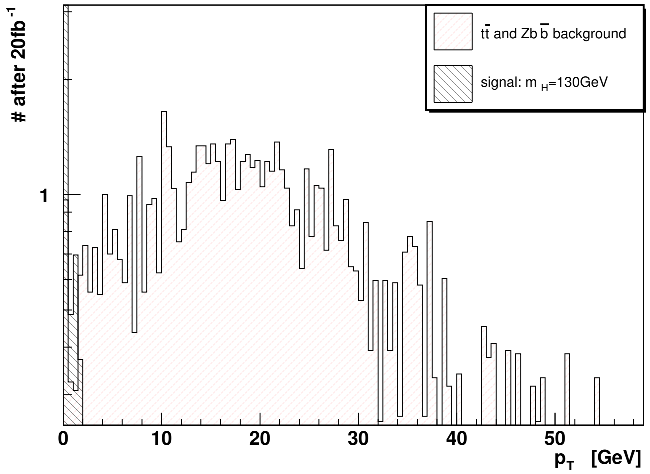

(a)

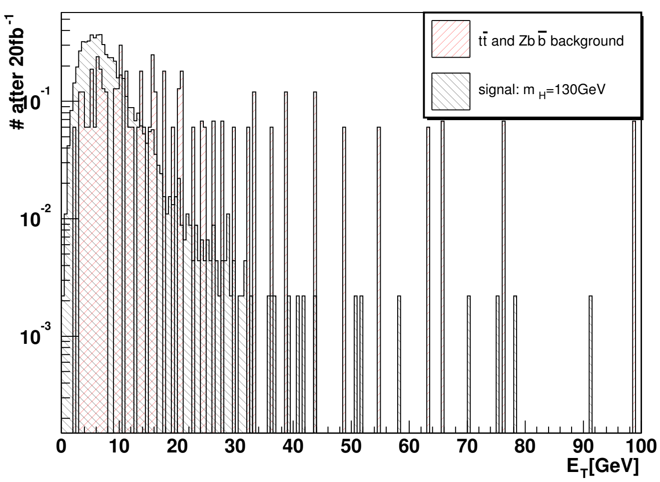

(b)

Figure 7.6: *Isolation: deposited $p_{T,deposited}$ ($E_{T,deposited}$) for the signal and the* $\mathrm{t\bar{t}}$ *and* $\mathrm{Zb\bar{b}}$ *backgrounds around the muon track in the low luminosity phase: (a) shows the tracker isolation with a cone size of 0.24 after all cuts, (b) shows the calorimeter resolution in a cone size of 0.45 after all other cuts including the tracker isolation cut.*

Table 7.3: *Values for the isolation cut for the low luminosity case. The cone used for the tracker isolation is cone $\Delta R = 0.24$, the cone for the calorimeter isolation is cone $\Delta R = 0.45$.*

Higgs boson mass in GeV	isolation cut: Tracker p_T in GeV	Calorimeter E_T in GeV	rejection on signal	$t\bar{t}$	$Zb\bar{b}$	ZZ^*
140	> 3.5	> 11.5	20%	99%	97%	22%
130	> 4.0	> 11.5	23%	99%	97%	20%
125	> 4.0	> 15.0	15%	99%	94%	16%
120	> 4.5	-	10%	98%	81%	9%
115	> 4.5	-	10%	97%	75%	9%

7.3 Vertex Cut

Events with muons in different collisions, two or three muons in one collision and one or two in another, may become a significant source of background due to the much higher rates compared to $4\,\mu$ processes. Requiring that all four muons must originate from the same primary vertex will significantly reduce such backgrounds. An efficient quantity to cut on is the distance in longitudinal vertex position of the muons, in other words Δz_{vert} of the z coordinates of pairs of muons at the point of closest approach to the beam line.[1]. For signal events, the value of Δz_{vert} for the muon pair with the largest distance in z is plotted in Figure 7.7(a). This distance is much smaller than the luminous region of the LHC beams of about 5 cm, which is also shown in Figure 7.7(b). These two distributions set the scale for the separation in z of a muon originating from another collision in the same bunch crossing. At a loss of only 1% in signal events a cut on the maximum distance in z_{vert} at 0.04 cm will reject events with a muon from a different collision vertex with a probability of 99.7 %.

Such a vertex cut also reduces slightly the background from muons originating

[1] Technically, the z position of each muon at the x, y position of the primary vertex is reconstructed applying the method *StateAtPoint* of the class *RecTrack*. The position of the primary vertex is obtained from the method *smearedPrimaryVertex* of the class *PrimaryVertexProvider*. This is not yet a final implementation of the cut suggested here.

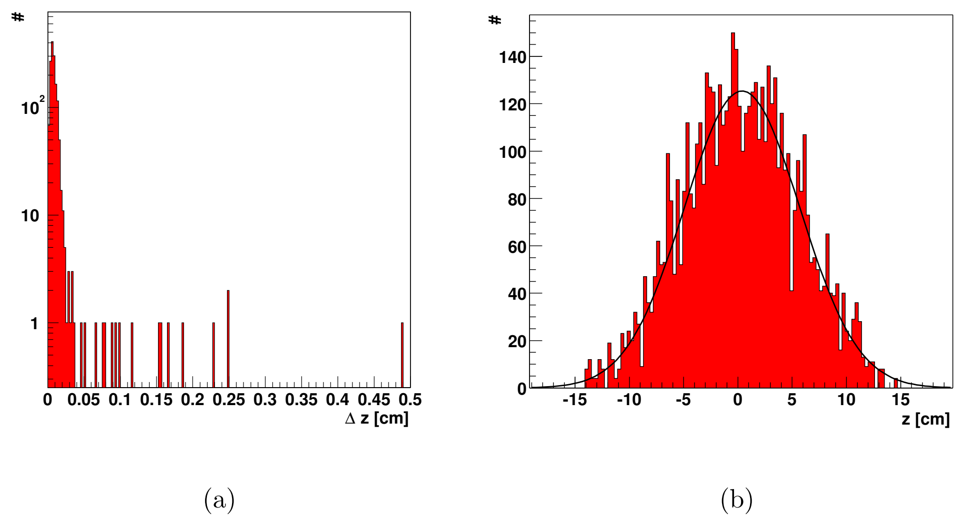

Figure 7.7: *(a) shows the distribution of the maximum difference in the longitudinal vertex position, Δz of the four muons coming from the signal. 99% of the signal events have a Δz smaller than 0.04 cm. This is much smaller than the size of the luminous region of the LHC beams of about 5 cm, which is shown in Figure 7.7(b).*

from b decays. On a sample of Z$b\bar{b}$ events, a reduction of 10 % after all other cuts was observed. However, the vertex cut was not applied as a standard cut in this analysis, but was only introduced to suppress backgrounds with an additional muon from another collision, as is discussed in Sect. 7.9 below.

7.4 Further Cuts to be applied

To study the channel H$\rightarrow$ZZ* $\rightarrow 4\mu$ in detail many more cuts could be used than the ones applied in this study. For several reasons these cuts are beyond the scope of this work.

In this thesis there are no cuts on the behaviour of the Higgs boson itself applied - apart from the Higgs mass cut. This is due to the changes arising from next-to-leading order processes. At the moment the event generators simulate only the behaviour of the processes in leading order. Only the cross section is rescaled to next-to-leading order. For Higgs boson production the cross section nearly doubles for next-to-leading order as pointed out in Sect. 5.3. At the next-to-leading order approximation, the Higgs boson is often accompanied by additional gluons and quarks. So the signature of the signal changes slightly for higher order corrections. But also the transverse momenta of the Higgs boson change.

In future some characteristics of the background can be used to assign events to the background. For example a b-tagging can be applied to reject backgrounds with a b quark in the decay chain like $\mathrm{t\bar{t}}$ and $\mathrm{Zb\bar{b}}$. According to the tracker technical design report [TRA98], b-tagging efficiencies of 40-50% can be obtained for b-jets ranging from 50 GeV to 200 GeV, that means that at best a reduction of 50% of the $\mathrm{Zb\bar{b}}$ and $\mathrm{t\bar{t}}$ background can be obtained.

In this study four muons need to be reconstructed to analyse the process. Even with a high muon reconstruction efficiency, the probability to reconstruct four muons will reject a high percentage of events, in this case about 20% of all events. So further studies must be made whether a reconstruction of only three muons plus an isolated track in the tracker are sufficient for the analysis. For these studies the additional backgrounds with 3μ's and the behaviour of the minimum bias events have to be understood very well. A few studies of three muon backgrounds can be found in Sect. 7.9 where the influence of multiple collisions is studied.

7.5 Remarks on Signal Visibility

There are several methods to estimate the probability of new physics discovery in a future experiment. These methods can be coarsely classified as event counting and likelihood methods. Whereas event counting methods rely on a binning and a good knowledge of the expected and observed signal and background events, likelihood methods also take the shape of the curves into account. In the following, some event counting and likelihood methods are investigated in a large number of simulated experimental results. In this thesis only one example with a similar number of signal events and background events as expected for the $\mathrm{H} \rightarrow \mathrm{ZZ}^{*} \rightarrow 4\mu$ is given. A more detailed description can be found in [BQ02]. A relatively simple and practical likelihood method is proposed, which still holds in the case of small statistics.

Event counting methods:
An overview over significances S is given, here significance is defined as the number of standard deviations an observed signal is above the expected background fluctuation. The general agreement is that the value of S of a signal should exceed five. The corresponding one-sided Gaussian probability, in other words the integral of the Gaussian distribution from five to infinity, is $0.29 \cdot 10^{-6}$. This means the probability of a 5σ signal arising from background is $0.29 \cdot 10^{-6}$.

Counting methods use the number of signal events N_s and the number of background events N_b observed in some signal region to define the significance. This procedure requires working with binned distributions, which in turn means that bin position and bin widths have to be fixed; if the bin positions and widths are fixed after observation of an excess above the background somewhere, this opens possibilities for subjective choices. Furthermore the optimal choice of a signal region around the mean to maximise the sensitivity depends on the background level, which is another disadvantage of such methods.

Three different types of these methods are presented:

- $S_{c1} = \frac{N_s}{\sqrt{N_b}}$,
- $S_{c2} = \frac{N_s}{\sqrt{N_s+N_b}}$,
- $S_{c12} = 2 * (\sqrt{N_s + N_b} - \sqrt{N_b})$ [BK00].

Likelihood methods:
Likelihood methods are frequently used in data analysis to extract the number of signal and background events from a fit to a distribution which discriminate signal and background. The ratio of likelihoods Q of the null hypothesis or background only hypothesis L_B and an alternative hypothesis, the signal plus background hypothesis L_{S+B} have already been used at LEP [GK02]. For convenience, the logarithmic form $2 \ln Q$ is used as the test statistic since this quantity is approximately equal to the difference in χ^2 in the high statistics case. So as a new estimator for the significance S_{L2} is defined as:

- $S_{L2} = \sqrt{2 \ln Q} = \sqrt{2(\ln L_{S+B} - \ln L_B)}$.

In this thesis special emphasize is put on a likelihood fit to determine the contributions from signal and background events in the distribution of the invariant mass of observed final states. The background and background-plus-signal distribution is the distribution of simulated data. Later in the experiment the background distribution could be taken from data. The fit for the signal is in my case a Gaussian with a radiative tail parametrised by the function $f_{tail}(m_{4\mu})$. The radiative tail is parametrized as follows: For all invariant four muon masses $m_{4\mu}$ larger than m_H the function is zero, for four muon masses with smaller than m_H the function is given in Eq. 7.1:

$$f_{tail}(m_{4\mu}) = N_{S,additional} * \frac{(m_{4\mu} - m_H)^2}{2 * \tau^3} * exp(\frac{(m_{4\mu} - m_H)}{\tau}) \tag{7.1}$$

The distribution for the background is a straight line. In the case of low statistics the shapes of the distribution are fixed and only N_s and N_b are free parameters.

Monte Carlo Study of estimators for signal significance:

If statistics are sufficiently large, all of the above estimators show a Gaussian distribution. When searching for something new, one very often deals with a small statistics problem. At the statistical limit, two important questions arise:

- What is the probability to actually observe an existing signal with a predefined signal significance with a given amount of data?
- What is the probability that the signal is merely a fluctuation of the background?

To answer the questions, Monte Carlo studies with a large number of simulated experiments - hereafter called toy experiments - have therefore to be performed to find the probability density function of the significance. The probability density function may turn to be far from Gaussian, because the common rules of statistics and many familiar theorems are no longer valid in the realm of small statistics. For the H → ZZ* → 4 μ channel, one expects for a Higgs mass of 130 GeV and an integrated luminosity of 20 fb^{-1} about 5 signal events over 2.5 background events. An example of one toy experiment at small statistics is shown in Fig. 7.8. The symbols with error bars each indicate a mass value drawn randomly according to the mass distribution of the weighted sum of signal and background events. The curve shows the result of an unbinned likelihood fit to these mass values.

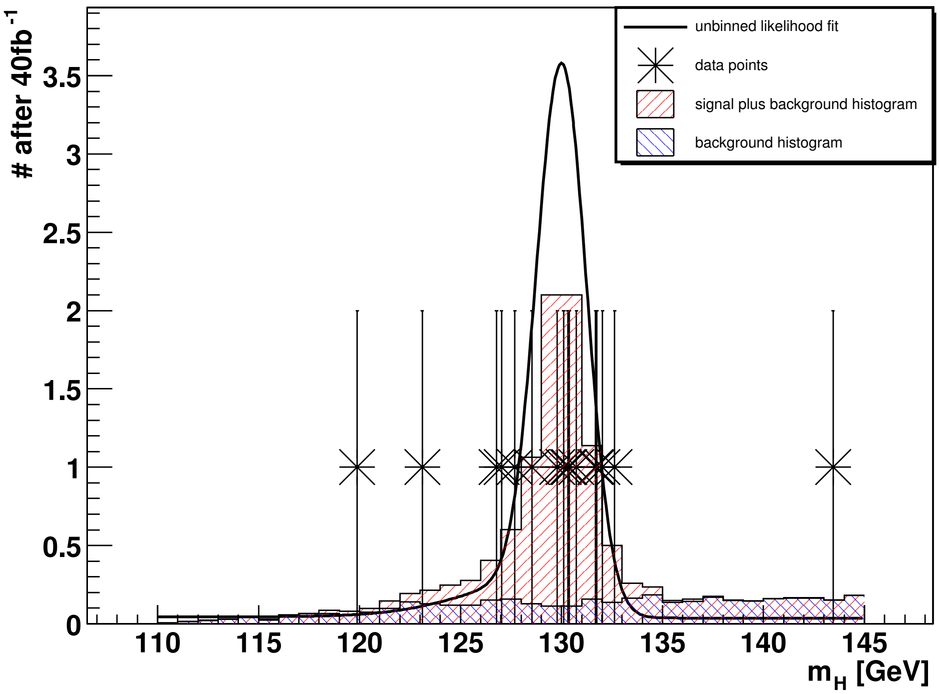

Figure 7.8: *Example of an unbinned likelihood fit to a number of data points shown as symbols. The data points demonstrate how the real data could look like after 40 fb^{-1}. The shaded histogram shows the distribution of signal plus background obtained from a large number of weighted simulated events. For the unbinned likelihood for signal plus background a Gaussian plus a flat distribution is fitted.*

The distribution of various definitions of significances from 10.000 of such toy experiments is shown in Fig. 7.9. The number of signal events is 25, the number of background events 10. It can be seen that S_{c1} gives much larger sensitivities than S_{c2} or S_{l2}. Gaussian fits are overlayed in the figure and the agreement is good for S_{c12} and S_{l2}, while S_{c1} is only poorly described by the Gaussian fit. Tab. 7.4 shows the mean and r.m.s. of the various estimators. It can be seen that S_{c1} gives the highest significances.

Beside the distributions of Fig. 7.9, the reliability of an estimator of significance has to be checked in addition, in other words how often a false discovery would be claimed for a certain choice of the minimum required significance. The same

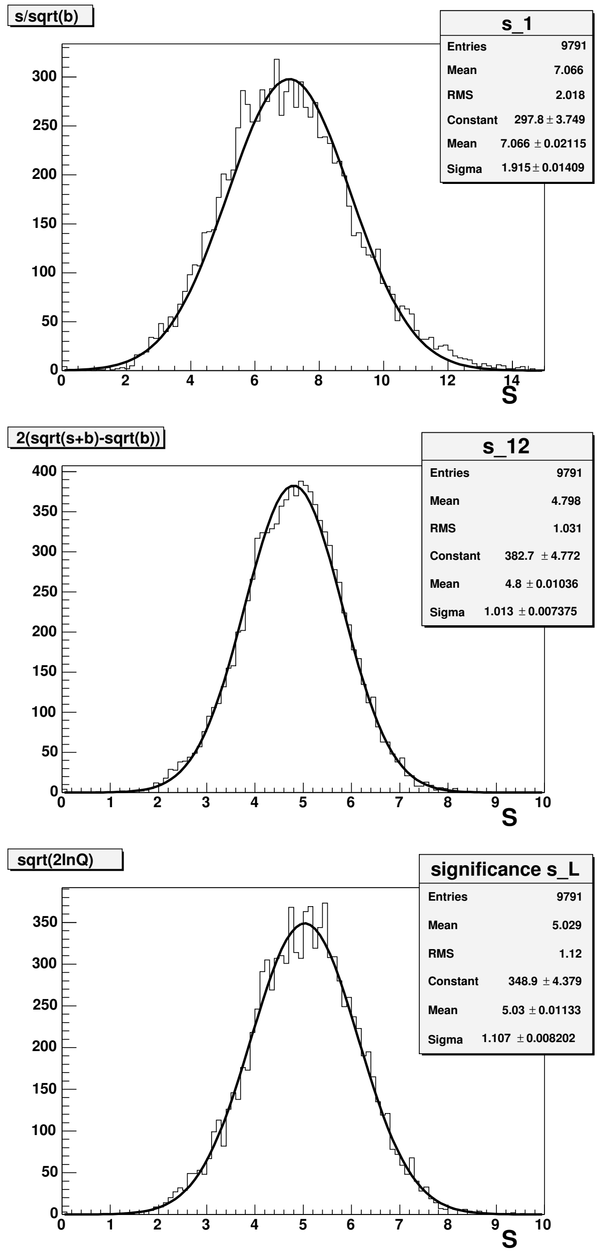

Figure 7.9: *Histograms of S_{c1}, S_{c12} and S_{L2} determined from from 9 791 successful fits to toy experiments, with N_b, N_s and m_0, the particle mass, as free parameters. The curves show the results of a Gaussian fit to the distributions. In addition to the "Mean" and "RMS" of the histograms the parameters of the fitted Gaussian, "Constant", "Mean" and "Sigma", are shown in the plots. The number of signal events is 25, the background level amounts 40%.*

Table 7.4: *Summary of the mean and r.m.s. of the various definitions of significance for the case discussed in the text.*

	mean significance	r.m.s..
S_{c1}	7.1	2.1
S_{c12}	4.8	1.0
S_{L2}	5.0	1.1

distributions as in Fig. 7.9 are shown in Fig. 7.10 but this time for background only. S_{c12} and S_{l2} are well described by a Gaussian distribution, but it has to be noted that the probability to find any entry beyond 5 in one million experiments is expected to be only about 0.3 for a perfect Gaussian shape. Fig. 7.11 shows the separation between the background only and signal-plus-background sample. The figure shows that the samples are only poorly separated using the estimator S_{c1}.

Practical method to determine the expected significance:
Having shown above that the estimator of significance based on the likelihood ratio of the signal-plus-background and the background-only hypothesis, $S_{L2} = \sqrt{2\ln Q}$, is very well described by a Gaussian shape and that the standard deviation of this Gaussian is one for a pure background sample in the absence of a signal, only one task remains to be done: to define a practical and simple method for estimating the expectation value of S_{L2} for a given amount of data and with presence of a signal. Therefore in this note a new approach is presented which evaluates the whole downweighted Monte Carlo statistics. Although there is no mathematical proof for this approach up to now the estimated significance of this method is equal to the mean of the toy experiments.

In the simpler case with large uncertainties on the signal and background rates the detection of a signal depends on a comparison of the signal and background shapes, leading to the observed Gaussian behaviour of S_{L2} in the cases studied here. Only the mean value of the distribution of S_{L2} is needed to quantify the expected discovery potential of a signal while keeping the fake probability due to background fluctuations under control.

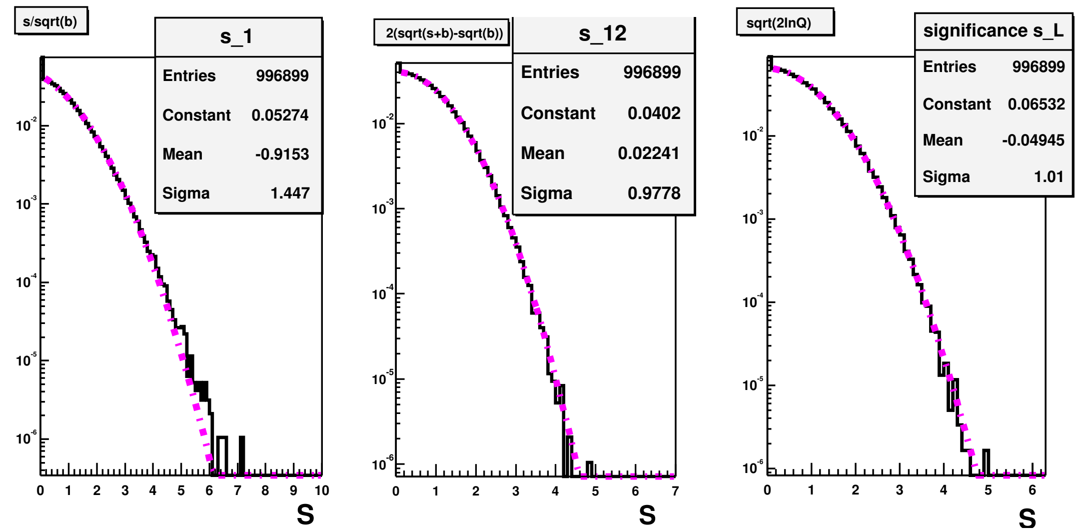

Figure 7.10: *Probability density functions determined from 1 000 000 toy experiments for background only, in the absence of a real signal, with N_s and N_b as free parameters and m_0 fixed. Again, the estimators of significance S_1, S_{12} and S_{L2} are shown. The fit parameters shown in each plot refer to the parameters of a Gaussian distribution. The distribution of S_{c1} cannot be described well by a Gaussian centred around zero, the standard deviation is far above one, and there are too many events observed at a significance beyond five, which should only occur with a probability of about $0.3\,10^{-6}$, in other words 0.3 expected occurrences for a total of about one million samples. The estimators S_{c12} and S_{L2}, on the contrary are well described by a Gaussian with mean around zero and a standard deviation close to one.*

Instead of performing many toy experiments, this mean value can be obtained by performing likelihood fits for the background-only and the signal-plus-background hypothesis on a large statistics sample of events, namely the weighted sums of the accepted signal and background events from Monte Carlo simulation as a function of the invariant mass. This is illustrated in Fig. 7.12, which shows invariant mass distribution for the H→4μ channel over a rather small background. The two curves show the results of two binned log-likelihood fits, the first one with a function describing the signal-plus-background shape and the straight line which assumes that there is only background. The bin size of the sample of weighted simulated events is small compared to the bin size that would be usable for the small number of expected signal events, and

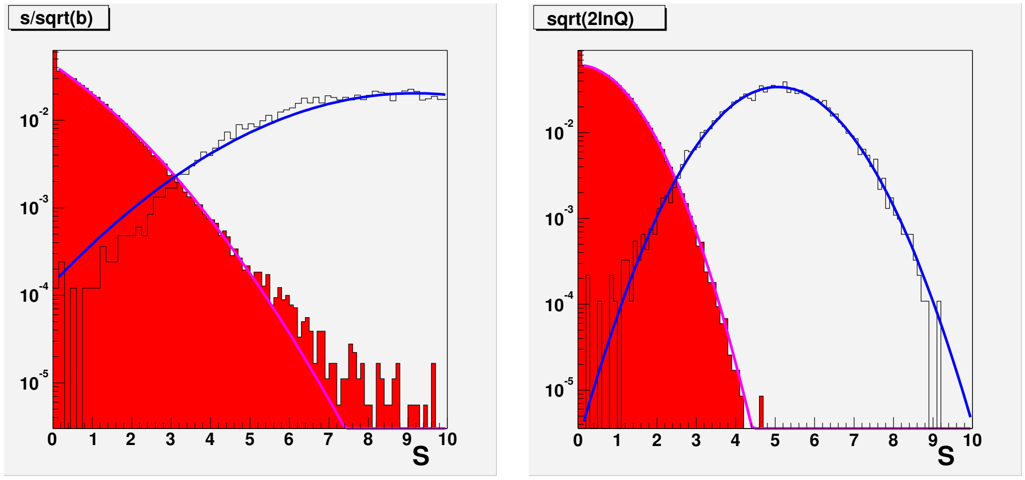

Figure 7.11: *Probability density functions of estimators of significance* S_{c1} *and* S_{L2} *for small statistics (25 signal events within* $\pm 1.5\sigma$ *over a background of 10 events). Filled: pure background sample, open histogram: background plus signal. The background distributions are based on 200 000 toy experiments, the distributions for signal plus background on 10 000 toy experiments. The Gaussian fit to the distribution of* S_{L2} *for the background-only sample has a mean of* -0.004 *and* σ *is 1.0 .*

therefore the performed binned fit is a good approximation to the unbinned fits on the small samples of expected real data. In the limit of zero bin size binned and unbinned likelihood fits become equal.

To compare the outcome of the toy-experiments with unbinned likelihood and the binned likelihood fit from the histogram fit, the distribution of $\sqrt{2\ln Q}$ of the toy-experiments shown in Fig. 7.13 is compared with the value from the binned likelihood. The mean value of the distribution is $< S_{l2} > = 3.4$, S_{l2} of the histogram fit is 3.2 with an r.m.s. of 1.0. So both values match taking into account the errors. Therefore a binned likelihood fit assuming Poisson statistics is a good approximation of an unbinned likelihood fit. Given that some kind of fit to determine the number of signal events above the background is usually performed anyway, the method suggested here to determine the significance of the observed peak does not imply a large extra effort.

To better understand the proposed method it is illustrative to investigate the

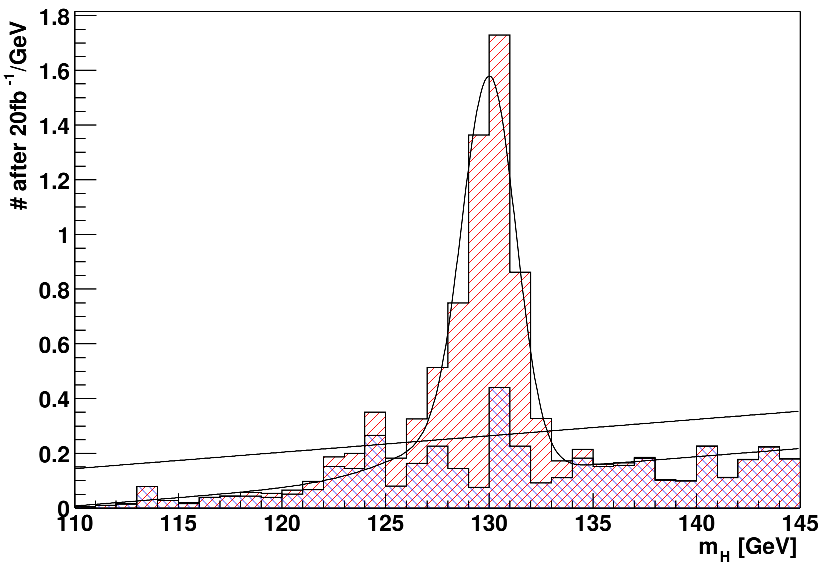

Figure 7.12: *Histogram of the reconstructed invariant mass of four muons, for an integrated luminosity of 20 fb^{-1}. The histogram is the weighted sum of signal events from H→4μ (shown in red) and of various background samples (blue). The straight line represents a fit for the background-only hypothesis, the curve is obtained under the assumption of the signal plus-background-hypothesis. In Appendix C the corresponding Figures for all simulated Higgs masses as well as Tables with the bin entries are given to redo a calculation of the likelihood estimator if needed.*

behaviour of the likelihood between the two extremes of the signal plus background and the background only hypotheses. A smooth change from one to the other can be obtained by varying the number of signal events and determining the minimum of the negative likelihood. The likelihood of such a fit is shown in Fig. 7.14. Near the minimum, the error in the number of signal events can be read off the curve at the point where the negative likelihood increases by 0.5. The significance S_{l2} takes the difference of the negative log-likelihood at zero signal events $L(N_s = 0)$ and at the minimum L_{min} as described in Eq. 7.2.

$$\ln Q = (-\ln L(N_s = 0)) - (-\ln L_{min}) \tag{7.2}$$

In the example shown here, the value at $N_s = 0$ is 5.1 above the minimum. There is an asymmetry in the curve, the rise towards small values is much larger than

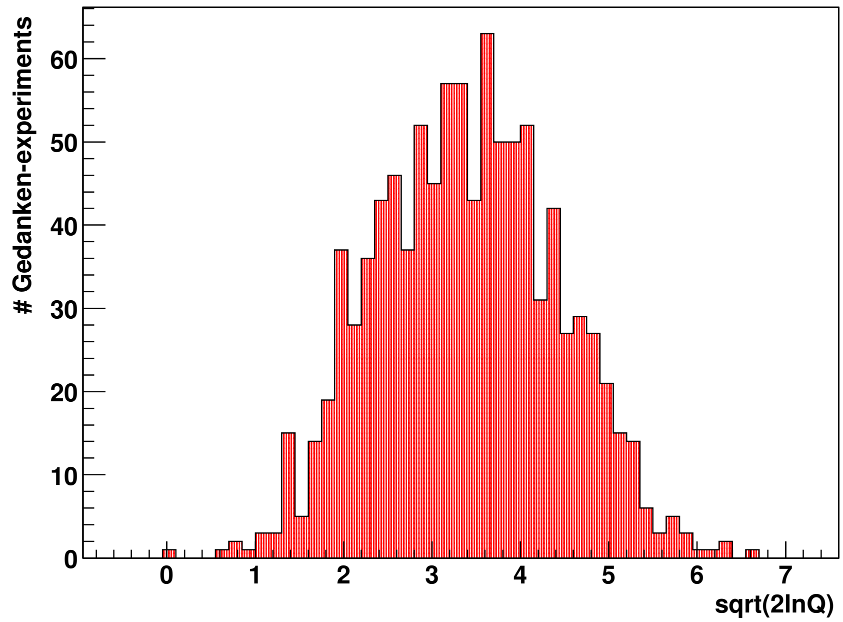

Figure 7.13: *Distribution of* $2\ln Q$ *from unbinned log-likelihood fits from 1000 simulated experiments, with simulated events which entered into the histogram of Fig. 7.12. The mean value of this distribution is 3.4 and agrees well with the value found above from the histogram fit.*

towards large values. The asymmetry is the reason why an estimate based on the likelihood values at the minimum and at zero is different from an estimator taking into account the number of signal events and its error.

There is a slight technical complication from the proposed procedure. The fitting tool used in this analysis ROOT assumes integer bin contents in the binned likelihood fits. Here, however, the sums of weighted simulated events are non-integer values. Because of the fine binning and the small statistics the bin content is very small, therefore the conversion to an integer poses a problem. Beside this the gamma-function used in the likelihood function has to be extended the generalised gamma-function taking into account non-integer values. Such a modified fit function has been provided as an addition to the ROOT framework, making its use technically easy.

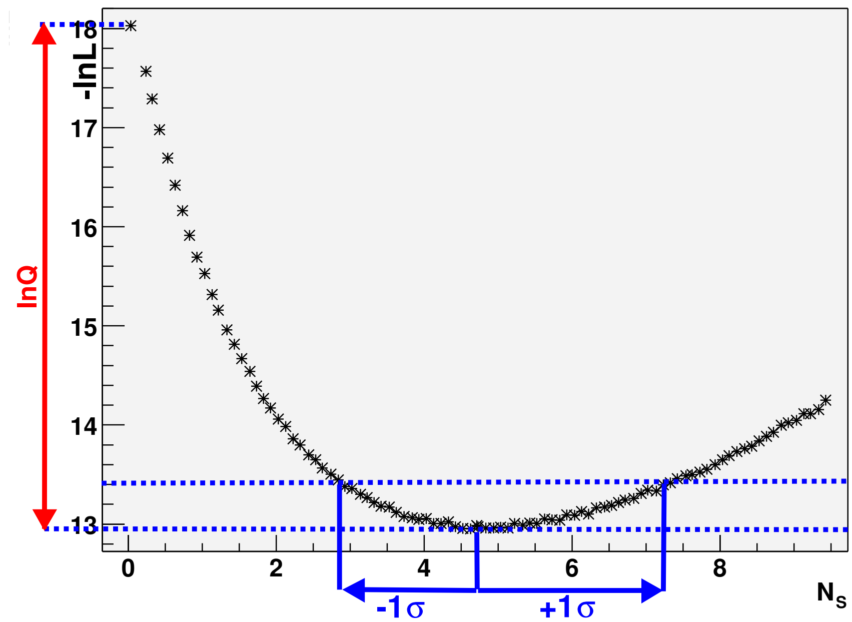

Figure 7.14: *The dependence of $-\ln\mathcal{L}$ on N_s for the histogram fit shown in Fig. 7.12. At each point on the curve, N_s is fixed, and a new fit is performed to find the minimum w.r.t. all other parameters. From this curve, the n-σ error bands for N_s can be determined from the increase relative to the minimum value, as is shown for the (in this case asymmetric) $\pm1\sigma$ error interval. The value of the likelihood at the best-fit point corresponds to $-\ln\mathcal{L}_{S+B}$, the likelihood value at zero signal events corresponds to $-\ln\mathcal{L}_B$, the difference thus is $\ln Q$.*

Conclusion:

In this section event counting methods were contrasted to likelihood methods. In the case of low statistics $S_{c1} = N_s/\sqrt{N_b}$ leads to a large overestimation of the significance and even worse often leads to high values of significance in cases where there is only background. The likelihood method S_{l2} gives the best performance. Among the event counting methods $S_{c12} = 2(\sqrt{N_s + N_b} - \sqrt{N_b})$ reaches an almost equally good performance. Likelihood methods offer the advantage of being independent of binning and independent of the definition of a signal region.

A practical method is suggested to determine the expected significance S_{l2}, which is based only on two binned likelihood fits to the invariant mass distribution with a fine binning, as is obtained from weighted simulated events.

7.6 Results on the Signal Visibility

To summarise the results of Sect. 7.1 the resulting cross sections determined from the fractions of Monte Carlo events surviving all cuts for $\mathrm{H} \to \mathrm{ZZ}^* \to 4\,\mu$ and for the sum of the main backgrounds $\mathrm{t\bar{t}}$, $\mathrm{Zb\bar{b}}$ and ZZ^* are given in Tab. 7.5.

Table 7.5: *Signal and total background cross sections. The cross section for the background refers to a range in the invariant mass of the four muons from 110 to 145 GeV. The cross sections for the signal may be converted into numbers of observed signal and background events by multiplication with the integrated luminosity.*

m_H GeV	σ_s fb	σ_b fb
140	0.463	0.232
130	0.261	0.197
125	0.208	0.392
120	0.162	1.747
115	0.091	2.962

The distributions of the invariant mass of the four muons for signal and background are summarised in Fig. 7.15. Individual distributions for each Higgs boson mass for low and high luminosity are shown in the figures in the Appendix C. To allow for a detailed numerical re-analysis, the bin entries of these distributions are available in tabulated form in the Appendix C. The number of events per bin given in Fig. 7.15 is normalised to an integrated luminosity of $20\,\mathrm{fb}^{-1}$, as expected after one year of LHC operation. The signal is clearly distinct from the background for Higgs boson masses above 120 GeV. The background levels are different for each Higgs boson mass studied, because optimised cuts according to Tab.s 7.1, 7.2 and 7.3 in Sect. 7.1 were applied. The background composition in the whole mass range of 110-145 GeV for a Higgs boson mass of 130 GeV is 61% from ZZ^*, 33% from $\mathrm{Zb\bar{b}}$, and the rest is surviving $\mathrm{t\bar{t}}$ background. The relative statistical error of the background level arising from the limited Monte Carlo statistics, within a range of four times the Higgs mass resolution around the centre of the signal peak, $m_\mathrm{H} \pm 2\Delta_{m_\mathrm{H}}$, is about 10%. If the whole mass range

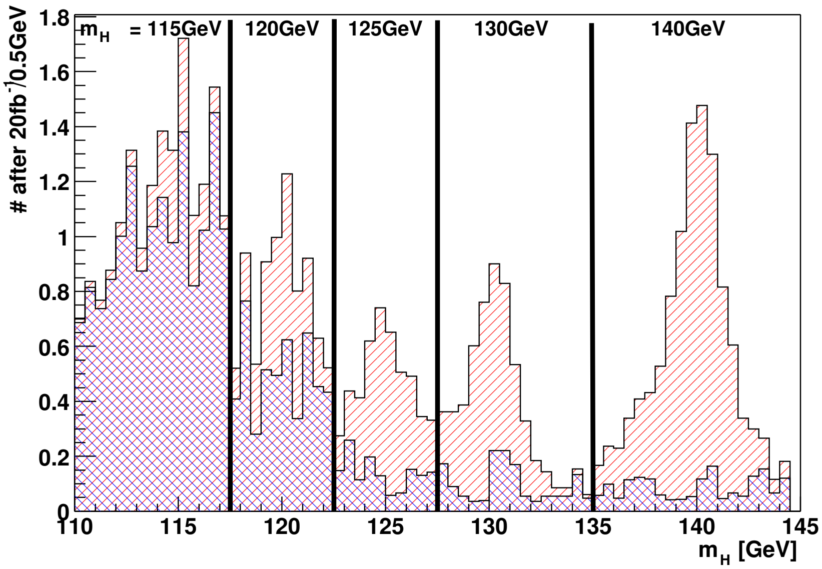

Figure 7.15: *Distributions of the four-muon invariant mass for signal plus background and for background only for Higgs boson masses of 115 GeV, 120 GeV, 125 GeV, 130 GeV and 140 GeV at low luminosity. For each value of Higgs boson mass the corresponding cuts described in Sect. 7.1, Tab.s 7.1, 7.2 and 7.3 have been applied.*

110-145 GeV is considered, the uncertainty on the background level amounts to about 4%. The latter is the error to be used when the background is extrapolated to the signal region by performing a fit of the signal and background shapes to the invariant mass distribution of the observed events. Thus, the error on the background is dominated by theoretical uncertainties.

To quantify the signal significance for each studied Higgs boson mass, results for the commonly used definitions of significance are summarised in Tab. 7.7. These are $S_{c1} = \frac{N_s}{\sqrt{N_b}}$, $S_{c12} = 2(\sqrt{N_s + N_b} - \sqrt{N_b})$, $S_{l2} = \sqrt{2 \ln Q}$ based on the likelihood ratio of fits assuming that only background or background plus signal are present, and a in the community of the CMS experiment newly proposed significance $S_{poisson}$ derived from the Poisson probability that the expected number of background events, N_b, fluctuates beyond the total number of observed events, $N_s + N_b$. The fitted signal and background cross sections and the mass resolution are summarised in Tab. 7.6. N_s and N_b were determined by integration of the signal-plus-background and the background-only distributions

Table 7.6: *Fitted cross sections of signal and background events accepted after all cuts at low luminosity, σ_s and σ_b, respectively, in the whole mass range and in a mass window of $m_H \pm 2\Delta_{m_H}$; the fitted Higgs boson mass resolution, Δ_{m_H}, is given in the third column. This analysis is optimised for an integrated luminosity of 20 fb^{-1} corresponding to one year of LHC operation.*

Higgs boson mass GeV	σ_s fb full range	Δ_{m_H} GeV	σ_s fb mass window $m_H \pm 2\Delta_{m_H}$	σ_b fb mass window $m_H \pm 2\Delta_{m_H}$
140	0.463	1.3	0.392	0.053
130	0.261	1.3	0.231	0.033
125	0.208	1.2	0.181	0.051
120	0.162	1.2	0.138	0.254
115	0.091	1.1	0.082	0.498

in a mass window of $m_H \pm 2\Delta_{m_H}$. The observed signal width is by far dominated by the detector resolution, because the natural Higgs width lies between about 0.03-0.08 GeV within the studied range in Higgs boson mass. When obtaining the Higgs mass width it has to be noticed that the radiative tail of the fit influences the magnitude of N_s and of the Higgs mass width σ_{m_H} in comparison to a fit without tail. This is because additional signal events are found and because the Gaussian gets smaller when it does not have to fit the additional muons in the radiative tail. The fit with radiative tail is equivalent to quantifying σ_{m_H} only for the Gaussian part of the histogram.

One can see that for all Higgs masses considered in this thesis the significance S_{l2} and S_{c12} and $S_{poisson}$ agree nicely, while S_{c1} gives much larger values at high Higgs boson masses, where the background under the signal is very small. S_{l2} and S_{c12} are most reliable under such conditions, in other words, following the common consensus that a discovery can only be claimed for significances above five, it will not be possible to claim a discovery of a light Higgs boson in the H$\rightarrow 4\,\mu$ channel alone after the first year of LHC operation.

Using the signal and background cross sections provided in Tab. 7.6, significances corresponding to other values of integrated luminosity can easily be calculated. The square of the likelihood significance, $S_{l2}^2 = 2\ln Q$, is proportional to the integrated luminosity. When calculating the significance corresponding to other integrated luminosities, one has to keep in mind a few things. For the low Higgs masses only a few events are in the fiducial acceptance of the CMS detector. Therefore the selection cuts are chosen to optimise both: the significance and the number of surviving Higgs events after the selection cuts optimised for an integrated luminosity of $20\,\mathrm{fb}^{-1}$. The selection cuts are softer the lower the Higgs mass (compare to Tabs. 7.1, 7.2 and 7.3). So when scaling the significance to higher luminosities the significances obtained from these calculations have to be understood as lower limit.

Table 7.7: *Estimators of significance* $S_{l2} = \sqrt{2lnQ}$, $S_{c1} = \frac{N_s}{\sqrt{N_b}}$ $S_{c12} = 2(\sqrt{N_s + N_b} - \sqrt{N_b})$ *and* $S_{poisson}$ *for an integrated luminosity of* $20\,fb^{-1}$ *corresponding to the first year of LHC operation at low luminosity, for several Higgs boson masses.*

Higgs boson mass GeV	S_{l2}	$S_{poisson}$	S_{c12}	S_{c1}
140	4.2	4.7	3.9	7.6
130	3.2	3.6	3.0	5.7
125	2.3	2.7	2.3	3.6
120	1.1	1.2	1.1	1.2
115	0.5	0.6	0.5	0.5

The signal significance obtained here is even higher than the one found in an older study [Dro97] of the discovery potential of a Higgs boson with a mass of 130 GeV in the channel H$\rightarrow 4\mu$, which was done with fast simulation. The cross section of the signal is $\sigma_s = 0.093\,\mathrm{fb}$ and of the background $\sigma_b = 0.022\,\mathrm{fb}$ after all cuts. The main reason is due the large background suppression achieved by the additional cut on muon isolation, which could only be studied and optimised with a full detector simulation. Unfortunately a direct comparison with the older study is only possible using event counting methods. Scaling the expected numbers of signal and background events from the old study to an integrated luminosity of $20\,\mathrm{fb}^{-1}$, a significance of $S_{c12} = 2.5$ is obtained, compared to a value of 3.2 from this study.

Table 7.8: *Efficiency of the muon reconstruction for high luminosity, after the preselection cuts of Table 6.2 and in the pseudo-rapidity range* $|\eta < 2.4|$.

channel	$4\ \mu$ reco efficiency at high luminosity
$\mathrm{H} \rightarrow \mathrm{ZZ}^* \rightarrow 4\,\mu$: $m_H = 115\,\mathrm{GeV}$	66 %
$\mathrm{H} \rightarrow \mathrm{ZZ}^* \rightarrow 4\,\mu$: $m_H = 120\,\mathrm{GeV}$	70 %
$\mathrm{H} \rightarrow \mathrm{ZZ}^* \rightarrow 4\,\mu$: $m_H = 125\,\mathrm{GeV}$	71 %
$\mathrm{H} \rightarrow \mathrm{ZZ}^* \rightarrow 4\,\mu$: $m_H = 130\,\mathrm{GeV}$	72 %
$\mathrm{H} \rightarrow \mathrm{ZZ}^* \rightarrow 4\,\mu$: $m_H = 140\,\mathrm{GeV}$	74 %
$\mathrm{ZZ}^* \rightarrow 4\,\mu$	63 %
$\mathrm{t\bar{t}} \rightarrow 4\,\mu$	61 %
$\mathrm{Zb\bar{b}} \rightarrow 4\,\mu$	48 %

7.7 Study of High Luminosity

At high luminosity the number of minimum bias events from collisions in the same bunch crossing quintuples compared to the low luminosity phase. For some other Higgs discovery channel, the reconstruction efficiency could decrease rapidly or new backgrounds could occur at high luminosity. The $\mathrm{H} \rightarrow \mathrm{ZZ}^* \rightarrow 4\,\mu$ channel is insensitive to these influences (compare to Sect. 7.9). This is due to the clear signature and due to the fact that most particles do not reach the crucial part of the detector for this analysis, the muon chambers. For studies of $\mathrm{H} \rightarrow \mathrm{ZZ}^* \rightarrow 4\,\mu$ with high luminosity the same signal and background samples as in the low luminosity study were used, but the number of overlaid minimum bias events was increased to an average of 17.85 per event.

As can be seen from the numbers in Tab. 7.8 the muon reconstruction efficiency in the high luminosity case is only slightly lower by typically 1 – 2 % compared to the low luminosity case. Beside that, the other distributions presented in Sect. 7.1 remain similar, leading to identical cuts in both cases. The cut on calorimeter isolation, however, has to be relaxed in order to avoid signal losses and is effectively disabled by setting the cut to a very high value of $E_T^{max} < 30\,\mathrm{GeV}$.

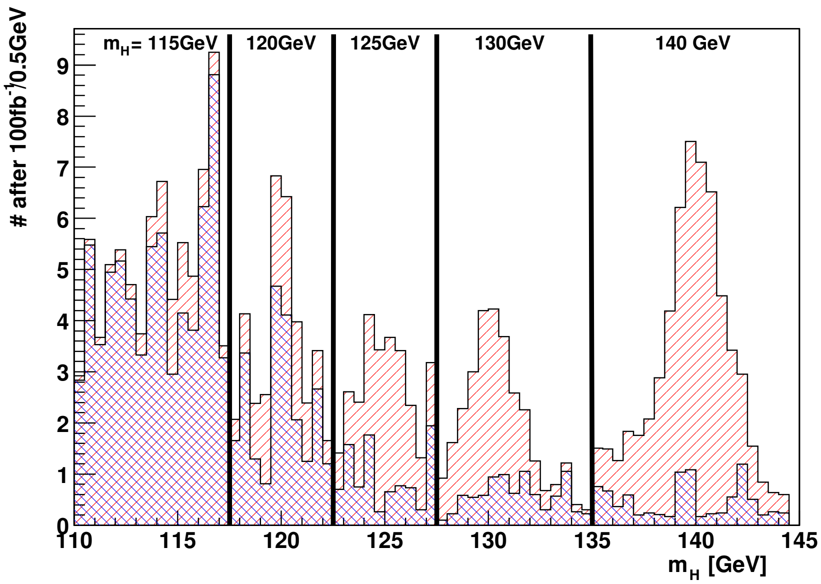

Figure 7.16: *Distributions of the four-muon invariant mass for signal plus background and for background only for Higgs boson masses of 115 GeV, 120 GeV, 125 GeV, 130 GeV and 140 GeV at high luminosity. For each value of Higgs boson mass the corresponding cuts described in Section 7.1, Tables 7.1 and 7.2 have been applied. Only the tracker isolation cuts of Table 7.3 have been made, the calorimeter cut is set to a very high value of* $E_T^{max} < 30$ *GeV.*

The distributions of the invariant mass of the four muons for signal and background for high luminosity are summarised in Fig. 7.16. Individual distributions for each Higgs boson mass for high and high luminosity are shown in the figures in the Appendix C. The signal and background cross sections and the resulting signal visibility after 100 fb^{-1} are summarised in Tab.s 7.9 and 7.10. The very low significance value of S_{l2} for a Higgs boson mass of 115 GeV is not larger than in the low luminosity case; this is due to a statistical fluctuation resulting from a small difference in the surviving signal and background events after all cuts (compare Fig.s C.1(a) and C.1(b) in Appendix C). For the high luminosity case the significance looses its importance, because at that time the Higgs should be clearly discovered in that mass range if it exhibits Standard Model like behaviour. At that time the properties of the Higgs will be studied. As pointed out in the previous Sect. 7.6 the number of signal events and the Higgs mass width are parameters to study. Their behaviour is summarised in Tab. 7.9.

Table 7.9: *Cross sections from binned likelihood fit to the weighted sum of signal and background events accepted after all cuts, σ_s and σ_b, respectively, for high luminosity. Values are given for the whole mass range considered (110-145 GeV), and for a mass window of $m_H \pm 2\Delta_{m_H}$; the fitted Higgs boson mass resolution, Δ_{m_H}, is given in the fourth column.*

Higgs boson mass	σ_s	σ_b	Δ_{m_H}	σ_s	σ_b
	full range			mass window $m_H \pm 2\sigma_{m_H}$	
140 GeV	0.511 fb	0.265 fb	1.4	0.421 fb	0.060 fb
130 GeV	0.273 fb	0.242 fb	1.4	0.236 fb	0.044 fb
125 GeV	0.244 fb	0.431 fb	1.4	0.210 fb	0.064 fb
120 GeV	0.175 fb	1.503 fb	1.4	0.154 fb	0.266 fb
115 GeV	0.058 fb	2.608 fb	1.4	0.051 fb	0.516 fb

Table 7.10: *Estimators of significance for an integrated luminosity of 100 fb^{-1} corresponding to one LHC year at high luminosity.*

Higgs boson mass	S_{l2}	$S_{poisson}$	S_{c12}	S_{c1}
140 GeV	9.3	10.7	9.0	17.2
130 GeV	6.7	7.5	6.4	11.2
125 GeV	5.5	6.2	5.4	8.3
120 GeV	2.6	2.8	2.6	3.0
115 GeV	0.6	0.7	0.7	0.7

7.8 Estimation of the Measurements of Higgs Couplings

The coupling behaviour of the Higgs boson in the Standard Model is fixed. The coupling of the Higgs boson is proportional to the mass of the fermions as described in Sect. 5.1. In non-standard models like the Supersymmetric Model the coupling of the Higgs boson can be different. So it is interesting to study these couplings. The ratio of the Higgs coupling can be obtained for example by comparing the Higgs decay $\mathrm{H} \rightarrow \mathrm{ZZ}^*$ with other channels like $\mathrm{H} \rightarrow \mathrm{W}^+\mathrm{W}^-$ or $\mathrm{H} \rightarrow \gamma\gamma$.

In order to get to know the Higgs coupling one has to know how many signal events N_s to expect:

$$N_s = \sigma_{tot} \cdot Br(H \rightarrow 4\mu) \cdot \epsilon_{pre} \cdot \epsilon_{trigger} \cdot \epsilon_{reco} \cdot \epsilon_{cuts} \cdot L_{int}. \tag{7.3}$$

The number of signal events depends on the total cross section for the Higgs production σ_{tot}, the branching ratio of the Higgs to decay into four muons Br(H $\rightarrow 4\mu$), the acceptance of the preselection cuts ϵ_{pre}, the trigger selection $\epsilon_{trigger}$, the reconstruction efficiency ϵ_{reco} and the selection cuts ϵ_{cuts}. In this thesis some of these numbers are given. The total cross section for the Higgs production is given in Tab. 5.1 for several Higgs masses. The error of the Higgs cross section can be estimated by comparing the next-to-leading order cross section with the next-to-next-to-leading order cross section. This uncertainty is about 10%. The integrated luminosity L_{int} is in typical hadron collider environments known to about 10%. The preselection efficiency is given in Tab. 6.1. The trigger efficiency is not studied in this thesis. It should be for the signal about 100%, because the muons of the signal have on average about seven times the possibility to trigger either the single muon or the di-muon trigger. The reconstruction efficiency with the current software is given in Tab. 6.6 for the low luminosity phase and 7.8 for the high luminosity phase. The number of signal events after the selection cuts is given in Tab.s 7.6 for the low luminosity case and 7.9 for the high luminosity case. The error ΔN_s found on the number of surviving signal events by fitting the events is summarised in Tab. 7.11. The error of the fitting procedure dominates the error of the number of signal events.

7.9 Study of the Influence of Multiple Collisions

Events with muons from different collisions, in other words two or three muons in one collision and one or two in another, may become a significant source of background due to the much higher rates compared to genuine $4\,\mu$ processes. The extra muon might also originate from a double-parton scattering process in the same collision.

To get the cross section of an event consisting of a three-muon process plus one extra muon, $\sigma_{3\mu+\mu}$, the three-muon cross section, $\sigma_{3\mu}$, is multiplied by the

Table 7.11: *Error on the number of signal events N_s obtained by the fitting procedure. For low luminosity an integrated luminosity of 20 fb^{-1} corresponding to the first LHC year is considered, for high luminosity 100 fb^{-1} corresponding to one LHC year at high luminosity. The values for a Higgs mass of 115 GeV have very high errors, so that they are not considered here.*

m_H GeV	$\frac{\Delta N_s}{N_s}$ for low lumi	$\frac{\Delta N_s}{N_s}$ for high lumi
140	34%	14%
130	46%	20%
125	55%	23%
120	89%	14%

probability for such an extra muon to occur in any of the collisions of the event,

$$\sigma_{3\mu+\mu} = \sigma_{3\mu} \cdot p_\mu \cdot n_{pu} \,. \tag{7.4}$$

Here, p_μ is the probability to find one reconstructed muon in a minimum-bias event, and n_{pu} is the number of underlying events, 3.41 for the low luminosity case and 17.85 for the high luminosity case.

Sources of $3\,\mu$ backgrounds result from processes which could also give a four-muon background like $\mathrm{t\bar{t}}$, $\mathrm{Zb\bar{b}}$ and ZZ. There can also be other processes like $\mathrm{Wb\bar{b}}$ and ZW. All of the backgrounds are characterised by the occurrence of a heavy gauge boson. This heavy particle is needed in order to mimic kinematic distributions similar to the signal. The cross sections for these three-muon backgrounds are summarised in Tab. 7.12.

The expected rate of single muons was studied with PYTHIA; in minimum bias events, the probability of occurrence of such muons is determined to be $6.12 \cdot 10^{-4}$, after preselection cuts of $p_T > 3\,GeV$, $|\eta| < 2.4$. Misidentified muons and the effect of non-prompt muons must be studied with the full detector simulation. For this purpose, the large minimum-bias sample of 200 000 fully simulated events from the spring production in 2002 [Lef03] was analysed. The probability for the occurrence of reconstructed muons satisfying the preselection criteria

$p_T > 3\,GeV$ and $|\eta| < 2.1$ [2] was thus determined to be $(3.6 \pm 0.4) \cdot 10^{-4}$. Overall, the probability of an extra single, reconstructed muon within the preselection cuts was determined to be approximately $1 \cdot 10^{-3}$ per collision.

Table 7.12: *Cross sections for the main three muon backgrounds. The total cross section σ_{tot} is the cross section for the production of the background with no limitation on the decay of the background processes. The branching ratio Br(bg$\rightarrow$3μ) is the branching ratio after two preselection cuts, $|\eta| < 2.5$ and $p_T > 3\,GeV$. The cross section $\sigma_{3\mu+\mu}$ is calculated according to Equation 7.4. The total cross section for the channels ZZ and ZW is taken in NLO from Ref. [lhca].*

background process	σ_{tot}	$\sigma_{tot}\cdot$ Br(bg$\rightarrow 3\,\mu$)	$\sigma_{3\mu+\mu}$
Zb$\bar{\text{b}}$	1492 pb	15.4 pb	15 fb $\cdot n_{pu}$
ZZ	18.2 pb	4.18 pb	4.1 fb $\cdot n_{pu}$
t$\bar{\text{t}}$	886 pb	2.09 pb	2.1 fb $\cdot n_{pu}$
Wb$\bar{\text{b}}$	172 pb	0.60 pb	0.60 fb $\cdot n_{pu}$
ZW	51.5 pb	0.07 pb	0.07 fb $\cdot n_{pu}$
total			22 fb $\cdot n_{pu}$

In order to estimate the contribution of single muons in combination with three-muon processes to the background after all cuts, the muons found in a sample of fully simulated three-muon events must be combined with reconstructed, single muons from the minimum-bias sample. A detailed study of the dominant three-muon background, Zb$\bar{\text{b}}$, is described below. Dedicated data samples of the Zb$\bar{\text{b}}$ $\rightarrow 3\mu$ background and of minimum bias events with a muon in each event were produced and processed through the full simulation. The kinematic properties of these muons were taken to be representative also for misidentified muons, for which no database with sufficiently high statistics was available. Here again, muons were reconstructed up to a value of $|\eta| < 2.4$.

The fraction of events with all three muons reconstructed was found to be 53% of the Zb$\bar{\text{b}}$ background events. The fraction of reconstructed single muons from minimum-bias is 42%, which is rather low due to the typically very low values of

[2] Unfortunately this small range in $|\eta|$ was chosen in this older study, the number of extra single muons in the larger range $|\eta| < 2.4$ should be about 15 % higher.

Table 7.13: *Rejection factors from muons reconstruction and of the cuts for* $\mu + (\mathrm{Zb\bar{b}} \rightarrow 3\mu)$. *The rejection factors give the fraction of events surviving each step with respect to the previous one.*

	rejection factor
μ reconstruction, $\mathrm{Zb\bar{b}}$	0.53
μ reconstruction, minimum-bias	0.65
isolation cut minimum bias	0.64
isolation cut $\mathrm{Zb\bar{b}}$	0.36
p_T cuts	0.03
Z, Z* and H mass cuts	0.04
reduction factor	$1 \cdot 10^{-4}$
vertex cut	0.003
total reduction factor	$0.003 \cdot 10^{-4} = 3 \cdot 10^{-7}$

p_T of such muons.

All cuts of Sect. 7.1, for a Higgs mass of 130 GeV, are applied to the combined events. The invariant mass of four muons is required to lie in the range 110 – 145 GeV. Technically, the pairing of muons and the cuts on the invariant masses were performed by combining the reconstructed four-vectors from both samples. To increase the statistical power, every event with three muons from $\mathrm{Zb\bar{b}}$ is combined with every muon from the minimum bias. The rejection factors of the cuts, listed in the same order as applied, are summarised in Tab. 7.13.

It is important to notice that the large background reduction due to the vertex cut is only effective if the fourth muon comes from a collision different from the one containing the 3μ event. An additional muon in the same collision could arise either from a misidentified muon in the beam remnant, or from double parton scattering. The rejection factors on the single muon of the other cuts should remain quite similar.

The cross section of double parton scattering is estimated in Ref. [Fab02], to be

$$\sigma_{doubleparton} = \frac{\sigma_{3\mu} * \sigma_{1\mu}}{\sigma_{eff}}. \tag{7.5}$$

Here $\sigma_{1\mu}$ is the one-muon cross section of the minimum bias, and σ_{eff} is estimated to range between (10-30) mb, which is not far from the minimum-bias cross section. The total four-muon cross section of 22 nb, after preselection cuts, as given in Tab. 7.12, therefore also approximates reasonably well the case of double parton scattering. Assuming properties of the event topology of the three-muon process and of the extra muon being similar to the multiple-collision case studied above, double parton scattering provides the dominant source of $3\mu + \mu$ backgrounds, which is, however, still very small compared to the main 4μ backgrounds studied earlier.

In summary, the cross section after all cuts for three-muon backgrounds plus an extra muon $\sigma_{3\mu+\mu}$, is estimated to be only about 0.002 fb. This background level is totally negligible compared to the other background sources.

Chapter 8

Conclusion

This thesis is divided into two parts: a technical part developing an algorithm to calculate the shift of the cluster position due to the Lorentz angle and a physics part studying the Higgs decay channel $H \rightarrow ZZ^* \rightarrow 4\,\mu$ in the mass range from 115 GeV to 140 GeV.

A comprehensive study of Lorentz shifts of non-irradiated and irradiated sensors is performed at Karlsruhe. The measured data are compared with the proposed algorithm taking into account the Lorentz angle. The dependence of the mobility on the electric field is taken into account, the influence of radiation damage on the Lorentz angle correction is studied. The algorithm is adjusted and simplified for the needs of the CMS pixel and tracker detector. The algorithm for the silicon strip detector is implemented in the full simulation and reconstruction framework ORCA.

The channel $H \rightarrow ZZ^* \rightarrow 4\,\mu$ is studied with the full reconstruction and simulation framework of CMS called ORCA. Signal and background events of the backgrounds $Zb\bar{b}$, $t\bar{t}$ and ZZ^* decaying in four muons were processed through the whole simulation and reconstruction chain for both the low and the high luminosity phases at LHC. Several advantages of these realistic studies can be found: the reconstruction efficiency is studied and it was found that it is different for signal and backgrounds; realistic optimised isolation cuts are found to suppress the $Zb\bar{b}$ and $t\bar{t}$ backgrounds. For light Higgs masses all cuts are optimised for each simulated Higgs mass. About 40% of all Higgs events within the acceptance of the CMS detector are finally selected by this analysis. In order to evaluate the actual separation of background and signal several definitions of significances are compared and a likelihood significance is chosen for this thesis. At a Higgs mass of 140 GeV, a discovery in the first year of LHC with a significance approaching a value of five seems possible. At lower masses this channel has to be combined with others for a discovery in the first year of LHC operation as shown in Tab. 8.1. This Higgs decay channel - also called gold-plated channel - is one of the few channels, which can still be detected at high luminosity. The low number of the signal and background events prohibits using the simple measure of significance given by the number of signal events divided by the square root of the number of background events, which is correct for Gaussian statistics. The present analysis using a realistic simulation shows a somewhat higher significance than an older Higgs study [Dro97].

Table 8.1: Significance of the likelihood method S_{l2} for several Higgs masses at low and high luminosity. One year of LHC is equivalent to $20\,\mathrm{fb}^{-1}$ at low luminosity and $100\,\mathrm{fb}^{-1}$ at high luminosity. For comparison the significance of the event counting method S_{ec1}, which is the ratio of the number of signal events and the square root of the number of background events, is given.

	low luminosity				high luminosity			
	after $20\,\mathrm{fb}^{-1}$		after $60\,\mathrm{fb}^{-1}$		after $100\,\mathrm{fb}^{-1}$		after $300\,\mathrm{fb}^{-1}$	
Higgs mass	S_{l2}	S_{ec1}	S_{l2}	S_{ec1}	S_{l2}	S_{ec1}	S_{l2}	S_{ec1}
140 GeV	4.2	7.6	7.3	13.2	9.3	17.2	16.1	29.8
130 GeV	3.2	5.7	5.5	9.8	6.7	11.2	11.6	19.5
125 GeV	2.3	3.6	4.0	6.2	5.5	8.3	9.5	14.4
120 GeV	1.1	1.2	1.9	2.1	2.6	3.0	4.5	5.2
115 GeV	0.5	0.5	0.9	0.9	0.6	0.7	1.0	1.2

Appendix A

Implementation of the Lorentz Angle in the CMS Software

In this Section, the implementation of the Lorentz angle algorithm for the strip detectors into the CMS full reconstruction software called ORCA is described [1].

The implementation of the Lorentz angle is done in such a way that a user of the software does not need to call the classes at all, but that they are invoked when starting any reconstruction, in other words calling the output of the detectors. This part of reconstruction is normally hidden by the reconstruction classes, but can be accessed if users want to use data for special purposes.

The detector system is described by the software. Any detector is represented by the *Det* interface from which the *DetUnit* corresponding to a physical detector inherits. Again the specialised detector classes like *SiStripDet* representing a silicon strip detector inherit from *DetUnit* (compare to Fig. A.1(a)). Inheritance means that the derived class provides all functionality of the base class. For computing purposes only limited characteristics of the detectors are implemented. For Example, the detection of traversing particles in the silicon detectors corresponds in the software to a detection surface the *Bound Plane*. In other words, the detectors are simplified to be flat. Besides the *BoundPlane* the *DetUnit* knows its *driftDirection*. So the only method which needs to be implemented here is *driftDirection*, which returns the drift direction of the ionization charges collected on the strips inside the detector volume (Fig. A.1(b)). In this method,

[1] This work is done in cooperation with Tommaso Bocalli.

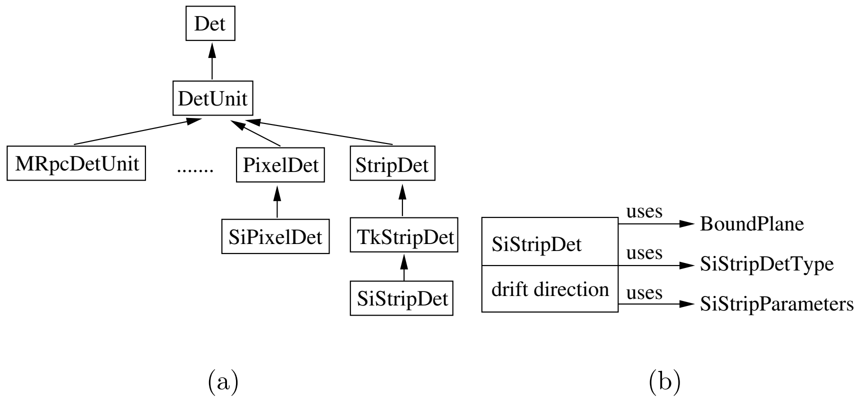

Figure A.1: *class SiStripDet: (a) Inheritance diagram of the class SiStripDet (b) Class diagram of the SiStripDet*

the Lorentz angle algorithm is implemented. The constants of the algorithm are stored in the class *SiStripParameters*. The actual thickness and doping concentration is stored in the class *SiStripDetType*. Both classes are used by the class *SiStripDet*. At the moment, the magnetic field is assumed to be 4 T without deviations in order to speed up the algorithm. During data taking some of this data, like temperature, full depletion voltage and applied voltage need to be changed to real detector data.

The current default parameters for the algorithm are the ones of Eqs. 4.4, 4.5 and 4.2. They are accessible as *.orcarc* parameters summarised in Tab. A.1.

Table A.1: *Parameters for the Lorentz angle description in the .orcarc file corresponding to the parameters in Eqs. 4.4, 4.5 and 4.2.*

Name	Default	Class	Corresponding to
HoleMobilityAtLowField	470.5	SiStripDet	μ_{low}
HoleSaturationVelocity	$8.36{\cdot}10^6$	SiStripDet	v_{sat}
HoleBeta	1.213	SiStripDet	β
HoleRHAllParameter	0.7	SiStripDet	r_{H}
HoleTemperature	297	SiStripDet	T
AppliedVoltage	150	SiStripDet	U_{bias}

Appendix B

Programmes of the CMS software

B.1 Overview

The CMS software consists of many standalone programmes, some of which have been used in this thesis. An overview of the major programmes is shown in Fig. B.1. One can divide the programmes into FORTRAN based programmes (left hand of Fig. B.1) and C++ based programmes (right hand of Fig. B.1). The programmes used in this thesis are FORTRAN based Monte Carlo generators, CMSIM, ORCA and Objectivity/DB as an object-oriented database (OODB). All of these programmes are described in the next sections of the Appendix. In this thesis a mixture of FORTRAN based programmes and object-oriented programmes is used since not all of the object-oriented programmes are already in a stage to work with them, for example OSCAR and FAMOS are not tested well enough.

At CMS there are in principle two ways to simulate events: the full simulation and the fast simulation. The full simulation, which is used in this thesis, simulates the detector response; the fast simulation takes the detector response into account by smearing the momenta of the particle. So the full simulation should give results which are closer to the measurements. The fast simulation packages are the FORTRAN based CMSjet programme and the object-oriented FAMOS programme. The full simulation and reconstruction programme is called ORCA. For the database production of fully simulated samples CMSIM is used.

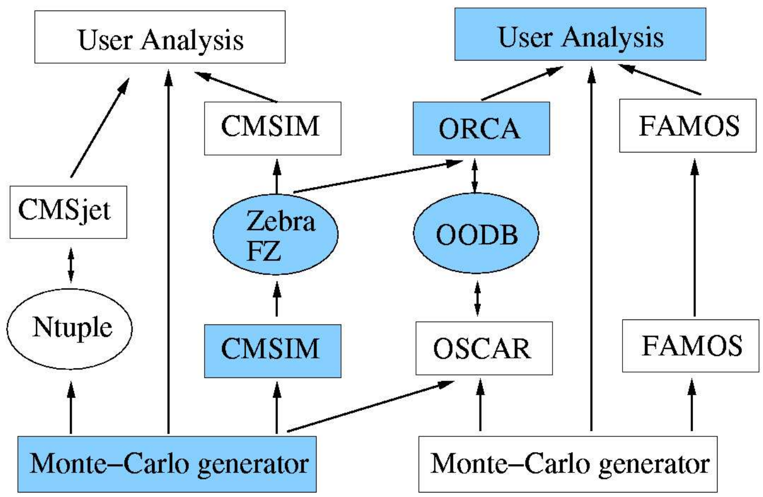

Figure B.1: *An overview over the CMS software, on the left hand side, FORTRAN based programmes, on the right hand side C++ based programmes. Data formats are specified by ellipses and programmes are specified by rectangles. The programmes and data formats used are underlaid with blue color (dark shaded).*

B.2 Main Programs

The main programs used in the physics analysis are:

- CMSIM (see [CMS]) (CMS Simulation package) is a full detector simulation using FORTRAN and GEANT3. Version cms125 is used. A detailed description can be found in Appendix B.3.

- Objectivity/DB [obj] is an object-oriented database storing the Monte Carlo information, the hits and the detector response called digitisation. This is the process of creating digis. Objectivity version 6.1.3 is used. A further description can be found in Appendix B.4.

- COBRA [COB] (Coherent Object-oriented Base for simulation Reconstruction and Analysis) provides basic services and utilities for analysing the data.

- ORCA [ORC] (Object-oriented Reconstruction for CMS Analysis) covers reconstruction as well as simulation tasks. A detailed description can be found at Appendix B.5. Version ORCA_6_3_0 is used for this thesis.

- IGUANA [IGU] (Interactive Graphics For User Analysis) is a graphical tool for displaying events.

- SCRAM [SCR] (Software Configuration, Release and Management) is a version management tool.

B.3 Detector Simulation Package CMSIM

The CMS simulation package CMSIM is an application of the GEANT3 (see [GEA]) detector description and simulation tool. CMSIM is used to describe the detector geometry and materials. It also includes and uses information about the magnetic field.

CMSIM reads the individual events from CMKIN ntuple and simulates the effects of energy loss, multiple scattering and showering in the detector materials with GEANT3. The information is stored in the form of hits (see Fig. 6.7). A simulated hit combines information about energy depositions in the detector, their magnitude, the time at which they occur and their location. In addition to the hits, CMSIM also produces simulated tracks and vertices. These are the original Monte Carlo information about the interactions and decays of particles in the detector.

B.4 Database Objectivity/DB

Objectivity is up to now the object-oriented database used for the storage of simulated data. This chapter describes the basic elements in an Objectivity/DB system and provides an overview of the Objectivity/DB tools. Details on the administration can be found in any Objectivity/DB manual (e.g. [Obj00]). An Objectivity/DB system consists of multiple processes and files that can be distributed across multiple host machines on a network (see Fig. B.2).

Federated Databases:
The federated database is the highest level in the Objectivity/DB logical storage hierarchy. Physically, each federated database exists as a file, with the ending **.FDDB*. This file contains the system database, which stores the schema for the federated database. A schema is a physical representation of the Objectivity/DB data model. It is a collection of type definitions and association

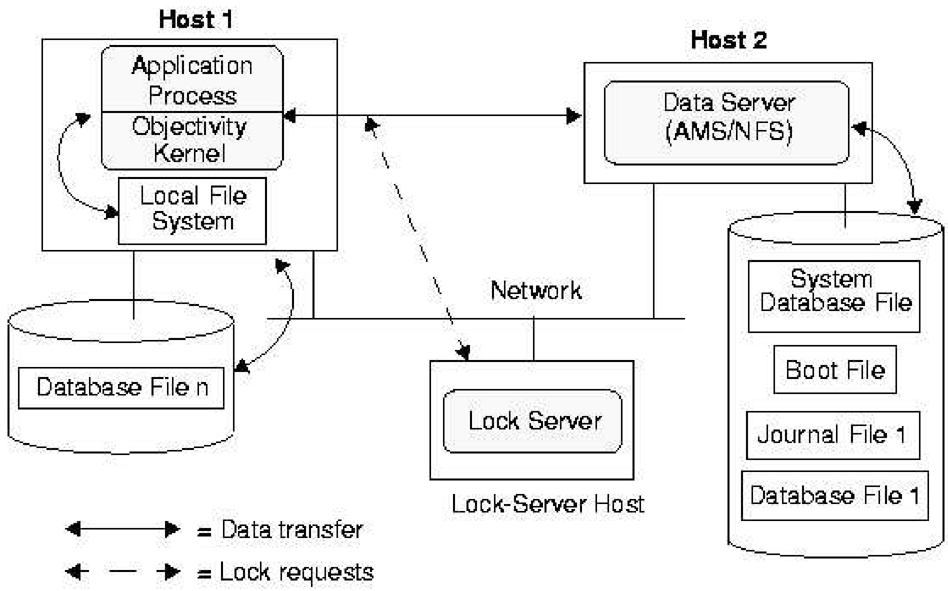

Figure B.2: *Structure of an Objectivity/DB system distributed across multiple host machines. [Obj00]*

definitions that allows a database to store and manage objects. When the data model changes, the schema has to be upgraded with a new schema file and the command *ooschemaupgrade*. The federated database file stores as well a catalogue of the additional databases that make up the federation. The catalogue of the federation can be printed out with the help of the command *oodumpcatalog*.

Every federated database has a boot file. Database applications, like any read- or write-jobs of ORCA, and tools, like any Objectivity command, refer to a federated dabase using its boot filename. The boot filename can be specified as a OO_FD_BOOT environment variable.

Database Files:

A database is where the persistent data is stored. A database is physically represented by a database file. As shown in Fig. B.2 some or all database files can be located at a different computer than the rest of the database. The distribution of a federated database over more than one computer is useful for improved scalability. But the complexity of the administration increases. For example after copying a federated database, the database has to be installed at the new site. This is done with the command *ooinstallfd*. The *ooinstallfd* tool requires that all files of the federated database are located in the same directory. If this is not the case, one has to run the *ooinstallfd* command with the *nocheck* option. This prints a warning for each database not located in the same directory. The catalogue of the federated database needs to be updated using *oochangedb* with the *-catalogonly* option. Each database is attached to one or more federated databases and is listed in the federated database's catalogue. The Objectivity/DB databases readable with ORCA jobs are organized like this:

- Meta databases contain the information where to find databases connected to each other. E.g. where to find the generator information of the digitized events.
- MCInfo databases contain the generator data.
- SimHits databases contain the simulated hits.
- TDigis and THits databases contain the digitized information.

To access the right database, *InputCollections* in the *.orcarc* file have to be specified. A list of OO_FD_BOOT variables and *InputCollections* of federated databases located at Karlsruhe can be found at the homepage of the institute.

Journal Files:
Whenever a transaction starts, it records update information in one or more journal files, which are used to return the federated database to its previously committed state if the transaction is aborted or terminated abnormally. Journal files are written in a federated database's jounal directory. These files should not be deleted.

Lock Server Process:
Objectivity/DB provides simultaneous multiuser access to data. To ensure that data remains consistent, database access is controlled through locks administered by a lock server. The lock server runs as a background process on one of the workstations in a network. Anyone can start the lockserver with the command *oolockserver*. It can be stopped by anyone with the command *ookillls* as long as no Objectivity/DB jobs are running. Sometimes, especially when the transactions are running via NFS the lock server is damaged, then the lock server has to be killed by killing the process *ools* and has to be restarted.

B.5 Reconstruction Framework ORCA and COBRA

In this chapter the two core elements of the CMS reconstruction software are described: ORCA and COBRA.

ORCA:
The CMS reconstruction software, ORCA (Object-oriented Reconstruction for CMS Analysis) is implemented in the C++ programming language. The ORCA project covers not only reconstruction tasks, but also includes code for simulating detector response and the Level-1 Trigger, as well as High-Level Trigger and analysis code.

ORCA has adopted a two-level decomposition - subsystems and packages - to match the different tasks it covers. For an overview of the currently available subsystems see Fig. B.3. Typical subsystems are Calorimetry, Tracker, Muon or Trigger matching the hardware components of CMS. Other subsystems provide common services for several subdetectors (CommonDet, CommonReco) or analysis tasks (Jets) or high-level reconstruction (TrackerReco, MuonReco, Vertex). Finally, subsystems for High-Level-Trigger selection and analysis are provided (ElectronPhoton, JetMetAnalysis, MuonAnalysis, bTauAnalysis). The subsystem Workspace is meant as a working environment for the user's private code.

COBRA:
The reconstruction software is based on the COBRA (Coherent Object-oriented Base for simulation Reconstruction and Analysis) software framework. Like ORCA COBRA can be decomposed into subsystems and packages. The subsystems comprise the GeneratorInterface, the MagneticField and CARF.
The GeneratorInterface interfaces the Monte-Carlo information. The MagneticField subsystem calculates the value of the magnetic field in a given point inside the CMS detector. CARF is the framework for CMS Analysis and Reconstruction. CARF comprises a set of classes with CMS specific components like detector components and event features and some service and utilities toolkit. It provides services like physics type services (histogrammers, fitters, mathematical algorithms, geometry and physics calculation routines) and

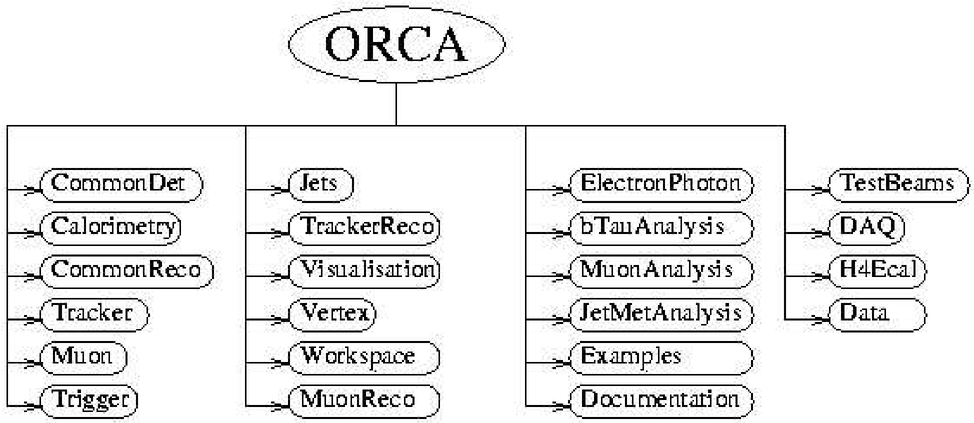

Figure B.3: *Subsystems of ORCA*

computer services (data access, inter-module communication, user interface, etc.).

Two main concepts implemented in the COBRA framework to steer the event processing are *action on demand* and *implicit invocation*. These concepts imply that modules register themselves at creation time and are invoked when required. In this way only those modules that are needed are loaded and executed.

For each standard package either in ORCA or in COBRA at least the following four sub-directories are present:

- doc: The documentation related to the package.
- interface: The C++ header files that can be referenced from other packages in the same or in different subsystems.
- src: The actual source code and C++ header files local to the package.
- test: Source code of test programmes for quality control of the package. Often this is equivalent to example programmes, showing typical use-cases of the classes.

B.6 KaMuonAnalysis Class Reference

The class KaMuonAnalysis handles the user code of the analysis. This class works with the ORCA version ORCA_6_3_0. In this class the reconstruction of the muons is called and information about the generated and reconstructed muons is stored into root-files. In addition a simple matching of the generated and reconstructed muons depending on the θ and η angles is implemented and the muons are matched corresponding to the Z boson masses. The final analysis is done with the help of ROOT programmes. With this approach the Monte Carlo samples have to be read out only once and any change in the final analysis cuts can be done without rereading the Monte Carlo samples. In the following the public methods of the class are described. A detailed description of also the public and private attributes can be found in [Wen03].

Inheritance diagram for KaMuonAnalysis:

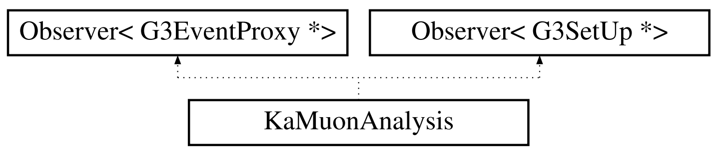

Public Methods

- **KaMuonAnalysis** () *Constructor.*
- ~**KaMuonAnalysis** () *Destructor: ROOT trees are saved.*
- void **initSetUp** () *Creates track reconstruction algorithms.*
- void **analysis** (G3EventProxy∗ ev) *Reads out reconstructed and generated muon data as Lorentz Vector.*
- void **getTrackerTracks** (G3EventProxy ∗ ev)
- void **FillRootTree** (int i,int block) *Root fill methods.*
- void **FillRootHisto** (int i,int block) *Root fill methods.*
- void **FindMinofMatrix** (int (∗col_match),float (∗col_quality),int (∗row_match),float (∗row_quality),int col_dimension,int row_dimension,int func) *Abstract method to find minimal element of a matrix. Here used for the matching of generated and reconstructed muons and the assignment of the muons to the real and virtual Z bosons.*

- void **getGeneratorParticles** (G3EventProxy ∗ ev) *Retrieves generator information about the muon.*

- float **delta_theta_phi** (int i_rec,int i_gen) *Computes the difference of the angles θ and ϕ between the generated and reconstructed muons and gives the value back to the method FindMinofMatrix.*

- float **delta_Z_Zreco** (int col,int row) *Computes the difference of the Z boson mass and the invariant mass of two reconstructed muons and gives the value back to the method FindMinofMatrix.*

- float **delta_Z_Zgen** (int col,int row) *Computes the difference of the Z boson mass and the invariant mass of two generated muons and gives the value back to the method FindMinofMatrix.*

- void **fillL1** () *Fills Level 1 Trigger information.*

- void **fillL2** (G3EventProxy ∗ ev) *Fills local muon reconstruction information.*

- void **fillL3** (G3EventProxy∗ ev) *Fills global muon reconstruction information.*

- bool **isIsolated** (const RecTrack∗ muon, char∗ algoname, int i) *Reads out the deposited transverse momentum in the tracker in a cone around the muon.*

- bool **isIsolated** (const MuIsoBaseContainer∗ isols, int i) *Reads out the deposited transverse energy in the calorimeter in a cone around the muon.*

Appendix C

Four Muon invariant Mass distributions

In the following the distributions of the four-muon invariant mass for signal plus background (red, light shaded) and for background only (blue, dark shaded) for all simulated Higgs masses (115 GeV, 120 GeV, 125 GeV, 130 GeV and 140 GeV) are shown. The cuts applied are depending on the Higgs mass and can be found in Tables 7.1, 7.2 and 7.3. For the high luminosity phase the calorimeter cut is changed and set to a value of $E_T^{max} < 30\,\mathrm{GeV}$. The figures show the distributions at $20\,\mathrm{fb}^{-1}$ for low luminosity in other words the expected luminosity at the first year of LHC and at $100\,\mathrm{fb}^{-1}$ for high luminosity, this is equivalent to the expected luminosity of LHC in the high luminosity phase. The histograms are the weighted sums of signal events and of the various background samples. The straight line represents a fit for background-only hypothesis, the curve is obtained with the signal-plus-background hypothesis. The remaining fluctuations seen in the background are due to the low statistics of available background events from Monte Carlo surviving all cuts. The plots are shown in the order of the simulated Higgs masses, followed by two tables with the bin entries for low luminosity and for high luminosity. With the help of the bin entries other likelihood methods for the estimation of signal visibility can be used instead of the one proposed and used in this thesis.

invariant mass distributions for a Higgs mass of 115 GeV:

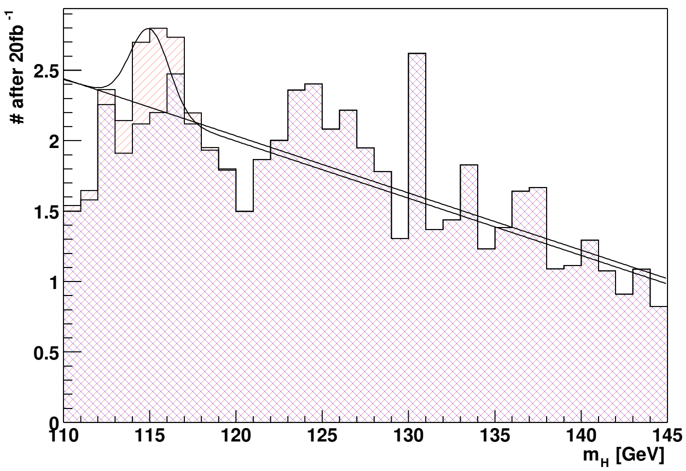

(a)

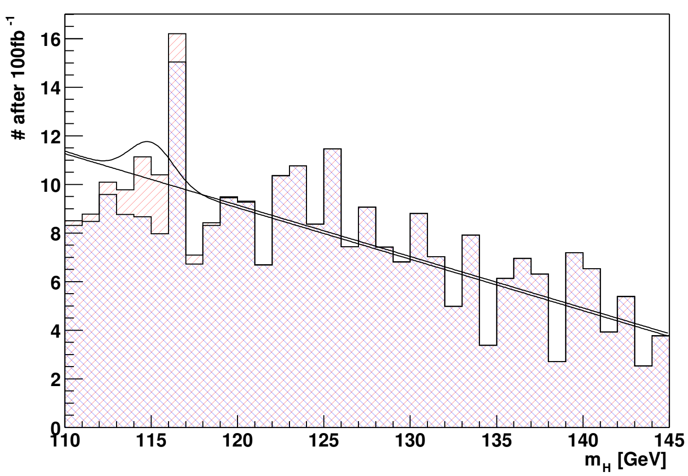

(b)

Figure C.1: *Histogram of the reconstructed invariant mass of four muons, for an integrated luminosity of 20 fb^{-1} at low luminosity operation (Fig. C.1(a)) and 100 fb^{-1} at high luminosity equivalent (Fig. C.1(b)) respectively. The histogram is the weighted sum of signal events with a Higgs mass of 115 GeV and of various background samples. The curves are fits obtained with background-only and a signal-plus-background assumption.*

Table C.1: *Distribution of the four muon invariant mass $m_{inv}^{4\mu}$ for low luminosity, a Higgs mass of 115 GeV after all cuts and after an integrated luminosity of 20 fb^{-1}: bin entries for signal plus background and for background only*

Higgs mass [GeV]	111	112	113	114	115	116	117
bin entry: sig. + bg	1.539	1.646	2.363	2.144	2.698	2.798	2.734
bin entry: background	1.501	1.581	2.257	1.910	2.120	2.201	2.474
Higgs mass [GeV]	118	119	120	121	122	123	124
bin entry: sig. + bg	2.197	1.952	1.800	1.498	1.867	2.003	2.359
bin entry: background	2.120	1.932	1.790	1.497	1.865	2.002	2.358
Higgs mass [GeV]	125	126	127	128	129	130	131
bin entry: sig. + bg	2.402	2.083	2.216	1.950	1.782	1.306	2.620
bin entry: background	2.402	2.082	2.216	1.950	1.782	1.306	2.620
Higgs mass [GeV]	132	133	134	135	136	137	138
bin entry: sig. + bg	1.369	1.438	1.828	1.233	1.383	1.642	1.667
bin entry: background	1.369	1.438	1.828	1.233	1.383	1.642	1.667
Higgs mass [GeV]	139	140	141	142	143	144	145
bin entry: sig. + bg	1.091	1.114	1.294	1.077	0.911	1.087	0.823
bin entry: background	1.091	1.114	1.294	1.077	0.911	1.087	0.823

Table C.2: *Distribution of the four muon invariant mass* $m_{inv}^{4\mu}$ *for high luminosity, a Higgs mass of 115 GeV after all cuts and after an integrated luminosity of* $100\,fb^{-1}$*: bin entries for signal plus background and for background only*

Higgs mass [GeV]	111	112	113	114	115	116	117
bin entry: sig. + bg	8.511	8.773	10.087	9.777	11.139	10.390	16.200
bin entry: background	8.312	8.483	9.588	8.771	8.665	7.966	15.044
Higgs mass [GeV]	118	119	120	121	122	123	124
bin entry: sig. + bg	7.093	8.427	9.494	9.306	6.701	10.365	10.7690
bin entry: background	6.721	8.319	9.444	9.277	6.681	10.356	10.759
Higgs mass [GeV]	125	126	127	128	129	130	131
bin entry: sig. + bg	8.363	11.470	7.438	9.069	7.427	6.815	8.809
bin entry: background	8.361	11.465	7.433	9.066	7.424	6.808	8.809
Higgs mass [GeV]	132	133	134	135	136	137	138
bin entry: sig. + bg	7.021	4.982	7.919	3.384	6.133	6.957	6.315
bin entry: background	7.021	4.979	7.917	3.384	6.133	6.954	6.313
Higgs mass [GeV]	139	140	141	142	143	144	145
bin entry: sig. + bg	2.714	7.189	6.531	3.928	5.390	2.525	3.773
bin entry: background	2.714	7.189	6.531	3.928	5.390	2.525	3.773

invariant mass distributions for a Higgs mass of 120 GeV:

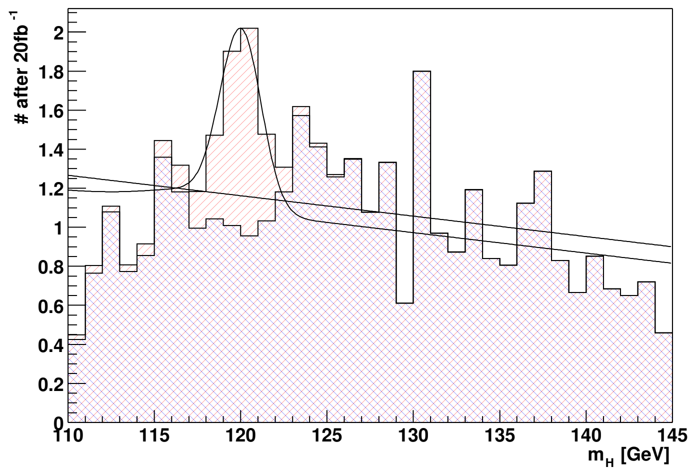

(a)

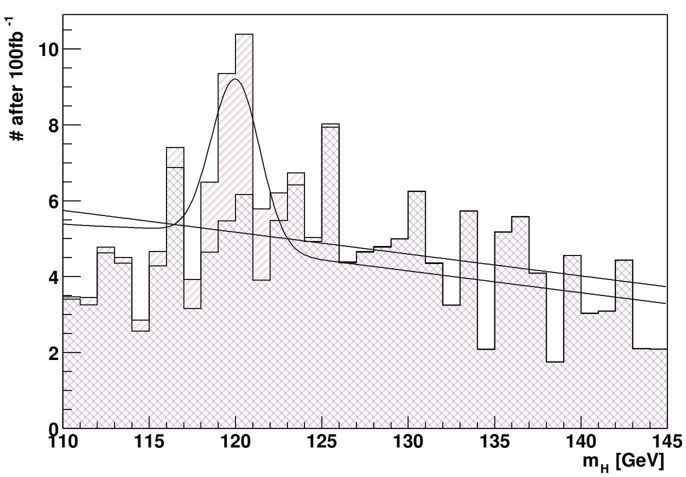

(b)

Figure C.2: *Histogram of the reconstructed invariant mass of four muons, for an integrated luminosity of 20 fb^{-1} at low luminosity (Fig. C.2(a)) and 100 fb^{-1} at high luminosity (Fig. C.2(b)) respectively. The histogram is the weighted sum of signal events with a Higgs mass of 120 GeV and of various background samples. The curves are fits obtained with background-only and a signal-plus-background assumption.*

Table C.3: *Distribution of the four muon invariant mass* $m_{inv}^{4\mu}$ *for low luminosity, a Higgs mass of 120 GeV after all cuts and after an integrated luminosity of 20 fb*$^{-1}$*: bin entries for signal plus background and for background only*

Higgs mass [GeV]	111	112	113	114	115	116	117
bin entry: sig. + bg	0.448	0.804	1.108	0.808	0.914	1.444	1.318
bin entry: background	0.425	0.764	1.078	0.773	0.855	1.359	1.182
Higgs mass [GeV]	118	119	120	121	122	123	124
bin entry: sig. + bg	1.183	1.472	1.901	2.019	1.477	1.308	1.619
bin entry: background	0.995	1.044	1.009	0.956	1.033	1.181	1.573
Higgs mass [GeV]	125	126	127	128	129	130	131
bin entry: sig. + bg	1.430	1.270	1.353	1.078	1.333	0.612	1.800
bin entry: background	1.412	1.258	1.348	1.077	1.332	0.611	1.800
Higgs mass [GeV]	132	133	134	135	136	137	138
bin entry: sig. + bg	0.970	0.873	1.193	0.839	0.806	1.123	1.288
bin entry: background	0.970	0.873	1.193	0.839	0.806	1.123	1.288
Higgs mass [GeV]	139	140	141	142	143	144	145
bin entry: sig. + bg	0.830	0.666	0.851	0.684	0.651	0.719	0.459
bin entry: background	0.830	0.666	0.851	0.684	0.651	0.719	0.459

Table C.4: *Distribution of the four muon invariant mass* $m_{inv}^{4\mu}$ *for high luminosity, a Higgs mass of 120 GeV after all cuts and after an integrated luminosity of 100 fb*$^{-1}$*: bin entries for signal plus background and for background only*

Higgs mass [GeV]	111	112	113	114	115	116	117
bin entry: sig. + bg	3.469	3.450	4.776	4.499	2.856	4.666	7.398
bin entry: background	3.404	3.257	4.624	4.356	2.561	4.280	6.876
Higgs mass [GeV]	118	119	120	121	122	123	124
bin entry: sig. + bg	3.924	6.485	9.348	10.385	5.785	6.207	6.737
bin entry: background	3.158	4.644	5.470	6.166	3.903	5.481	6.422
Higgs mass [GeV]	125	126	127	128	129	130	131
bin entry: sig. + bg	5.035	8.021	4.387	4.660	4.796	4.997	6.255
bin entry: background	4.924	7.939	4.363	4.640	4.780	4.993	6.246
Higgs mass [GeV]	132	133	134	135	136	137	138
bin entry: sig. + bg	4.359	3.247	5.729	2.090	5.178	5.580	4.094
bin entry: background	4.343	3.247	5.725	2.077	5.170	5.576	4.094
Higgs mass [GeV]	139	140	141	142	143	144	145
bin entry: sig. + bg	1.751	4.556	3.033	3.091	4.435	2.104	2.092
bin entry: background	1.751	4.556	3.033	3.091	4.435	2.104	2.092

invariant mass distributions for a Higgs mass of 125 GeV:

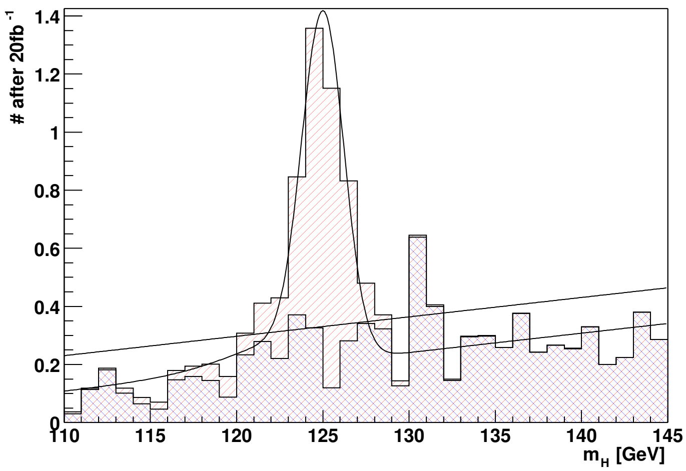

(a)

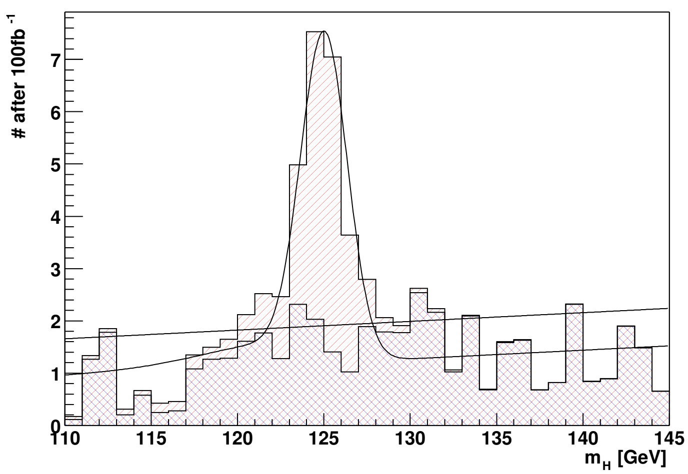

(b)

Figure C.3: *Histogram of the reconstructed invariant mass of four muons, for an integrated luminosity of 20 fb^{-1} at low luminosity (Fig. C.3(a)) and 100 fb^{-1} at high luminosity (Fig. C.3(b)) respectively. The histogram is the weighted sum of signal events with a Higgs mass of 125 GeV and of various background samples. The curves are fits obtained with background-only and a signal-plus-background assumption.*

Table C.5: *Distribution of the four muon invariant mass* $m_{inv}^{4\mu}$ *for low luminosity, a Higgs mass of 125 GeV after all cuts and after an integrated luminosity of* $20\,fb^{-1}$*: bin entries for signal plus background and for background only*

Higgs mass [GeV]	111	112	113	114	115	116	117
bin entry: sig. + bg	0.037	0.118	0.188	0.118	0.086	0.070	0.179
bin entry: background	0.030	0.114	0.182	0.101	0.064	0.046	0.147
Higgs mass [GeV]	118	119	120	121	122	123	124
bin entry: sig. + bg	0.194	0.201	0.159	0.308	0.411	0.429	0.846
bin entry: background	0.159	0.145	0.087	0.233	0.279	0.221	0.371
Higgs mass [GeV]	125	126	127	128	129	130	131
bin entry: sig. + bg	1.358	1.151	0.832	0.480	0.371	0.144	0.645
bin entry: background	0.326	0.120	0.281	0.341	0.323	0.127	0.639
Higgs mass [GeV]	132	133	134	135	136	137	138
bin entry: sig. + bg	0.405	0.149	0.297	0.299	0.258	0.377	0.243
bin entry: background	0.400	0.145	0.295	0.297	0.258	0.376	0.243
Higgs mass [GeV]	139	140	141	142	143	144	145
bin entry: sig. + bg	0.266	0.256	0.330	0.200	0.224	0.380	0.286
bin entry: background	0.266	0.256	0.330	0.200	0.224	0.380	0.286

Table C.6: *Distribution of the four muon invariant mass* $m_{inv}^{4\mu}$ *for high luminosity, a Higgs mass of 125 GeV after all cuts and after an integrated luminosity of 100 fb*$^{-1}$*: bin entries for signal plus background and for background only.*

Higgs mass [GeV]	111	112	113	114	115	116	117
bin entry: sig. + bg	0.172	1.333	1.852	0.309	0.665	0.428	0.454
bin entry: background	0.111	1.265	1.784	0.200	0.577	0.244	0.278
Higgs mass [GeV]	118	119	120	121	122	123	124
bin entry: sig. + bg	1.346	1.494	1.645	2.121	2.521	2.464	4.987
bin entry: background	1.081	1.263	1.285	1.611	1.766	1.281	2.315
Higgs mass [GeV]	125	126	127	128	129	130	131
bin entry: sig. + bg	7.529	7.0467	3.643	2.793	2.061	1.907	2.620
bin entry: background	2.028	1.403	1.025	1.889	1.789	1.778	2.539
Higgs mass [GeV]	132	133	134	135	136	137	138
bin entry: sig. + bg	2.234	1.059	2.108	0.691	1.605	1.643	0.677
bin entry: background	2.166	1.025	2.095	0.677	1.585	1.629	0.677
Higgs mass [GeV]	139	140	141	142	143	144	145
bin entry: sig. + bg	0.821	2.321	0.844	0.895	1.902	1.492	0.655
bin entry: background	0.821	2.315	0.837	0.888	1.895	1.485	0.655

invariant mass distributions for a Higgs mass of 130 GeV:

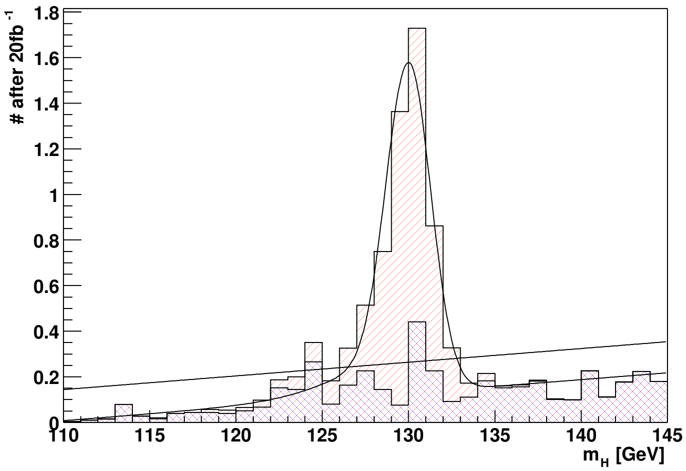

(a)

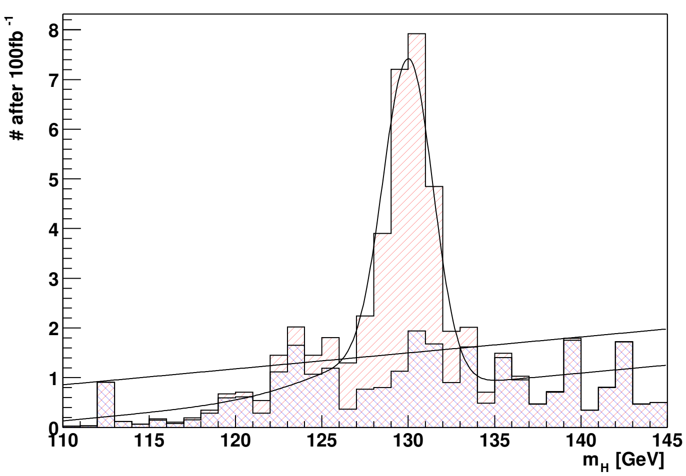

(b)

Figure C.4: *Histogram of the reconstructed invariant mass of four muons, for an integrated luminosity of 20 fb^{-1} at low luminosity (Fig. C.4(a)) and 100 fb^{-1} at high luminosity (Fig. C.4(b)) respectively. The histogram is the weighted sum of signal events with a Higgs mass of 130 GeV and of various background samples. The curves are fits obtained with background-only and a signal-plus-background assumption.*

Table C.7: *Distribution of the four muon invariant mass* $m_{inv}^{4\mu}$ *for low luminosity, a Higgs mass of 130 GeV after all cuts and after an integrated luminosity of* $20\,fb^{-1}$*: bin entries for signal plus background and for background only*

Higgs mass [GeV]	111	112	113	114	115	116	117
bin entry: sig. + bg	0.005	0.009	0.016	0.078	0.028	0.021	0.039
bin entry: background	0.005	0.009	0.014	0.078	0.028	0.016	0.039
Higgs mass [GeV]	118	119	120	121	122	123	124
bin entry: sig. + bg	0.044	0.057	0.055	0.066	0.098	0.187	0.200
bin entry: background	0.044	0.044	0.039	0.051	0.067	0.152	0.145
Higgs mass [GeV]	125	126	127	128	129	130	131
bin entry: sig. + bg	0.350	0.182	0.326	0.514	0.750	1.363	1.729
bin entry: background	0.266	0.081	0.164	0.226	0.145	0.076	0.442
Higgs mass [GeV]	132	133	134	135	136	137	138
bin entry: sig. + bg	0.862	0.327	0.172	0.215	0.161	0.165	0.185
bin entry: background	0.226	0.092	0.110	0.182	0.152	0.157	0.181
Higgs mass [GeV]	139	140	141	142	143	144	145
bin entry: sig. + bg	0.1034	0.099	0.226	0.113	0.178	0.224	0.180
bin entry: background	0.101	0.099	0.226	0.113	0.178	0.224	0.180

Table C.8: *Distribution of the four muon invariant mass* $m_{inv}^{4\mu}$ *for high luminosity, a Higgs mass of 130 GeV after all cuts and after an integrated luminosity of 100 fb*$^{-1}$*: bin entries for signal plus background and for background only*

Higgs mass [GeV]	111	112	113	114	115	116	117
bin entry: sig. + bg	0.022	0.033	0.908	0.122	0.067	0.172	0.106
bin entry: background	0.022	0.033	0.908	0.122	0.067	0.144	0.0778
Higgs mass [GeV]	118	119	120	121	122	123	124
bin entry: sig. + bg	0.192	0.344	0.676	0.708	0.540	1.45	2.018
bin entry: background	0.155	0.289	0.593	0.615	0.289	1.114	1.655
Higgs mass [GeV]	125	126	127	128	129	130	131
bin entry: sig. + bg	1.451	1.806	1.296	2.240	3.900	7.202	7.919
bin entry: background	1.070	1.192	0.366	0.770	0.803	1.130	1.939
Higgs mass [GeV]	132	133	134	135	136	137	138
bin entry: sig. + bg	4.849	1.936	2.013	0.712	1.491	1.033	0.476
bin entry: background	1.678	0.903	1.622	0.488	1.407	0.959	0.466
Higgs mass [GeV]	139	140	141	142	143	144	145
bin entry: sig. + bg	0.720	1.793	0.344	0.808	1.727	0.476	0.500
bin entry: background	0.710	1.755	0.344	0.799	1.718	0.466	0.500

invariant mass distributions for a Higgs mass of 140 GeV:

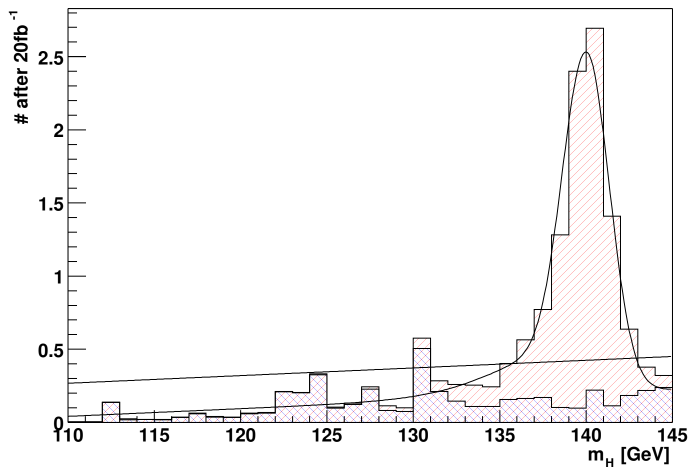

(a)

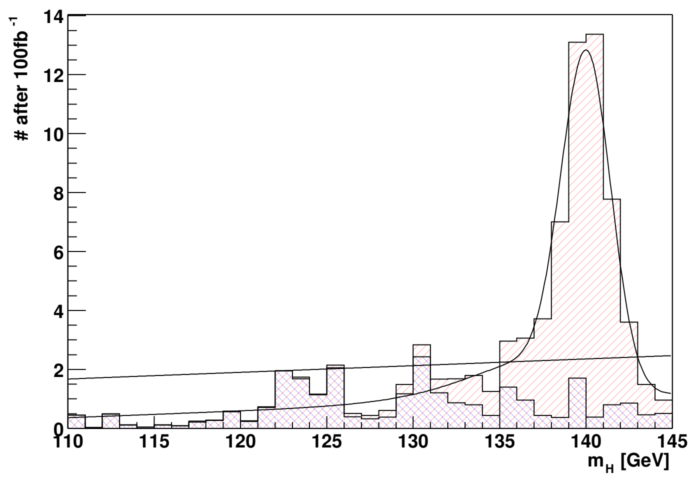

(b)

Figure C.5: *Histogram of the reconstructed invariant mass of four muons, for an integrated luminosity of 20 fb^{-1} at low luminosity (Fig. C.5(a)) and 100 fb^{-1} at high luminosity (Fig. C.5(b)) respectively. The histogram is the weighted sum of signal events with a Higgs mass of 140 GeV and of various background samples. The curves are fits obtained with background-only and a signal-plus-background assumption.*

Table C.9: *Distribution of the four muon invariant mass* $m_{inv}^{4\mu}$ *for low luminosity, a Higgs mass of 140 GeV after all cuts and after an integrated luminosity of* $20\,fb^{-1}$*: bin entries for signal plus background and for background only*

Higgs mass [GeV]	111	112	113	114	115	116	117
bin entry: sig. + bg	0.005	0.005	0.139	0.024	0.021	0.022	0.037
bin entry: background	0.005	0.005	0.136	0.018	0.021	0.018	0.034
Higgs mass [GeV]	118	119	120	121	122	123	124
bin entry: sig. + bg	0.062	0.039	0.037	0.062	0.067	0.212	0.205
bin entry: background	0.060	0.037	0.035	0.060	0.064	0.210	0.203
Higgs mass [GeV]	125	126	127	128	129	130	131
bin entry: sig. + bg	0.331	0.104	0.132	0.244	0.114	0.100	0.576
bin entry: background	0.326	0.097	0.122	0.228	0.080	0.074	0.506
Higgs mass [GeV]	132	133	134	135	136	137	138
bin entry: sig. + bg	0.285	0.260	0.254	0.243	0.404	0.564	0.771
bin entry: background	0.212	0.145	0.108	0.108	0.157	0.164	0.170
Higgs mass [GeV]	139	140	141	142	143	144	145
bin entry: sig. + bg	1.282	2.400	2.694	1.410	0.638	0.378	0.320
bin entry: background	0.101	0.097	0.221	0.113	0.183	0.219	0.240

Table C.10: *Distribution of the four muon invariant mass $m_{inv}^{4\mu}$ for high luminosity, a Higgs mass of 140 GeV after all cuts and after an integrated luminosity of 100 fb^{-1}: bin entries for signal plus background and for background only*

Higgs mass [GeV]	111	112	113	114	115	116	117
bin entry: sig. + bg	0.448	0.033	0.497	0.126	0.044	0.126	0.089
bin entry: background	0.448	0.033	0.482	0.111	0.044	0.111	0.089
Higgs mass [GeV]	118	119	120	121	122	123	124
bin entry: sig. + bg	0.241	0.281	0.589	0.263	0.730	1.955	1.738
bin entry: background	0.211	0.266	0.559	0.233	0.715	1.955	1.678
Higgs mass [GeV]	125	126	127	128	129	130	131
bin entry: sig. + bg	1.166	2.145	0.509	0.442	0.602	1.489	2.837
bin entry: background	1.136	2.055	0.389	0.322	0.377	1.174	2.432
Higgs mass [GeV]	132	133	134	135	136	137	138
bin entry: sig. + bg	1.672	1.680	1.793	1.258	2.960	3.059	3.718
bin entry: background	1.207	0.870	0.803	0.433	1.396	0.959	0.433
Higgs mass [GeV]	139	140	141	142	143	144	145
bin entry: sig. + bg	7.011	13.100	13.368	7.774	3.600	1.486	0.961
bin entry: background	0.366	1.700	0.377	0.799	0.855	0.466	0.511

Bibliography

[A$^+$01] I. Abt et al. Cluster shapes and cluster sizes in the HERA-B silicon vertex detector. *Nucl. Instr. and Meth. A*, 469:147 – 158, 2001.

[A$^+$02] N. Amapane et al. High level trigger algorithms for muon isolation. *CMS Note 2002/040*, 2002.

[ADD00] The CMS Collaboration, Addendum to the CMS Tracker TDR. CERN/LHCC 2000-16, 2000.

[Ale00] M. Aleppo. A measurement of Lorentz angle of radiation-hard pixel sensors. *Nucl. Instr. and Meth. A*, 465:108 – 111, 2000.

[Ale02] M. Aleppo. A measurement of Lorentz angle and spatial resolution of radiation-hard silicon pixel sensors. *Nucl. Instr. and Meth. A*, 481:204 – 221, 2002.

[B$^+$83] E. Belau et al. Charge collection in silicon strip detectors. *Nucl. Instr. and Meth. A*, 214:253, 1983.

[B$^+$98] L.J. Beattie et al. The electric field in irradiated silicon detectors. *Nucl. Instr. and Meth. A*, 418:314 – 321, 1998.

[B$^+$99] T.J. Brodbeck et al. Carrier Mobilities in Irradiated Silicon. *ROSE/TN/2000-09*, 1999.

[B$^+$01] V. Bartsch et al. An algorithm for calculating the Lorentz angle in silicon detectors. *CMS Internal Note 2001/027*, 2001.

[B$^+$02] G. Bruno et al. Local reconstruction in the muon detectors. *CMS Note 2002/043*, 2002.

[B$^+$03] V. Bartsch et al. An algorithm for calculating the Lorentz angle in silicon detectors. *Nucl. Instr. and Meth.*, A497:389–396, 2003.

[BK00] S.I. Bityukov and N.V. Krasnikov. On observability of signal over background. *Nucl. Instr. and Meth. A*, 452:518–524, 2000.

[Bla85] J. S. Blakemore. *Solid State Physics*. Cambridge Univ. Press, 1985.

[BQ02] V. Bartsch and G. Quast. Expected signal observability at future experiments. *CMS Internal Note 2003/039*, 2002.

[BW94] E. Barberio and Z. Was. *Comput. Phys.Commun.*, 79:291–308, 1994.

[C+75] C. Canalli et al. Electron and hole drift velocity measurements in Silicon and their empirical relation to electric field and temperature. *IEEE Transactions on Electron Devices, vol. ED-22*, pages 1045–47, 1975.

[C+95a] M. Carena et al. *Phys. Lett.*, B273:167, 1995.

[C+95b] J.A. Casas et al. Improved higgs mass stability bound in the standard model and implications for supersymmetry. *Phys. Lett.*, B342:171=179, 1995.

[C+99] G. Casse et al. Study of evolution of active volume in irradiated silicon detectors. *Nucl. Instr. and Meth. A*, 426:140 – 146, 1999.

[CE03] J. Campbell and K. Ellis. Mcfm - monte carlo for femtobarn processes. *http://mcfm.fnal.gov*, 2003.

[CMS] http://cmsdoc.cern.ch/cmsim/cmsim.html.

[COB] http://cobra.web.cern.ch/cobra.

[Com] http://theory.sinp.msu.ru/comphep.

[D+91] Yu. L. Dokshitzer et al. *Basic of Pertubative QCD*. Ed. Frontieres, Gif-sur-Yvette, 1991.

[D+03] D. Denegri et al. Summary of the CMS Discovery Potential for the Higgs boson. *CMS Note 2003/32*, 2003.

[Daw95] S. Dawson. Bounds on anomalous gauge boson couplings from partial Z width at LEP. *Nucl. Phys.*, B359:3–22, 1995.

[Daw97] *The Standard Model intermediate mass Higgs boson from S. Dawson in the Perspectiveson Higgs Physics II.* World Scientific, 1997.

[dB+01] W. de Boer et al. Lorentz angle measurements in irradiated silicon detectors between 77K and 300K. *Nucl. Instr. and Meth. A, 461*, pages 200 – 203, 2001.

[DET02] http://cmsdoc.cern.ch/cms/outreach/html/CMSmedia/CMSmovies/CMS_Slice.gif, 2002.

[Die03] Alexander Dierlamm. Studies on the Radiation Hardness of Silicon Sensors. Dissertation an der Universität Karlsruhe, 2003.

[DK94] S. Dawson and R.P. Kauffman. QCD corrections to Higgs boson production: non-leading terms in the heavy quark limit. *Phys. Rev.*, D49:2298–2309, 1994.

[DKS98] A. Djouadi, J. Kalinowski, and M. Spira. Hdecay: A program for higgs boson decays in the standard model and its supersymmetric extension. *Comp. Phys. Commun.*, 108C:56–74, 1998.

[Dro97] V. Drollinger. Die Suche nach dem Higgs-Boson - Studien für das CMS-Experiments. Diplomarbeit an der Universität Karlsruhe, 1997.

[DSZ91] A. Djouadi, M. Spira, and P.M. Zerwas. Production of Higgs bosons in proton colliders: QCD corrections. *Phys. Lett.*, B264:440–446, 1991.

[DW89] D.A. Dicus and S. Willenbrock. Higgs boson production from heavy quark fusion. *Phys. Rev.*, D39:751, 1989.

[E+95] V. Eremin et al. Carrier drift mobility study in neutron irradiated high purity silicon. *Nucl. Instr. and Meth. A*, 362:388 – 343, 1995.

[E+02] V. Eremin et al. Effect of radiation induced deep level traps on Si detector performance. *Nucl. Instr. and Meth. A*, 376:537 – 549, 2002.

[ECA97] The CMS Collaboration, The Electromagnetic Calorimeter Project, Technical Design Report. CERN/LHCC 97-33, 1997.

[F+00] E. Focardi et al. The CMS silicon tracker. *Nucl. Instr. and Meth. A*, 453:121, 2000.

[Fab02] A. Del Fabbro. Double parton scattering processes in pp collisions and the scale factors. *hep-ph/0111416*, 2002.

[fer] http://www.fermions.com.

[G+62] J. Goldstone et al. Broken symmetries. *Phys. Rev*, 127, 1962.

[G+70] S.L. Glashow et al. Weak interactions with lepton-hadron symmetry. *Phys. Rev*, D2:1285–1292, 1970.

[G+93] D. Graudenz et al. QCD corrections to Higgs boson production at proton proton colliders. *Phys. Rev. Lett.*, 70:1372–1375, 1993.

[GEA] *GEANT3, version 3.21/13 (release 15111999), Detector Description and Simulation Tool, CERN program library long writeup W5013.*

[GK02] E. Gross and A. Klier. *Supersymmetry and unification of fundamental interactions.* Hamburg, 2002.

[H+92] T. Han et al. Structure function approach to vector boson scattering in pp collisions. *Phys. Rev. Lett.*, 69:3274–3277, 1992.

[H+99] F. Hornung et al. High Magnetic Field facilities and Projects at the Forschungszentrum Karlsruhe . 1999.

[H+02] K. Hagiwara et al. *Review of Particle Physics, Particle Data Group.* 2002.

[Har00] R.V. Harlander. Virtual corrections to gg→H to two loops in the heavy top limit. *Phys. Lett.*, B492:74–80, 2000.

[Hau00] F. Hauler. Lorentzwinkelmessungen an bestrahlten Silizium-Streifendetektoren im Temperaturbereich T=77-300K. Diplomarbeit an der Universität Karlsruhe, 2000.

[hbo] http://wwwinfo.cern.ch/asdoc/hbook_html3/hboomain.html.

[HCA97] The CMS Collaboration, The Hadronic Calorimeter Project, Technical Design Report. CERN/LHCC 97-31, 1997.

[Hei99] S. Heising. Silicon detectors for high energy physics experiments at low temperatures and high magnetic fields. Dissertation an der Universität Karlsruhe, 1999.

[Hig66] P. W. Higgs. Spontaneous symmetry breakdown without massless bosons. *Phys. Rev.*, 145:1156 – 1163, 1966.

[HK02] R.V. Harlander and W. B. Kilgore. Next-to-next-to leading order Higgs production at hadron colliders. *Phys. Rev. Lett.*, 88:201801, 2002.

[HLT03] The CMS Collaboration, Technical Design Report, Volume 2, Data Acquisition and High-Level Trigger, Technical Design Report. to be published, 2003.

[HR97] T. Hambye and K. Riesselmann. Matching conditions and higgs mass upper bounds revisited. *Phys. Rev.*, D55:7255–7262, 1997.

[Huh01] M. Huhtinen. Simulation of non-ionising energy loss and defect formation in silicon . *RD48 Technical Note 2001-02*, 2001.

[IGU] http://iguana.web.cern.ch/iguana.

[Jon95] L.L. Jones. Premux128 specification version 2.3. Rutherford Internal Note, 1995.

[Kun84] Z. Kunszt. Associated production of heavy Higgs boson with top quarks. *Nucl. Phys.*, B247:339–359, 1984.

[L+99] C. Leroy et al. Charge transport in non-irradiated and irradiated silicon detectors. *Nucl. Instr. and Meth.*, A426:90 – 102, 1999.

[Laz87] M. S. Lazo et al. Silicon and silicon dioxide neutron damage functions. In *Proc. Fast Burt React. Workshop*, volume 1. Sandia National Laboratories, 1987. SAND, SAND87-0098.

[Lef02] V. Lefebure. http://cmsdoc.cern.ch/cms/production/www/cgi/SQL/List_Dataset_forBrowsing.php, OO_FD_BOOT = nobj03.cern.ch::/usr/objy/cmsprod/test/reconstruction/user/jet0102/jet0102.boot, InputCollection = /System/jm_Hit600_g125_CERN/jm02_MB/jm02_MB, 2002.

[Lef03] V. Lefebure. http://cmsdoc.cern.ch/cms/production/www/cgi/SQL/List_Dataset_forBrowsing.php, OO_FD_BOOT = nobj03.cern.ch::/usr/objy/cmsprod/test/orca6test/jet0102/jet0102.boot, InputCollection = 392:/System/sw_NoPU600pre9_TkMug125_CERN/jm02_MB/jm02_MB, 2003.

[Leo94] W. R. Leo. *Techniques for Nuclear and Particle Physics Experiments — A How-to Approach.* Springer, Berlin, New-York, 2nd revised edition, 1994.

[LEP03a] LEP Higgs Working Group for Higgs Boson searches. http://lepewwg.web.cern.ch/lepewwg/, 2003.

[LEP03b] LEP Higgs Working Group for Higgs Boson searches. Search for the Standard Model Higgs Boson at LEP. *CERN-EP-2003-11*, 2003.

[lhca] Proceedings of the workshop on Standard Model (and more) at the LHC. CERN 2000-04.

[LHCb] The LHC study group, The Large Hadron Collider Conceptual Design. CERN/AC/95-05.

[Lut99] Gerhard Lutz. *Semiconductor Radiation Detectors*, volume 1. Springer, Heidelberg, 1999.

[M^+99] D. Menichelli et al. Modelling of the observed double-junction effect. *Nucl. Instr. and Meth. A*, 426:135 – 139, 1999.

[Mig01] E. Migliore. http://cmsdoc.cern.ch/tracker/managment/agenda_gtm/agenda_0101.html, 2001.

[MP91] W.J. Marciano and F.E. Paige. Associated production of Higgs bosons with t- and anti-t pairs. *Phys. Rev. Lett.*, 66:2433–2435, 1991.

[MUO97] The CMS Collaboration, The Muon Project, Technical Design Report. CERN/LHCC 97-32, 1997.

[Neu] N. Neumeister. Single and Di-Muon Trigger Thresholds, Standard Model PRS meeting, CPT week May 2003. http://neumeist.home.cern.ch/neumeist/talks/talks.html.

[obj] http://www.objectivity.com.

[Obj00] Objectivity. *Objectivity/DB Administration*, 2000.

[ORC] http://cmsdoc.cern.ch/orca.

[Pul00] I. Puljak. Potentiel de decouverte du boson de Higgs dans le canal $H \rightarrow ZZ^* \rightarrow 4e^{\pm}$. Doctorat de l‘universite Paris, 2000.

[R$\ddot{9}$8] F. Röderer. Messung von Lorentz-Winkeln in Silizium-Detektoren. Diplomarbeit an der Universität Karlsruhe, 1998.

[roo] http://root.cern.ch/.

[Ros01] Rd48 collaboration. *Nucl. Instr. and Meth. A*, 46:308, 2001.

[S+93] M. Spira et al. SUSY Higgs production at proton colliders. *Phys. Lett.*, B318:347–353, 1993.

[S+01] T. Sjostrand et al. High Energy Physics Event Generation with PYTHIA 6.1. *Comput. Phys. Commun.*, 135:238–259, 2001.

[SC03] M. Sani and V. Ciulli. Search for the Standard Model Higgs boson in the four-muon final state with the CMS detector. *CMS Analysis Note 2003/005*, 2003.

[SCR] http://cmsdoc.cern.ch/releases/scram/current/scrampage.cgi.

[See73] K. Seeger. *Semiconductor physics*. Springer Verlag, Berlin, Heidelberg, New York, 1973.

[Smi68] R. A. Smith. *Semiconductors*. Cambridge Univ. Press, 1968.

[Spi95] M. Spira. HIGLU: A program for the calculation of the total Higgs production coross-section at hadron colliders via gluon fusion including QCD corrections. *DESY T-85-05*, B453, 1995.

[Spi98] M. Spira. QCD effects in Higgs physics. *Fortschr. Phys.*, 46:203–284, 1998.

[Sze85] S. M. Sze. *Semiconductor Devices, Physics and Technology*. John Wiley & sons, New York, 1985.

[TRA98] The CMS Collaboration, The Tracker Project, Technical Design Report. CERN/LHCC 98-6, 1998.

[TRI00] The CMS Collaboration, The Trigger and Data Acquisition project, Volume 1, The Level-1 Trigger, Technical Design Report. CERN/LHCC 2000-038, 2000.

[vEK90] B. van Eijk and R. Kleiss. *Proceedings of the Large Hadron Collider Workshop, Aachen*, 11(1):510, 1990.

[vL+80] V. A. J. van Lint et al. *Mechanisms of Radiation Effects in Electronic Materials*, volume 1. John Wiley & Sons, New York, 1980.

[Wei67] S. Weinberg. *Rev. Lett*, 19, 1967.

[Wen03] Joanna Weng. Analysis of the channel H$\rightarrow 4\mu$ in the object-oriented software environment of CMS. Diplomarbeit an der Universität Karlsruhe, 2003.

[Wun92] R. Wunstorf. Systematische Untersuchungen zur Strahlenresistenz von Silizium-Detektoren für die Verwendung in Hochenergiephysik-Experimenten. Dissertation an der Universität Hamburg, 1992.

Acknowledgements

During my Ph.D. thesis many people gave me inspiration in discussions, emails, etc.. I can not mention all of them by name but they can be sure that my thoughts are with them.

Some of them had such an impact on my thesis that I need to thank them more thoroughly. I thank my Doktorvater Prof. Dr. Wim de Boer for giving me the chance to do this Ph. D. thesis. I thank the Korreferent Prof. Dr. Günter Quast for partly supervising the thesis. I thank both of them for their physics insights. The diverse areas of research in the institute EKP were helpful for my development. Especially useful were the weekly seminars and the of course the cakes.

Some help came from nearly out of space - from CERN. Here the person I have to thank most is Sasha Nikitenko who kept an eye on my work. It was always a nice experience to go to CERN and realise that one is part of a big particle physics family.

Some people have read my Ph. D. thesis, these were Kerstin Höpfner, Stefanie Menzemer, Klaus Rabbertz, Christian Weiser and Valeri Zhukov,. Many thanks for your useful comments!

Part of the physics family was of course around at Karlsruhe and it was a pleasure to spend the lunch break with them or to share the office with them. In particular I would like to mention Christian Sander, Bettina Hartmann and Sabine Feyen. Besides physics a Ph. D. is something very personal and so I thank my husband and my mum for supporting me.